Improving Biocompatibility of Implantable Bioelectronics using Zwitterionic Cysteine

by

Peter YH Lin

A thesis
presented to the University of Waterloo
in fulfillment of the
thesis requirement for the degree of
Doctor of Philosophy
in
Chemical Engineering (Nanotechnology)

Waterloo, Ontario, Canada, 2017

Examining Committee Membership

The following served on the Examining Committee for this thesis. The decision of the Examining Committee is by majority vote.

External Examiner	ELIZABETH GILLIES Professor
Supervisor	FRANK GU Professor
Internal Member	NEIL MCMANUS Professor WILLIAM A. ANDERSON Professor
Internal-external Member	VIVEK MAHESHWARI Professor

Author's Declaration

I hereby declare that I am the sole author of this thesis. This is a true copy of the thesis, including any required final revisions, as accepted by my examiners.

I understand that my thesis may be made electronically available to the public.

Abstract

Recent advances in bioelectronics have allowed for faster diagnoses of diseases as well as treatments for disorders that were previously considered incurable. The performance of these devices is, however, severely hindered *in-vivo* due to the body's inherent immune response. Surface fouling, rapid oxidation, and fibrous encapsulation are some of the common issues that reduce device performance and lead to device failure. Overcoming these issues becomes especially critical when a bioelectronic is designed for prolonged exposure to the host in the form of an implant. Constant exposure to the host results in rapid deterioration of device functionality and a secondary surgery is often required to replace the dysfunctional device. The inclusion of various surface modifications, specifically zwitterionic coatings, have recently demonstrated promising results in prolonging a device's performance *in-vivo*.

An extensive literature review indicates that current antifouling coatings are mainly composed of long-chain hydrophilic or zwitterionic polymers; however, these thick polymer brushes are often undesirable for bioelectronics, especially devices designed for electrotherapy as the therapeutic electric pulse decays exponentially with respect to coating thickness. There is a growing need for an engineered surface that is biocompatible, resistant to nonspecific protein adsorption, and does not interfere with the device function in order to prolong the bioelectronics' *in-vivo* lifetime.

This research focuses on developing an ultra-thin and highly zwitterionic antifouling coating that is also biocompatible and versatile. Cysteine is selected as the coating material because it is a small biomolecule, highly zwitterionic at physiological pH, inherently biocompatible, and practical to fabricate. By optimizing the fabrication process, a monolayer cysteine coating of 8.64Å in thickness is achieved. X-ray photoelectron spectroscopy confirms the protonation of the amine group and the deprotonation of the carboxyl group, and that 87.84% of the surface cysteine is zwitterionic when fabricated at room temperature. This zwitterionic percentage is increased to 94.47% by increasing the reaction temperature

to 330K. The adsorption kinetics of zwitterionic cysteine onto a gold surface is studied through monitoring a liquid interface quartz-crystal microbalance in real time and the rate constants are calculated. Cysteine is also inherently biocompatible because it is an amino acid that exists in, and is produced by, our body. Fabrication of a cysteine monolayer is also practical; the sulfur headgroup on cysteine allows for a one-step synthesis onto a gold substrate without the need of a linker molecule. The fabrication can be completed in solution, which allows for the coating of curved or ridged surfaces that can be challenging for other coating processes such a vacuum deposition.

Investigation towards the antifouling performance of zwitterionic cysteine begins by quantifying the hydration layer around the molecule. Surface hydration is a key attribute that dictates a material's antifouling performance. The layer of water associated with the surface acts as an energy barrier that proteins must overcome in order to adsorb onto the surface. Molecular dynamic simulations indicate that a zwitterionic cysteine molecule associates 43.89 water molecules per nm^3, which is comparable to established zwitterionic coatings. The degree of surface fouling from various plasma proteins and human blood was quantified by a liquid interface quartz crystal microbalance in real time, and a zwitterionic cysteine surface can reduce fouling from BSA by 95%, fibrinogen by 93%, and human blood by 93% compared with an untreated gold surface.

This thesis demonstrates that an ultra-thin monolayer of highly zwitterionic cysteine capable of significantly reducing biological fouling can be fabricated through solution chemistry. This technology exemplifies the tremendous potential of engineering at a nanoscopic level and has application in the field of bioelectronics, tissue engineering, contact lenses, marine membranes, and drug delivery.

Acknowledgements

First and foremost, I would like to express my most sincere gratitude to my supervisor, Professor Frank Gu, who has been an excellent mentor throughout my Ph.D. Without his invaluable guidance, input, and recommendations, my research projects would not have been successful. The training I received in his laboratory has prepared me for independent research and future career as a researcher. I would also like to thank my external collaborator and mentor, Professor Chii-Wann Lin, from National Taiwan University for granting me the opportunity to research internationally in his lab in Taiwan.

I would like to express my deepest gratitude to my thesis committee members, Professor William Anderson, Professor Vivek Maheshwari, Professor Neil McManus, and Professor Elizabeth Gillies for their participation in my defense and for providing critical comments to my thesis.

I would like to acknowledge the support from various research groups that had been instrumental to the progress of this research project. I would like to thank Brandon Seo and Professor Ting Tsui for their help with SEM imaging. I would like to thank Jung-Soo Kang from WATLab for his help with XPS analysis. I would like to thank Dr. Bahareh Sadeghimakki from Professor Siva Sivoththaman's research group for her help with ellipsometry. I would like to thank Maris Chuang, Chia-Chen Chang, and Chi-Ying Liu from Professor Lin's research group for their help with QCM and SPRi analysis.

I would also like to thank all lab members within our research group for their support, input, and companionship. I would like to especially thank Sandy Liu, Jasper Huang, Terence Chan, Timothy Leshuk, Sarah LeBlanc, and Drew Davidson.

I am extremely grateful to my family for their support and I would like to especially thank my brother Matt for his encouragement and life tips.

Finally, I would like to express my gratitude for fanatical supports provided by various organizations: Ontario Graduate Scholarship (OGS), University of Waterloo (UW) Faculty of Engineering Graduate Scholarship, UW Graduate Research Studentship, UW President's Graduate Scholarship, and Waterloo Institute for Nanotechnology (WIN) Nanofellowship.

Dedications

This thesis is dedicated to my Great-grandmother, Grandmother, and Thunder

May they rest in peace.

Table of Contents

List of Figures

List of Tables

List of Abbreviations

Asp	Aspartic acid
BCA	Bicinchoninic acid assay
BSA	Bovine serum albumin
CB	Carboxybetaine
CBMA	Carboxybetaine methacrylate
COC	Cyclic olefin copolymer
ELISA	Enzyme-linked immunosorbent assay
FDA	United States Food and Drug Administration
FWHM	Full width at half maximum
Glu	Glutamic Acid
HS	Human serum
HAS	Human serum albumin
Lys	Lysozyme
MD	Molecular dynamics
MPC	Methacryloyloxylethyl phosphatidylcholine
OEG	Oligo(ethylene glycol)
PBS	Phosphate-buffered saline
PC	Phosphatidylcholine

QCM	Quartz crystal microbalance
RDF	Radial distribution function
SB	Sulfobetaine
SBMA	Sulfobetaine methacrylate
SEM	Scanning electron microscopy
SPRi	Surface plasmon resonance imaging
SS	Stainless-steel
VMD	Visual Molecular Dynamics Software

Chapter 1
General Introduction

1.1 Overview

Bioelectronics, from biosensors for trace biomolecule detection to neurostimulators for Alzheimer patients, provide innovative therapies that drastically improve people's lives. The performance of bioelectronics, however, is severely hindered *in-vivo* due to our body's inherent immune response[1-3]. Upon surgical insertion, the body spontaneously smears the surface of any bioelectronic with a layer of plasma proteins[4] to identify the device as foreign and attempts to destroy or isolate the implant. In most cases, development of successful implantable biosensors and neurostimulators has been severely hindered due to unreliable *in-vivo* performance after a few hours or days[5, 6]. As a result, there is an increasing demand for a more biocompatible surface that resists nonspecific plasma protein fouling to prolong the *in-vivo* lifetime of implantable bioelectronics.

Traditionally, the biocompatibility and protein-resistivity of a surface are enhanced through a surface coating composed of long hydrophilic polymer chains. Ethylene glycol (EG) and its derivatives are perhaps the most representative and well-studied hydrophilic antifouling material[7]. By forming a strong hydration shell, EG coated surfaces demonstrated a decreased interaction with the biological environment[8-11]. Polymerization of ethylene glycol to create a dense layer of PEG brushes provides an additional steric repulsion barrier that further improves protein resistance by introducing an entropically unfavorable compression of polymer chains during the adsorption process[7, 12, 13]. However, recent studies of PEG-based material have reported that enzymatic degradation[11, 14] can occur *in-vivo* to produce toxic metabolites[15] and, in some cases, hypersensitive reactions up to anaphylactic shocks[16] have been reported.

As a result, recent research focuses have shifted towards finding PEG alternatives that are more biocompatible and biostable.

Bioinspired by zwitterionic phosphatidylcholine (PC) headgroups of phospholipids that constitute the external mammalian cell membranes[17] zwitterionic surfaces have demonstrated a strong resistance against biofouling[18]. Zwitterions, composed of an equal amount of opposite charges in close proximity, preserve net charge neutrality and often outperform traditional hydrophilic polymers in resisting biofouling[19]. Integration of zwitterionic monomers (methacryloyloxylethyl PC) into bulk polymer material (hydroxyethyl methacrylate) to improve biocompatibility and reduce fouling have since been ubiquitous (omafilcon A, a commercially available contact lens material[20]). Zwitterion-based coatings had undergone many iterations in the past decade[7] and are recognized as the next-generation antifouling material. However, existing zwitterionic coatings are composed of long-chain polymer brush and are often undesirable for bioelectronics especially devices designed for electrotherapy as the therapeutic electric pulse decays proportionally with respect to coating thickness. Hence, there is a need for an ultra-thin monolayer of highly zwitterionic coating that does not interfere with the underlying bioelectronic.

This research project exploits the inherent biocompatibility and zwitterionic nature of the amino acid cysteine to produce a monolayer of ultra-thin and highly zwitterionic antifouling coating. This study investigates the antifouling mechanisms of cysteine coatings through molecular dynamic simulation and derives its adsorption kinetics through experimental results. Then, the fabrication processes are optimized in order to minimize coating thickness while maximizing hydration and zwitterionic percentage. Characterization tools used in this study include scanning electron microscopy (SEM), ellipsometry, X-ray photoelectron spectroscopy (XPS), bicinchoninic acid protein assay (BCA), quartz-crystal microbalance (QCM) and surface plasmon resonance imaging (SPRi). The monolayer cysteine coatings are deployed to resist biological fouling from homogeneous mixtures of protein that are known to cause

adverse host response as well as complex biological media. Some of the avenues that will be pursued in future studies are improved zwitterionic percentage, coating stability *in-vitro* and specific understanding of the components in blood that has a higher affinity towards cysteine coatings.

1.2 Research objectives

The success of current bioelectronics is severely hindered by the rapid deterioration of device performance after implantation. Upon surgical insertion, biomaterials and bioelectronics are spontaneously smeared with a layer of plasma proteins which triggers a cascade of undesirable host responses that results in device failure. Thus, by controlling nonspecific protein adsorption, the degree of undesirable host responses can be minimized and implant functionality can be prolonged.

Prolonging the *in-vivo* lifetime of bioelectronics requires an engineered surface that is biocompatible, resistant to nonspecific protein adsorption and does not interfere with the device function. This research focuses on developing an ultra-thin and highly zwitterionic antifouling coating that is also biocompatible and cost-effective to fabricated. Cysteine is a small biomolecule and by controlling the fabrication process, a monolayer coating in the sub-nanometer range can be achieved. This property is essential for applications such as implantable electrotherapeutic devices where the curative electric signal decays with respect to coating thickness. Due to the protonation of the amine group and the deprotonation of the carboxyl group, cysteine is 99.95% zwitterionic in physiological pH and the charge groups are in close proximity to be an effective zwitterionic antifouling material. Biocompatibility is inherently achieved by cysteine, an amino acid that exists in, and is produced by, our body. Fabricating a cysteine coating is both cost-effective and versatile. The single-molecular nature of the monolayer coating requires trace quantity of reagent and the established thiol chemistry can be completed at room temperature without any complex equipment. Fabrication through solution chemistry also allows for the coating of non-planar surfaces and

is useful for coating curved or ridged surfaces that are challenging for other coating processes such a vacuum deposition. The specific objectives of the project are as follows:

1. Develop an understanding of the antifouling mechanism of zwitterionic cysteine and its adsorption kinetics onto a gold surface.
    - Investigate the hydration of cysteine, mainly the number of water molecules associated with each charged group, through molecular dynamics and develop an understanding towards the effect of water mobility within the moieties' hydration shell have on its protein resistivity.
    - Determine the adsorption model of cysteine onto a gold surface and quantify the rate constants.
2. Demonstrate that a zwitterionic cysteine coating can be fabricated on a gold surface and is capable of resisting protein fouling.
    - Fabricate zwitterionic cysteine coatings onto a gold surface and investigate coating integrity.
    - Determine these coatings' thickness, zwitterionic percentage, and resistivity towards biological media.
3. Optimize the fabrication process to create and characterize an ultra-thin monolayer of highly zwitterionic cysteine.
    - Investigate the effect of reaction time, temperature and post reaction wash on coating properties.
    - User various characterization tools demonstrate that a monolayer is achieved and determine thickness.

4. Demonstrate that a monolayer of zwitterionic cysteine is capable of resisting both homogeneous protein mixtures and complex heterogeneous biological media.
    - Quantify the antifouling performance of the coating towards homogeneous mixtures of protein that are known to cause adverse host responses, such as serum albumin and fibrinogen.
    - Quantify the antifouling performance of the coating in a complex biological medium by using human blood.

1.3 Thesis Outline

Chapter 1 provides a general introduction to the thesis, where the research problem, overriding objective, and specific deliverables are outlined. Chapter 2 reviews current progress on antifouling materials composed of hydrophilic polymers, zwitterionic polymers and nanoscale patterns that are used for bioelectronics, tissue engineering, contact lenses, marine membranes and drug delivery. Discussions are focused on the advantages and limitations of each category of material and this review demonstrates that there is a growing drive for a zwitterionic antifouling surface that is both biocompatible and does not hinder the function of the underlying bioelectronic.

Chapter 3 provides a proof-of-concept for implementing zwitterionic cysteine coating on a gold surface to significantly reduce nonspecific protein fouling compared to stainless steel and untreated gold surfaces. Characterizations are made to determine, coating thickness, molecular integrity, and zwitterionic percentage. This chapter demonstrates the feasibility of zwitterionic cysteine as an effective antifouling material as well as that there is room for improvement.

Chapter 4 investigates the antifouling mechanisms of zwitterionic cysteine from a molecular dynamics perspective. Discussions focus on zwitterionic materials and how their antifouling mechanisms suppress

those employed by the traditional hydrophilic material. Topics discussed include the degree of hydration, the structure of surrounding water, the residence time of associated water molecules, the effect of ion-coupling, and benefits of steric repulsion. Special emphases are made on zwitterionic cysteine and molecular dynamics simulations are performed to investigate the molecule's hydration later. Results are compared against other zwitterionic antifouling materials currently available.

Chapter 5 optimizes the fabrication of cysteine coatings based on previous successes demonstrated in chapter 3. By controlling the reaction temperature, the zwitterionic fraction of the surface is significantly improved. Using a liquid interface quartz-crystal microbalance, the adsorption kinetics of zwitterionic cysteine onto a gold surface is monitored in real-time and the rate constants are calculated.

Chapter 6 quantifies the antifouling performance of the coating towards homogeneous mixtures of protein that are known to cause adverse host responses, such as serum albumin and fibrinogen. A monolayer coating is achieved and coating thickness is determined to be less than one nanometer. The antifouling performance of the coating in a complex biological medium is also studied by using human blood.

Chapter 7 presents the conclusions drawn from this research project and based on these conclusions, provides recommendations for future research avenues. Impactful future research includes investigating the in-vitro stability and biocompatibility of the zwitterionic coating. Another key research area is to understand the mechanisms of adsorption between different components of blood and determine whether any specific component exhibits a higher affinity towards adsorption onto the coating. Furthermore, analytical instruments with higher sensitivity can be employed to obtain additional meaningful information on various physical properties of the coating, such as surrounding water structure and associated ion-coupling.

Chapter 2
Literature Review

2.1 Summary

For implantable bioelectronic devices, the interface between the device and the biological environment requires significant attention as it dictates the device performance *in-vivo*. Nonspecific protein adsorption onto the device surface is the initial stage of many degradation mechanisms that will ultimately compromise the functionality of the device. In order to preserve the functionality of any implanted bioelectronics over time, protein adsorption must be controlled. This chapter outlines two major approaches to minimize protein adsorption onto the surface of implantable electronics. The first approach is through a surface coating technique, which minimizes close proximity interactions between proteins and device surfaces by immobilizing electrically neutral hydrophilic polymers as a surface coating. These coatings reduce protein fouling by steric repulsion and the formation of a hydration layer which acts as both a physical and energetic barrier that minimize protein adsorption onto the device. Relevant performances of various conventional hydrophilic coatings are discussed. The second approach is surface patterning using arrays of hydrophobic nanostructures through photolithography techniques. By establishing a large slip-length via superhydrophobic surfaces, the amount of protein adsorbed on the surface of the device can be reduced. The last section discusses emerging surface coating techniques utilizing zwitterionic polymers where ultralow biofouling surfaces have been demonstrated. These surface modification techniques have the potential to significantly improve the long-term functionality of implantable bioelectronics, thus allowing researchers to overcome challenges to diagnose and treat chronic neurological and cardiovascular diseases.

2.2 Introduction

Advances in nanofabrication and the understanding of human biology have promoted the design of more compact, selective and efficient bioelectronics, which has opened numerous avenues for medical practitioners to diagnose and treat diseases that were previously considered incurable[21-24]. Neurological disorders are extremely difficult to diagnose and treat due to the complexity of the disease. Recent advances in molecular and cell biology have allowed scientists to pinpoint the exact location of several incurable disorders including Alzheimer's disease. According to World Health Organization, there is currently an estimate of 18 million people worldwide with Alzheimer's disease and are projected to nearly double to 34 million by 2025[25]. Recently emerging research has demonstrated promising results utilizing transcutaneous electrostimulation on the central nervous system of Alzheimer's patients to improve memory, alertness[26, 27] and rest-activity rhythm[21] without severe side effects. This example is merely one of the driving forces behind the development of bioelectronics that are capable of synchronizing communication between biological and electrical platforms.

The scope of bioelectronics can be considered to incorporate an exploitation of biology in conjunction with electronics for information processing, information storage, electronic components, and actuators. Miniaturized, implantable bioelectronics—such as neurostimulators and biosensors—are crucial in providing convenient continuous functionality in diagnostic or treatment without the need to interrupt the everyday life of the patients with psychological concerns of their health. Even though there have been numerous successful demonstrations of implantable biosensors and neurostimulators[22-24, 28], the primary challenge of current implantable bioelectronics still revolves around the long-term functionality of the device. In most cases, the development of successful implantable biosensors and neurostimulators has been severely hindered due to unreliable in-vivo performance after a few hours or days.

The success of any implantable bioelectronics depends heavily on preserving the devices' functionality in-vivo throughout the course of the implantation. The implantation period can be chronicled into several stages, each with a distinct host response (Figure 1). Upon surgical insertion of any implantable devices, tissue inflammation and foreign body response are immediately invoked as the initial stage of the body's natural defense system. The short-term host response, or the acute inflammation phase, can last from hours to days depending on the surgical procedure. The next stage of the host response against implanted bioelectronics is indicated by fibrous encapsulation, which is the formation of a layer of fibroblast or smooth muscle cell sheet approximately 50–200μm in thickness to isolate the device [29, 30]. The formation of the fibrous capsule will prevent further interaction of the bioelectronics with the surrounding host environment and compromises the functionality of the device. As a result, implanted bioelectronics often requires a secondary surgery to remove or replace the device. Taking implantable glucose sensors as an example, as of 2010, there are six minimally invasive glucose sensors approved by FDA that provide periodic readings[5]; however, the longest marketed in vivo functionality is 7 days[5]. Aside from the obvious that the fibrous capsule hinders the transport of glucose molecules[5], several investigations indicated that nonspecific protein adsorption also hinder glucose diffusion to the sensor[5, 31, 32]. As a result, in order to prolong the functionality of any bioelectronics, the progression of undesirable host responses must be delayed if not completely prevented.

There are several established strategies for improving the biocompatibility of implantable devices. One approach is by minimizing the acute inflammation phase through refining and enhancing different aspects of the surgical procedure; these methods are often referred to as indirect influences and can generally be applied to implantable bioelectronics regardless of their applications. For example, refining the surgical insertion techniques can minimize the implant injury, which will reduce the degree of homeostatic responses as well as the amount of blood-to-device exposure[33, 34]. Another strategy is the use of steroidal and non-steroidal anti-inflammatory drugs, which can control or even suppress the degree of the immune

response at the implant site. Drugs such as glucocorticoids are known for their ability to inhibit both the formation and secretion of inflammatory mediators and hence, achieving a decrease in capillary permeability, fibroblast proliferation, as well as the release of inflammatory cells at the injury site[35]. There also have been reports of using angiogenic drugs when implanting long-term biosensors in order to improve analyte transport to the sensor[36]. Growth factors such as the vascular endothelial growth factor (VEGF) is capable of promoting the formation of new blood vessels around the implant in order to promote analyte transport to the sensors[37-39]. Note that the above strategies can be, and often are, used in conjunction in order to improve biocompatibility. Although the short-term acute phase can be greatly minimized through external influences, minimizing long-term chronic responses and fibrous encapsulation required direct modification of the implantable device itself. Since invoking host response results in a gradual loss of device functionality followed by complete isolation via fibrous encapsulation, extensive research has focused on preventing nonspecific protein adsorption at the initial stage of the host response. Anti-fouling measures primarily target plasma proteins since they function as the dominating agents in signaling and controlling the initial phases of tissue inflammatory response.

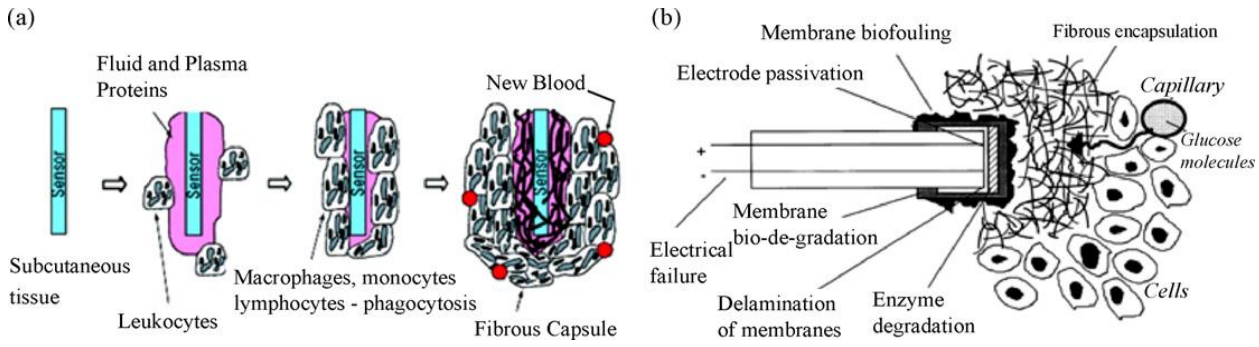

Figure 1: Process of Encapsulation of Biosensors
The process of encapsulation of Biosensors (Santhisagar *et al*., 2010[40]). (Reprinted with permission from [1, 41])

Several distinct approaches to constructing device surfaces have been proposed to minimize nonspecific protein adsorption. All of these approaches, although significantly different in design, ultimately tackle a distinct stage in the protein adsorption process. A typical protein adsorption process

is illustrated in Figure 2. Proteins arrive at the implant site through conductive transport either in blood or tissue fluid. This is often observed in the bulk fluid at a distance that is too far away for any interacting forces to be significant and thus, proteins carried by this flow do not directly contribute to the protein adsorption[42]. However, as in most fluid dynamics, a no-slip boundary condition is assumed to be observed near the device surface where no flow is observed[43]. This region is referred to as the diffusive transport region that is typically 10 μm in length. Proteins that are carried to the site of the implant by conductive transport will diffuse through this diffusion-controlled region before reaching the surface of the device[42]. At this close proximity region (2-5nm), the short range forces, such as hydrogen bonding, van der Waals, and electrostatic forces, are dominant and the interaction between the surface and the protein will determine the extent of protein adsorption.

The surface coating approach focuses on reducing the extent of close proximity forces between protein and implant surface in order to reduce the amount of biofouling. By coating the surface with a layer of more biocompatible molecules, the close range interactions between the device surface and the biological environment can be minimized. In an ideal case, this surface coating will render the device undetectable by preventing the host body from recognizing the implant as a foreign object. This approach will be referred to as the surface coating technique. In addition to simple coating, another approach to creating an anti-biofouling surface is to reduce the diffusive transport region by surface patterning. The theory behind this approach is to reduce the diffusive transport layer, caused by the no-slip condition, between the boundary of the device surface and the fluid. By reducing the thickness of the non-slip zone, one can reduce the amounts of protein reaching and adsorbing onto the device surface[44]. This approach is primarily achieved by patterning the device surface with arrays of hydrophobic nanostructures through various photolithography techniques. These rough hydrophobic surfaces will create a huge gas-fraction (or air bubbles) on the device surface and increase the slip-length. Lee *et al.*[44] has reported that by surface patterning a silicon wafer with a "grate" design, a slip length as large as 185 μm can be achieved.

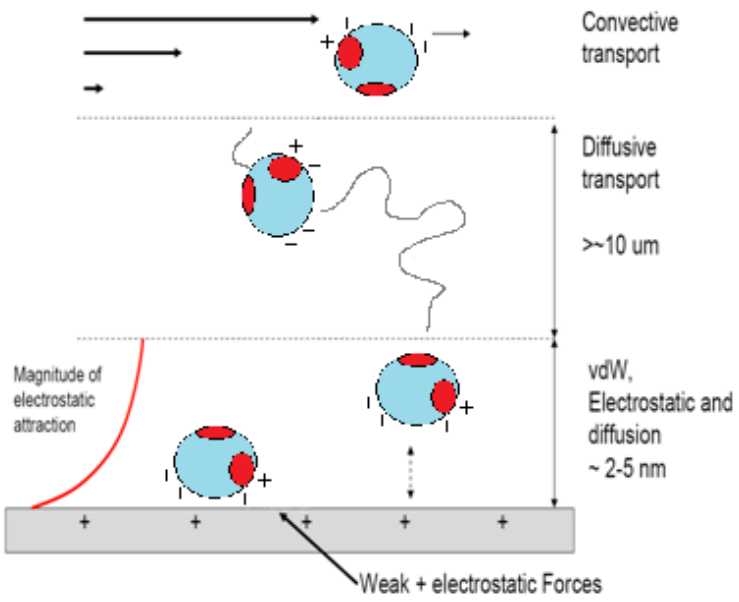

Figure 2: Schematic representation of the protein adsorption process.
Outlining the conductive transport region (top), diffusive transport region (middle), and close proximity region (bottom).

2.3 Surface Coating

Numerous polymers have demonstrated promising results in resisting nonspecific protein adsorption (Tables 1 and 2). Many of these, such as poly(ethylene glycol) (PEG) and poly(lactic-co-glycolic acid) (PLGA), have been approved by the Food and Drug Association (FDA) for use in human applications and continue to be the primary materials used for anti-biofouling[45-48]. All of these polymers exhibit two major characteristics that are hypothesized to be responsible for their anti-biofouling capabilities. The first is electrical neutrality[49]; polymers that are electrically neutral demonstrate a reduced amount of coulombic interaction with various charged domains of the protein. This will ensure that even upon contact, the proteins will not adhere strongly to the polymer coating. The second commonly shared characteristic between these polymers is hydrophilicity[50]. The most established reason behind the resistive property of hydrophilic polymers is the formation of a hydration layer on the surface of the

coating. This layer of water molecules is tightly bound through hydrogen bonding[19, 51] and acts not only as a physical barrier but also as an energetic barrier that the proteins have to overcome in order to adsorb onto the surface. The polymers used for surface coating can be categorized into two major classes. Traditionally, researchers focus on using hydrophilic polymers as a surface coating material; however, reports have demonstrated promising results of zwitterionic polymers and small biomolecules as an ultralow-biofouling surface (<0.3ng/cm^2). The following section will first investigate the effect of a hydration layer and be followed by outlining the recent achievements of surface coating using traditional hydrophilic polymers, such as PEG and dextran, on biosensors and neural stimulation electrodes.

2.3.1 Surface Hydration

Hydrophilic coatings are known to facilitate the formation of a hydration layer through hydrogen bonding between the surface and the solvent[50]. This layer of tightly bound water molecule will not only act as a physical barrier but also as an energetic barrier that the proteins have to overcome before adsorbing onto the device surface[51-55]. The effect of the water barrier can be analyzed thermodynamically in the same fashion as the dehydration process and is entropically unfavorable[56]. The expulsion of water molecules at the surface to allow for the adsorption of protein is analyzed theoretically and through simulations in various accounts[34, 52, 53]. Zheng *et al.*[51] has predicted the repulsive force towards proteins by surfaces coated in the descending order of OEG-SAMs, OH-SAMs, and CH3-SAMs. Figure 3 illustrates surface-to-protein repulsive forces as a function of separation distance. The OEG-SAMs, being the most hydrophilic of the three materials, demonstrated the sharpest increase in repulsive force as the protein moves closer to the surface, which agrees with experimental results[57]. On the other hand, CH3-SAMs, being hydrophobic, demonstrated the least increase in repulsive forces. Zheng *et al.*[51] concluded that the tightly bound hydration layer adjacent to the OEG-SAMs is the primary contributing factor for the SAMs' larger repulsive hydration force compared to the other two surfaces.

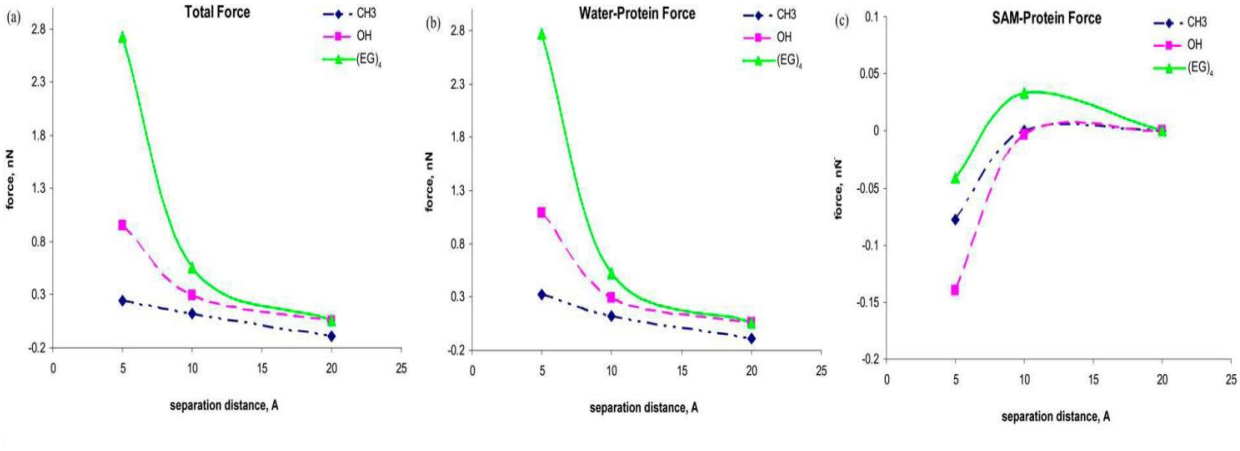

Figure 3: Molecular dynamics simulation of hydration effect
Repulsive force as a function of separation distance for OEG-SAMs, OH-SAMs, and CH3-SAMs for a) total force, b) forces contributed by water, and C) forces contributed by SAM[51] (Reprinted with permission from Zheng *et al.*, 2005. Copyright 2005 Elsevier)

The effect of the surface hydration layer as one of the primary contributing factors of anti-biofouling was demonstrated experimentally by several groups[55, 58, 59]. The most conclusive investigation is perhaps the one done by Warkentin where a hydrophilic silica surface is modified with different concentration of hydrophobic methyl groups, resulting in a hydrophilic gradient across the surface (Figure 4)[59]. As illustrated, a sudden increase in protein adsorption occurs at >45° contact angle, where the surface switches from being hydrophilic to hydrophobic. The hydrophilic portion of the surface (<45°) forms a hydration layer through hydrogen bonding and exhibits significantly less protein adsorption. On the other hand, the hydrophobic surface causes the dehydration process to become entropically favorable and the expulsion of water occurs rapidly, which facilitates protein adsorption. This expulsion of water is driven in a similar fashion as the release of water cage around hydrophobic tails in micelle formation. Similarly, Tsai *et al.*[60] has demonstrated that by modifying the hydrophobic polyurethane with the more hydrophilic dextran, the amount of protein adsorbed is reduced to less than half for numerous plasma proteins including serum albumin, fibrinogen, and haptoglobin (Hp2).

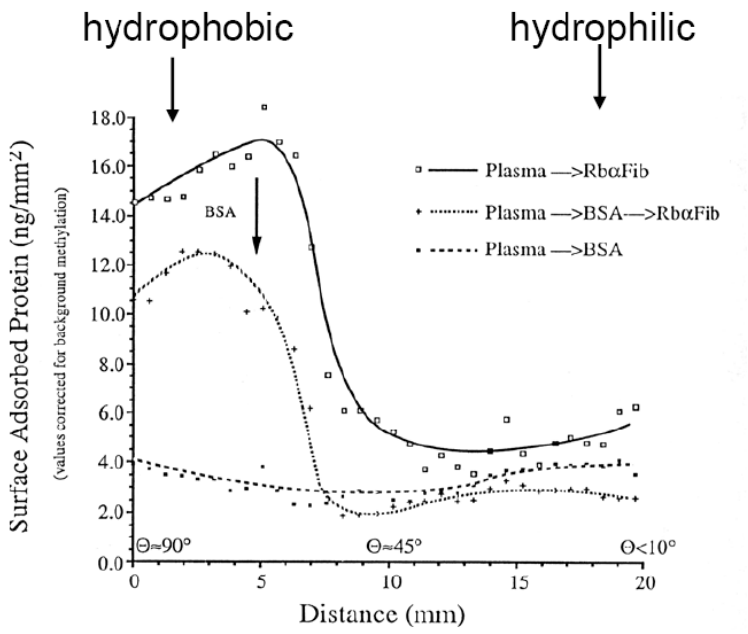

Figure 4: Hydration Effect on Protein Adsorption
Ellipsometric reading of 1) plasma adsorption, 2) Fibrinogen antigen strength due to the presence of BSA blockage on a hydrophobic gradient surface achieved by treating silica with different amounts of methyl[59]. (Reprinted with permission from Warkentin *et al*., 1995. Copyright 1995 American Chemical Society.)

Based on these simulations and experimental results, the stronger the interaction between the water solvent and the surface coating, the more unfavorable the dehydration process becomes, and the more resistant the surface will be towards protein adsorption. It is also reasonable to predict that both the intrinsic physiochemical properties as well as the surface density of the surface coating are the primary contributing factors to the strength of the hydration layer. Chen *et al.*[58] has hypothesized that the water molecules will be more localized and more tightly bonded to the charged groups for zwitterionic surfaces and to the polar head for SAM; whereas, the distribution of water molecules are fairly random for hydrophilic polymers (Figure 5)[58].

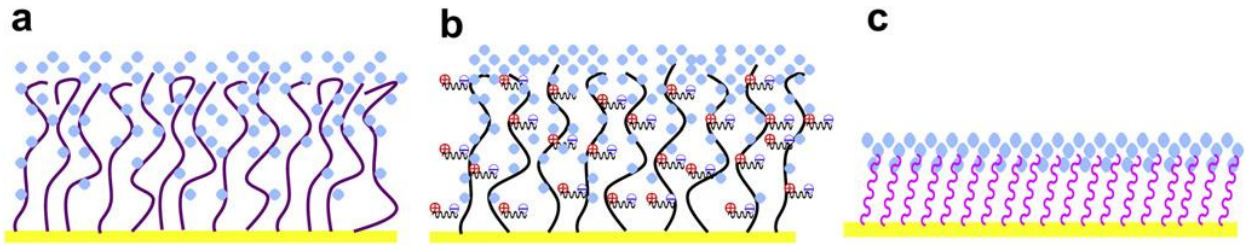

Figure 5: Schematic representation of a hydration layer.
With blue dots representing water molecules interaction with a) hydrophilic surface, b) zwitterionic surface, and c) self-assembled monolayer (SAM). Note that the water molecules are randomly distributed on the hydrophilic surface but concentrated in close proximity to the charge groups for zwitterionic surfaces and to the polar head for SAM[58]. (Reprinted with permission from Chen *et al.*, 2010. Copyright 2010 Elsevier)

2.3.2 Hydrophilic Polymer

Surface coating with hydrophilic polymers often utilizes long-chain polymers where both the hydration layer and steric repulsion will contribute to resisting biofouling. Steric repulsion occurs when the long polymer chains are compressed due to the adsorption of proteins. The compression forces the surface polymers to undergo unfavorable configuration changes and result in an unfavorable decrease in entropy, resulting in an entropically driven repulsion force to prevent nonspecific protein adsorption. For long-chain hydrophilic polymer coatings, both packing density and the functional group are of great significance. Poly(ethylene glycol) (PEG) is arguably the most common anti-biofouling polymer that is currently available. The primary reasons for the anti-fouling characteristic of PEG can be attributed to the formation of a highly hydrated layer, high steric repulsion due to high chain mobility, and large exclusion volume. Luesse and Arnold have demonstrated that a maximum of one water molecule per ethylene glycol repeat unit ($-CH_2CH_2-O-$) can be observed through deuterium NMR relaxation time; indicating a significant degree of hydration[61]. Numerous approaches have been investigated to modify surfaces with PEG-based materials including physisorption[62, 62-64], chemisorptions[65, 66], covalent grafting[67, 68], and plasma polymerization[69, 70]. The performance of PEG-based and other hydrophilic polymer coatings is summarized in Table 1 and Table 2 (adapted from Chen *et al.*[58]). Table 1 focuses on various reporting of PEG-based materials exhibiting distinguished results as a surface coating material.

The PEG-conjugated drug is known to prevent recognition by the patient's immune system[71]. Alconcel *et al.* have reported a list of PEGylated protein drugs that are approved by FDA as of January 2011[48]. However, recent in-vitro studies of PEG-based material have only demonstrated short-term stability that is hypothesized to be caused by oxidation stresses in biological environment[72, 73]. As a result, recent research focuses have shifted towards finding alternative anti-biofouling polymers that are bio-mimicking in nature. Table 2 summarizes various PEG-alternative materials used for antifouling. Dextran is a complex and branched polysaccharide that mimics the carbohydrate-rich portion of inner surface of blood vessels known as the endothelial glycocalyx[74, 75]. By mimicking the endothelial glycocalyx, dextran coated surfaces are believed to be a promising candidate for reducing thrombosis and inflammation[76]. Tsai *et al.*[60] have explored the capability of the dextran-coated surface in resistant to the adhesion of various human blood plasma protein through a two-dimensional electrophoresis analysis technique[60]. The effect of a dextran-coated surface on hydrophobic polyurethane (PU) and hydrophilic silicon was reported. Both surfaces were submerged in human blood clinically acquired by adult volunteers and electrophoresis analysis returned that nonspecific protein adsorption is reduced by ~50% for all blood plasma proteins in both polyurethane (hydrophobic) and silicon (hydrophilic) surfaces[60].

Table 1: Summary of anti-biofouling hydrophilic polymer
(Adopted from Chen *et al*.[58])

	Material	Demonstrated Resistance to Protein Adsorption	Demonstrated Resistance to Cell Adhesion
PEG-based materials	**PS-g-PEGMA, PMMA-g-PEGMA**[77]	BSA	-
	PEG-poly(phosphonate) terpolymer[78]	Serum Protein (4 ± 1 ng/cm^2)	-
	PLL-g-PEG[79, 80]	Serum Protein (<5 ng/cm^2)	Fibroblast, Osteoblasts, Epithelial cell
	PEGMA[81, 82]	Fibrinogen	-
	PPEGxLys[83]	BSA, Fibrinogen	-
	POEGMA[84-87]	Fibrinogen, Serum Protein, platelet	Bacteria (*S. epidermidis& P. aeruginosa*) reduce 87%
	PEO-PU-PEO[65, 88-90]	Fibrinogen, C3, Akbumin, Apolipoprotein AI	-
	PEO-PPO-PEO[91]	Fibrinogen	-
	PEO[92]	Analytical	-
	PEG[9-11, 93, 94]	BSA, Alginic acid	Microbial, Fibroblasts, Bacteria (*Staphylococcus aureus, Klebsiella pneumonia, Pseudomona*sp.*)*
	mPEG-DOPA[64, 95]	Serum Protein	Fibroblasts
	mPEG-MAPD[95]	-	Fibroblasts
	OEG-SAM[87, 96, 97]	Fibrinogen, Serum Protein, platelet, lysozyme, BSA	-

Table 2: Summary of anti-biofouling hydrophilic polymer (continued)

PEG Alternatives	**PMOXA**[98, 99]	Serum Protein (<2 ng/cm^2)	Bacteria (*E. coli*)
	Glycerol Dendron[100]	Fibrinogen, Lysozyme, Albumin, Pepsin	-
	HPG Dendron[101]	BSA, Immunoglobulin	-
	Tetraglyme[102-105]	Fibrinogen (<10 ng/cm^2), Platelet, Serum Protein	Leukocyte, Monocyte
	Dextran[76]	Serum Protein, albumin, lysozyme, collagen	-
	Polysaccharide[106]	lysozyme, HSA, IgG, bovine colostrum lactoferrin	-
	Poly(HEMA)[107, 108]	-	Fibroblast, Bacteria (*Salmonella typhimurium*)
	PVA[109]	Myoglobin	-
	Polyamines functionalized with acetyl chloride[110]	Fibrinogen, Lysozyme	Bacteria (*Staphylococcus epidermidis*, *Staphylococcus Aureus*)
	Mannitol-SAM[111]	Fibrinogen, Lysozyme, Pepsin, Insulin, Trypsin	Fibroblast
	Peptide-based SAM[112]	Streptavidin, BSA, Fibronectin	-

2.4 Surface Patterning

In addition to surface coating, another approach to creating anti-fouling surfaces is to reduce the diffusive transport region in the protein adsorption process (Figure 2). This is an indirect approach to reducing protein adsorption; by reducing the length of the diffusive transport region, the amounts of protein actually arriving at the surface can be minimized. The extent of the diffusive transport region is inversely proportional to the slip length; a large slip length is an indication of a small diffusive transport region. Koc *et al.* have demonstrated that protein adsorption can be greatly reduced by patterning the surfaces with nanostructures[113]. Through sol-gel chemistry, different grain sizes of silica can be deposited onto standard microscope glasses in order to create surfaces with different roughness. The surfaces are then terminated by either hydrocarbon or fluorocarbon. As discussed previously in Chapter 2.3, the hydrocarbon-terminated surfaces tend to form a stronger hydration layer and hence demonstrated less protein adsorption when compared to the fluorocarbon-terminated surfaces[113]. However, this is not the case for surfaces that are modified with nanostructures. By patterning the surfaces with hydrophobic nanostructures that are small enough (10 nm) to stabilize the dewetted state, the amount of adsorbed protein is reduced by half (Figure 6)[113]. Moreover, Koc *et al.* had further demonstrated that if the surfaces are subjected to a very low shear flow (equivalent to 3 μL/min), almost no protein adsorption is observed on the dewetted surface (Figure 6: 10 nm). This antifouling property can be explained by analyzing the diffusive transport region of the protein adsorption process (Figure 2). By patterning a surface with hydrophobic nanostructures, the surface is stabilized in a dewetted state and hence has a smaller diffusive transport region (Figure 2)[44]. It is suggested that more proteins are carried away from the surface by the flow as opposed to arriving at the surface due to diffusion. By creating a smaller diffusive transport region (or a larger slip length) through nano-patterning, Koc *et al.* have successfully created an antifouling surface.

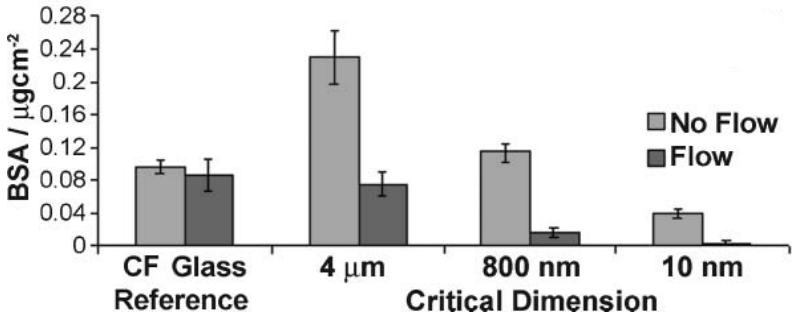

Figure 6: Effect of Surface Roughness on BSA Adsorption
BSA adsorption onto fluorocarbon-terminated surfaces with different scale of roughness[113]. (Reprinted with permission from Koc *et al*., Copyright 2008 Royal Society of Chemistry)

By using an organized surface pattern as opposed to a randomized roughness, the diffusive transport region can be further minimized. Lee *et al.* have reported that a very large slip length can be achieved by patterning the device surface with arrays of organized hydrophobic nanostructures through photolithography and deep reactive ion etching[44]. The principle behind designing a surface with a large slip length is focused on stabilizing a large gas fraction (or an air bubble) between hydrophobic structures[114]. Stabilizing the surface in a dewetted state with a large gas fraction will minimize the interface between the solid and the liquid and hence realizing a large slip length[114]. Lee *et al.* have demonstrated two methods of increasing the gas fraction: 1) by reducing the size of the nanostructure, and 2) by increasing the pitch between each nanostructure. Two nanostructures, post and grate, were investigated under different pitch length and size percentage (Figure 7). Investigations demonstrated that rapid increase of slip length is observed after 95% removal of substrate[44]. Lee *et al.* had demonstrated a slip length as large as 185 μm can be achieved by using a grate design with a pitch size of 210 μm (Figure 7 bottom). Note that the increase of slip length with respect to pitch is higher for post designs as illustrated by the bottom panel of Figure 7; however, it is a lot more difficult to stabilize the post-patterned surface in a dewetted state. Therefore, the maximum slip length for the post design is ~100 μm at a pitch of 60 μm (Lee *et al*., 2008). By combining the design proposed by Koc *et al.* with that by Lee *et al.*, it is possible to achieve ultralow-biofouling surfaces through surface patterning with organized arrays of hydrophobic

nanostructures. Current issues regarding this approach revolve around the fragility of the nanostructures during device handling as well as the possibility of surface contaminations that will further destabilize the de-wetted state of the surface.

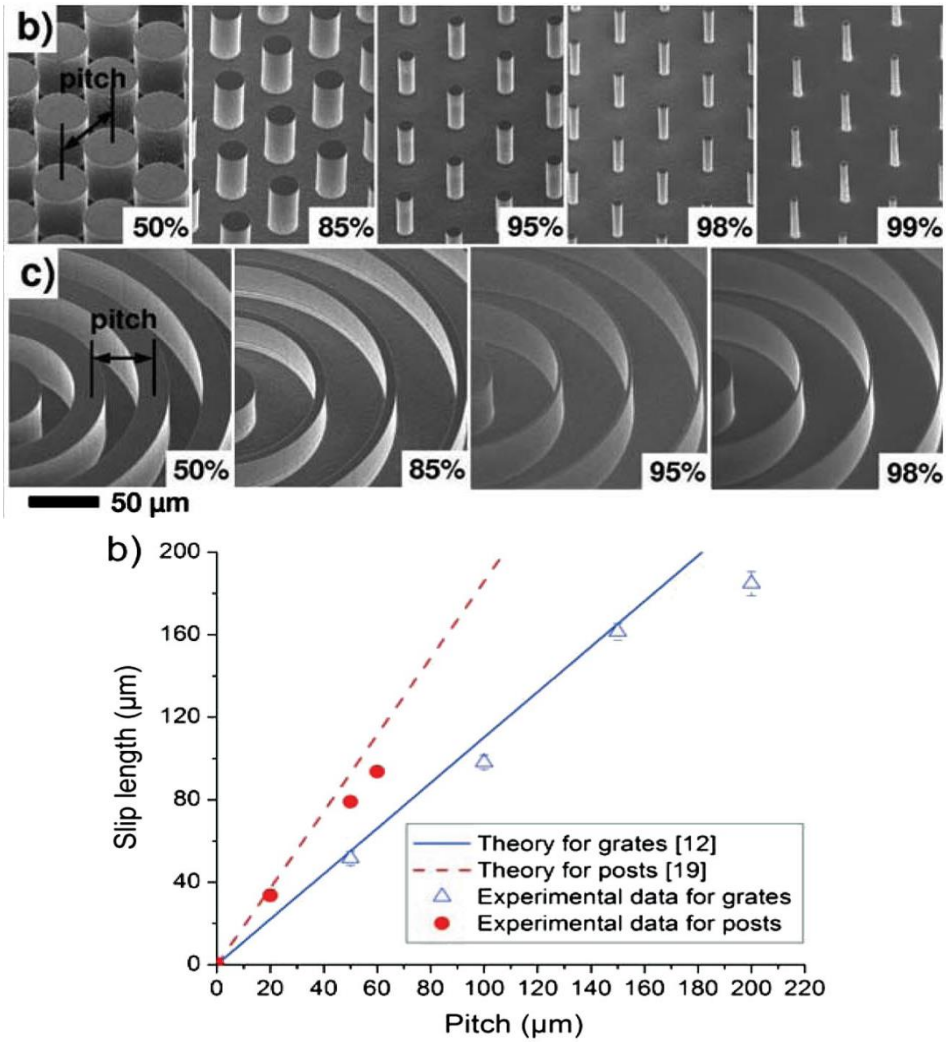

Figure 7: Effect of different Surface Patterns on Slip Length
The effect of different surface patterns (top) on the slip length under different pitch size (bottom). Note that a large slip length translates to a small diffusive transport region[44]. (Reprinted with permission from The American Physical Society. Copyright 2008 by The American Physical Society)

2.5 Zwitterionic Surface Coating

Zwitterionic coatings are a recently emerging surface modification material that have demonstrated promising results as a candidate for creating ultralow-biofouling surfaces[115-118]. Zwitterionic polymers are composed of an equal ratio of both positive and negative charge groups in close proximity and thus, maintaining electrically neutral. The positive and negative charge groups can be expressed on the same monomer, known as polybetaines, or on separate monomer units in a mixed charge complex, known as polyampholytes. When designing a zwitterionic polymer coating, obtaining a uniform charge distribution of the opposite charges is critical to maintaining electrical neutrality.

Similar to hydrophilic polymers, zwitterionic polymers form a hydration layer. However, in this case, the formation of hydration layer is facilitated through ionic solvation which is reported to be stronger than that formed by a hydrophilic coating[19]. As expected, recent designs of anti-biofouling surfaces utilizing various zwitterionic materials have demonstrated promising results (Table 3); a report of an ultra-low protein adsorption ($<0.3 ng/cm^2$) has been achieved by using polyampholytes consisting of alternating amino acids Glu/Lys or Asp/Lys[118]. In addition, zwitterionic polymers are also versatile and the application does not limit only to surface coating. Yang *et al.* demonstrated a glucose sensor can be stabilized *in-vitro* for 12 days by encapsulating the device with a hydrogel conjugated with zwitterionic carboxybetaine methacrylate (CBMA)[116].

The performance of various zwitterionic polymers is summarized in Table 3. Although numerous reports have demonstrated promising results utilizing zwitterionic polymers (such as CBMA and pMPC), the chain-length of these polymers greatly hinders their attractiveness in micro or nano-systems. By coating these systems with long polymers chains, the systems lose their useful activities such as large surface-to-volume ratio. This promotes the search for novel surface coating materials that are small and naturally exist inside the body, such as amino acids.

Cysteine is a promising candidate for zwitterionic surface coating due to its small size, zwitterionic nature, and accessible thiol group which allows for established surface chemistry with major platforms for bioelectronics such as gold and silicon. Rosen *et al.* have reported that only ~9 nm increase in nanoparticle diameter is observed by coating commercial silicon nanoparticles with cysteine, whereas the stability of the coated particles is significantly increased in human serum and BSA[117]. Ma *et al.* reported that by reacting cysteine with gold nanoparticle precursors under various pH, the average particle size and particle size distribution can be tailored; an increase in pH result in smaller particle size[119]. This is hypothesized to be caused by: 1) the reducing capability of cysteine increases with pH, and 2) the deprotonation of the amino group at pH >pKa of 10.07.

Fabrication and characterization of a monolithic layer of cysteine on gold were reported by Gonella[120]. Figure 8 illustrates high-resolution x-ray photoelectron spectroscopy (HR-XPS) references indicating the presence of sulfur and surface interaction (sulfur 2p), the presence of unaltered cysteine (carbon 1s), and the ratio of zwitterionic state (nitrogen 1s).

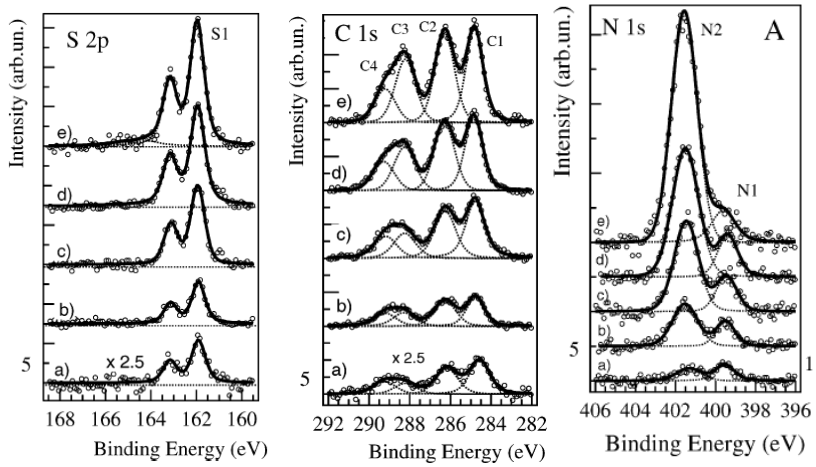

Figure 8: HR-XPS result of Sulfur 2p, Carbon 1s, and Nitrogen 1s
These series of spectra indicate the presence of sulfur and surface interaction (left), the presence of cysteine (middle), and the ratio of zwitterionic state with N1 and N2 representing NH_2 and NH_3^+ respectively (right). For all curves, a) – e) represent the surface coverage ranging from 0.14, 0.33, 0.62, 0.8, and 1 monolayer[120]. (Reprinted with permission from Gonella *et al.*, 2005. Copyright 2005 American Chemical Society.)

Table 3: Summary of anti-biofouling Zwitterionic polymer

Material		Demonstrated Resistance to Protein Adsorption	Demonstrated Resistance to Cell Adsorption
Polybetaine	**Poly(CBAA)**[66, 87, 102, 121-123]	Fibrinogen, Serum Protein, Platelet, DNA	Bacteria (S. epidermidis& P. aeruginosa)
	Poly(SBMA)[86, 87, 124, 125]	Fibrinogen, Serum Protein, Platelet, Lysozyme	Bacteria (Pseudomonas aeruginosa)
	Poly(CBMA)[126, 127]	Fibrinogen, Lysozyme, hCG	Bacteria (*Escherichia coli*)
	Poly(MPC)[108, 128, 129]	Serum Protein, Platelet	Fibroblast
	PC-SAM[87, 97]	Fibrinogen, Serum Protein, Platelet,	Bacteria (*S. epidermidis& P. aeruginosa*)
	OPC-SAM[56, 87, 97]	Fibrinogen, Serum Protein, Platelet, BSA, Lysozyme	Bacteria (*S. epidermidis& P. aeruginosa*)
Polyampholyte	**SA/TMA-SAM**[87, 97, 130]	Fibrinogen, Serum Protein, Platelet, BSA	Bacteria (*S. epidermidis& P. aeruginosa*)
	CA/TMA-SAM[87, 97, 130]	Fibrinogen, Serum Protein, Platelet, BSA	Bacteria (*S. epidermidis& P. aeruginosa*)
	PM/TMA-SAM[87, 97, 130]	Fibrinogen, Serum Protein, Platelet, BSA	Bacteria (*S. epidermidis& P. aeruginosa*)
	Peptide surfaces derived from natural amino acids [118]	Fibrinogen, Albumin, Lysozyme	-
	Poly(TM-SA)[69]	Fibrinogen, BSA, Lysozyme	-
	Poly(METMA-MES)[131]	Fibrinogen, BSA, Lysozyme	-
	PDDA/PSS[132]	tTGase, β-galactosidase, Lysozyme	-

2.6 Conclusion

Recent advances in nanofabrication and surface chemistry have promoted numerous novel approaches to designing more compact, selective and efficient bioelectronics. However, for any biomedical applications, the interactions at the interface between the device and the biological environment require significant attention as it often governs the functionality of the device over time. Foreign body response, and among other degradation mechanisms, are initiated through non-specific protein adsorption; therefore, in order to improve the in-vivo lifetime of the implanted bioelectronics, biofouling must be minimized. Currently, there are two major approaches to minimize nonspecific protein adsorption. The first approach minimizes the close proximity interactions between proteins and the device surface by immobilizing electrically-neutral hydrophilic or zwitterionic polymers as a surface coating. Ultralow-biofouling surfaces (<0.3 ng/cm^2) have been demonstrated through zwitterionic coatings of alternating Glu/Lys or Asp/Lys. Cysteine is a promising coating material for nanoscale systems because of its small size, zwitterionic surface, and improved biocompatibility of nanoparticles. We believe that future surface coating materials may focus on zwitterionic biomolecules, such as amino acids, as a PEG-alternative. The second approach to creating anti-biofouling surfaces is to reduce the diffusive transport layer by patterning the device surface with hydrophobic nanostructures; this method indirectly reduces protein adsorption by reducing the amounts of protein arriving at the surface. The current challenges with the surface patterning approach consist of designing and fabricating more durable surface patterns in order to withstand normal handling of the device during implantation. By applying various surface modification techniques discussed in this review, significant improvements were demonstrated on several devices' long-term in-vivo functionality, which has always been a major challenge for implantable bioelectronics.

Chapter 3
Development of an Antifouling Surface Using Cysteine

3.1 Summary

Applications of implantable bioelectronics for analytical and curative purposes are currently limited by their poor long-term biofunctionality in physiological media and nonspecific interactions with biomolecules. In an attempt to prolong *in-vivo* functionality, recent advances in surface modifications have demonstrated that zwitterionic coatings can rival the performance of conventional poly(ethylene glycol) polymers in reducing nonspecific protein fouling. This chapter reports the fabrication of a very thin layer of nonfouling zwitterionic cysteine surface capable of protecting implantable bioelectronics from nonspecific adsorption of plasma proteins. In this proof-of-concept, a cysteine surface exhibiting zwitterionic state as high as 88% was fabricated through solution chemistry, and demonstrated a reduced fouling from bovine serum albumin (BSA) and human serum. The fabricated surface utilized a minimal amount of gold substrate, approximately 10 nm, and an extremely thin antifouling layer at 1.14 nm verified by ellipsometry. X-ray photoelectron spectroscopy assessment of the nitrogen (N1s) and carbon (C1s) spectra conclude that 87.8% of the fabricated cysteine surface is zwitterionic, 2.5% is positively charged, and 9.6% is noncharged. The anti-biofouling performance of a cysteine surface is quantitatively determined by bicinchoninic acid (BCA) protein assay as well as qualitatively confirmed using scanning electron spectroscopy. Cysteine surfaces demonstrated a BSA fouling of $3.9 \pm 4.84\%$ $\mu g/cm^2$, which is 93.6% and 98.5% lower than stainless steel and gold surfaces respectively. Surface plasma resonance imaging analysis returned similar results and suggest that a thinner cysteine coating will enhance performance. Scanning electron microscopy confirmed the results of BCA assay and suggested that cysteine surface demonstrated a 69% reduction to serum fouling. The results reported in this report demonstrate that it is possible to achieve a highly zwitterionic surface through solution chemistry on a

macroscopic level that is capable of improving the biocompatibility of long-term implantable bioelectronics.

3.2 Introduction

Recent advances in microfabrication techniques have opened numerous new avenues for implantable bioelectronics such as implantable biosensor[116], neuron stimulators[133], and electrode-based pain-control treatments[6]. For nearly all biomedical applications, the interface between the implanted device and the biological environment is of great significance and often dictates the performance of the device in-vivo. As reviewed in Chapter 2, biofouling in the form of nonspecific protein adsorption is one of the major contributions to device failure for implantable bioelectronics, especially for surface-based diagnostic devices[5, 31, 32]. For neuro-stimulating electrodes, biofouling is even more detrimental as the effective electric signal decays proportionally with the thickness of the adhered biomass as governed by Coulomb's law.

Zwitterionic molecules have demonstrated promising characteristics as antifouling coating materials[49, 134], and are capable of achieving ultra-low protein adsorption in the range of <0.3 ng/cm^2 [7, 69, 118, 131, 135]. Zwitterionic molecules consist of an equal ratio of positive and negative charges in close proximity and thus preserve overall electrical neutrality, which is essential for nonfouling surfaces[49]. As discussed in Chapter 2, zwitterionic polymers have recently surpassed most hydrophilic polymers, including PEG, in resisting protein fouling. To highlight some examples, Yang *et al.* have demonstrated that carboxybetaine methacrylate (CBMA) has promising stability *in-vitro* as a hydrogel encapsulation for an implantable glucose sensor over 15 days[116]. Chen *et al.* have reported of achieving ultra-low protein adsorption (<0.3 ng/cm^2) by using polyampholytes consisting of alternating Glu/Lys or Asp/Lys[118]. Zwitterionic coatings have also been integrated into other platforms including hydrogels[136], gold[137] and silica[138] nanoparticles,

liposome[139], and gene delivery[140]. Cysteine is a promising alternative candidate for surface coating due to its small size, zwitterionic nature, and established thiol chemistry.

The use of cysteine as a coating material for bioelectronics is particularly desirable because the sulfhydryl group allows for easy and established thiol chemistry to create a self-assembled monolayer. As aforementioned, the curative electric signal of electrotherapeutic devices decays proportionally with respect to the working distance; therefore, a thinner monolayer coating will always provide better performance in a curative perspective. Recent studies have shown that cysteine as a coating material is capable of stabilizing both silicon and gold nanoparticles in protein solutions with minimal protein adsorption[117, 141]. Furthermore, cysteine functionalization onto gold nano-clusters (Au_{20}) demonstrated the enhancement in infrared activities[142]. These investigations focus mainly on nano-scale systems and the improved stability of cysteine-functionalized nanoparticles in a protein solution. On a macroscopic level, cysteine as a zwitterionic coating has also demonstrated similar promising results as shown by Li's work on grafting cysteine onto PET sheet to produce a 55% reduction in protein fouling[143]. However, these works have made no report towards the percentage of the coating that is actually in the zwitterionic state.

Results presented in this chapter demonstrate that a thin layer (~1.14 nm) of cysteine is capable of improving biocompatibility by minimizing nonspecific protein adsorption. We first compared the extent of protein fouling on cysteine-coated surfaces with gold and stainless steel surfaces using bovine serum albumin as a model protein, followed by a complete study using pool human plasma. X-ray photoelectron spectroscopy (XPS) was used to characterize the integrity of the cysteine coating as well as the percentage of the coating in the zwitterionic state. Bicinchoninic acid protein assay (BCA) confirmed that a cysteine surface demonstrated 98.5% reduction in BSA fouling and 69% reduction in blood plasma fouling when compared to a gold surface.

3.3 Material & Methods

3.3.1 Materials

L-cysteine (($HSCH_2CH(NH_2)(CO_2H)$, 97% purity) and bovine serum albumin (BSA) were used as received from Sigma-Aldrich. Stainless steel (grade 4) was obtained from the supplier and machined locally. Bicinchoninic acid (BCA) protein assay kit was used as received from Thermal Scientific. Phosphate buffered saline (PBS) was purchased from Sigma-Aldrich and Invitrogen and used as received. Pooled human serum was used as received from Innovative Research. Whole sheep blood in Alsever's solution was used a received from Cedarlane.

3.3.2 Surface Fabrication

Commercially available stainless-steel sheets were machine cut into circular disks of 2 cm in diameter and served as the substrate for all samples. Three different surfaces were fabricated for this study: stainless steel, gold, and cysteine. The gold sample was fabricated by sputter coating (Electron Microscopy Science, model MS150R-E) the stainless-steel disks through plasma evaporation of gold (99.99% purity, Electron Microscopy Science) under a vacuum of 0.05 mbar. The stainless-steel disks were exposed for 239 seconds, creating a coating thickness of approximately 10 nm confirmed by ellipsometry. The cysteine surface was fabricated by first preparing a gold substrate using the same procedure as the gold sample. Upon completion, the gold substrate was then immediately submerged into 10 mL of 1 mM cysteine solution for 12 hours. The cysteine solution was prepared by dissolving L-cysteine in phosphate buffered saline (PBS) of pH 7.4. The cysteine coated samples were rinsed with 70% ethanol, followed by a rinse with PBS solution before drying with nitrogen gas. Post-reaction rinse with ethanol was employed to remove any non-anchored cysteine and the rinse with PBS solution is to ensure that the final surface mimics that of the human physiological environment. The stainless-steel layer in the cysteine sample only exists to provide structural support as the primary substrate in this thiol

chemistry is the layer of gold. A schematic representation of the cysteine sample is illustrated by Figure 9.

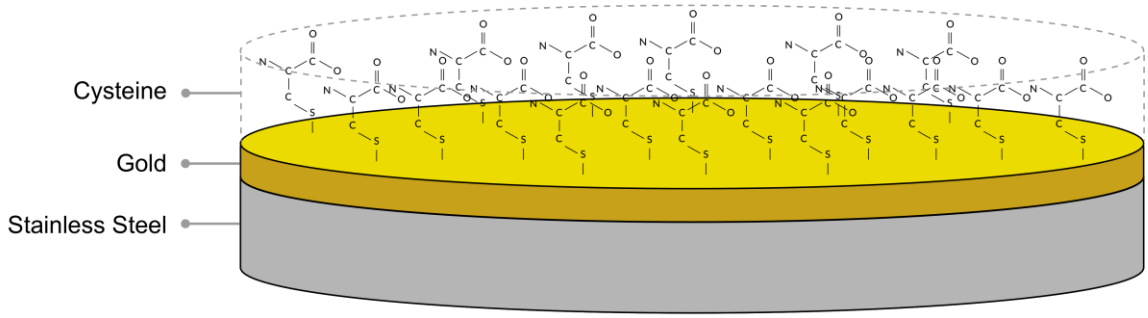

Figure 9: Schematic representation of of the cysteine-coated sample.
A layer of gold is sputter-coated onto a stainless-steel disk through plasma evaporation and, afterwards, cysteine is adsorbed onto the gold surface through thiol chemistry in solution. The stainless-steel disk only exists to provide structural support.

3.3.3 Ellipsometry Measurement

WVASE32 spectroscopic ellipsometer model M44 by J. A. Woollam Co., Inc. was used to determine the thickness of the fabricated cysteine layer. The refractive index, *n*, and extinction coefficient, *k*, was characterized using WVASE software for the stainless-steel substrate, sputter-coated gold layer, and chemisorbed cysteine coating. The optical properties of each layer had been verified individually before depositing the subsequent layer. The cysteine coating was modeled using two different methods. In the first model, the cysteine coating was defined as an individual layer using a Cauchy model whereas the second modeled the gold and cysteine as a combined layer. Both methods returned similar results.

3.3.4 XPS Characterization

Cysteine samples were characterized by X-ray photoelectron spectroscopy (XPS) analysis using an ESCALAB 250Xi (Thermo Scientific) in order to confirm cysteine integrity, binding orientation, and thickness. The X-ray gun was set to image a 500 μm^2 area at 15kV and 150W power at 80% dispersing

power. The exposure time was kept under 2 hours (104 min) in order to prevent sample damaging. The elements surveyed were gold (Au_{4f}), carbon (C_{1s}), sulfur (S_{2p}), nitrogen (N_{1s}), and oxygen (O_{1s}). The results were analyzed using the software CasaXPS.

3.3.5 SEM Characterization

The scanning electron microscopy (SEM) analysis was completed by using field emission (FE-SEM, Zeiss Leo 1550). The electron gun energy was kept at 10.00kV and the vacuum was kept approximately at $6x10^{-6}$ mbar. The samples were subjected to SEM analysis without any additional sample preparation.

3.3.6 BSA, Serum, and Plasma Exposure

0.1 mM (6.6461 g/L) of BSA solution was prepared in PBS and used as is. For BSA exposure, all samples were individually exposed to 20mL of BSA for 1 hour. Pooled human serum was used without dilution. For serum exposure, all samples were individually exposed to 10 mL of pooled human serum for 15 min. Sheep plasma was obtained by centrifuging whole sheep blood in Alsever's solution at 1200g for 15 min following the standard operating procedure[134]. For plasma exposure, all samples were individually exposed to 10 mL of undiluted sheep plasma for 15 min.

3.3.7 Protein Quantification

Bicinchoninic acid (BCA) reagent was prepared in a 50:1 ratio of Reagent A to B, termed working reagent (WR), as instructed by the kit. The resulting working reagent was diluted in PBS in a 8:1 ratio of PBS to WR, termed diluted reagent (DR). Since the procedure provided with the assay kit is intended for detecting protein concentration in solution and the protein in this study was adsorbed onto the surfaces, an adaptation of the procedure was used in order to perform solid-state detection. As a result, use of the diluted reagent (DR) was required in order for the sample readings to be comparable to the protein standard. All three surfaces (gold, stainless steel, and cysteine) were exposed to BSA for 1 hour followed

by 2 rinses with PBS. Afterward, 300 µL of diluted reagent was pipetted directly onto each sample, covering the entire surface. The samples were then incubated for 30 min in a plastic Petri dish and, afterward, 225 µL of the diluted reagent on the surface was transferred to a 96 well microplate. The absorbance reading was taken immediately at 562 nm by Epoch Microplate Spectrophotometer (BioTek). The measured absorbance was translated to BSA concentration using a set of BSA standards. The total amount of BSA protein on each surface was obtained by multiplying the translated concentration by the applied volume (300µL). The area of each sample was assumed to be consistent at 3.14 cm^2. Although cysteine, even in small quantities, has been reported to significantly influence the result of BCA assay due to its nature as a reducing agent, this concern does not apply in this study primarily because the majority of the sulfur group, which is responsible for the reducing property of cysteine, was anchored onto the gold substrate and hence, unable to influence the assay. However, it is still important to obtain a baseline absorbance of cysteine samples that may be the result of a secondary layer of cysteine molecules with exposed sulfur motifs. Therefore, before exposure to BSA solution, cysteine samples were first submerged in 20 mL of BCA reagents for 24 hours, followed by two rinses with PBS solution in order to remove unanchored cysteine. A baseline absorbance reading of cysteine samples was obtained in a similar fashion as previously described for other samples. The baseline for cysteine samples was subtracted from the post-BSA exposure absorbance in order to accurately quantify the absorbance responsible by BSA protein.

3.3.8 Surface Plasmon Resonance Imaging

SPRi sensor chips were fabricated by coating 2 cm x 2 cm glass slide substrates with a 50 nm layer of zinc oxide (ZnO) followed by a 50 nm layer of gold film on top. These chips were then further coated in different concentrations of cysteine for 30 min in order to determine the effect of coating thickness on the anti-biofouling performance of cysteine. Two different concentrations of cysteine solution that were

used in this study are 10 mM and 1 mM. The surface plasma resonance imaging (SPRi) analysis was done by the SPR Imager from GWC using a BK7 prism that was coupled under a fixed angle of 75 ° and the change in intensity was monitored over 16 minutes. The flow rate was kept constant at 60 µL/min throughout the analysis. The cysteine-coated sensor chips were exposed to a running PBS buffer for 5 minutes before introducing 10 g/L bovine serum albumin (BSA) to the system for 5 minutes followed by a wash with the running buffer. A sensor chip that has not been coated with cysteine, or a pure gold surface, represents the control in this SPRi analysis.

3.4 Results and Discussion

3.4.1 XPS Analysis

The zwitterionic nature of the coating was achieved by anchoring cysteine onto the gold layer through the sulfur head using established thiol chemistry[144], such that both the amino and carboxylate groups are available. The presence of unaltered zwitterionic cysteine layer was confirmed by XPS analysis. This investigation provides key understanding towards the chemisorption, presence of secondary layers, and percent zwitterionic state. Figure 10 illustrates the core level regions of the XPS spectra for the L-cysteine coated sample using gold as the primary substrate. The acquired gold (Au_{4f}) spectrum is illustrated in Figure 10a and was calibrated by a slight shift of -0.2 eV in order to produce the two characteristic peaks of metallic gold doublet at 84.0 eV and 87.6 eV[145]. The XPS spectra for all other elements were calibrated accordingly by the same amount of shift made upon the gold spectrum. On the gold spectrum (Figure 10a), a secondary doublet, with significantly less intensity but larger full-width half maximum (FWHM), can be observed and has the two peaks positioned at 84.12eV and 87.69 eV. The less intense secondary doublet can be assigned to metallic gold closer to the surface as reported by Dodero *et al.*[144]. Therefore, the intensity ratio of the secondary doublet with respect to the primary doublet, or I(secondary)/I(primary), provides insight on the amount of gold available on the surface for thiol

chemistry. Figure 10a shows that the secondary doublet contributes 29.88% of the signal whereas the primary contributes 70.12%. The calculated ratio of 0.4261 I(secondary) to I(primary) is significantly higher than the ratio reported for Au(111) surface at 0.12[144] and would suggest that the amount of exposed gold atoms on our fabricated surface is more than 3.55 times of the standard Au(111) surface. The result is as expected because the gold surfaces were created through sputter coating; therefore, even though the gold deposition has smoothened out the macroscopic cracks that are observed on stainless steel surfaces, on a microscopic level, the surface is rougher and contains a larger amount of exposed gold atom than that of a completely smooth 111-oriented surface reported in[144]. As illustrated in Figure 10a, the signal-to-noise ratio for gold is very high, and thus the experimental lines and the fitted spectra are almost identical and are superimposed. Such a well-defined spectrum is not always observed especially for less prominent elements such as sulfur and a low signal-to-noise ratio observed in sulfur reflects a less well-fitted spectrum.

Figure 10b illustrates the Carbon (C_{1s}) spectrum demonstrating the presence of unaltered cysteine on the sample. The deconvolution of this spectrum can be achieved by fitting four peaks centered at 284.9 (C1), 286.1 (C2), 288.4 (C3), and 289.4 (C4). The four peaks represent three chemical states of carbon. The C1 peak demonstrates characteristics of carbon involved in C-C bonding with a shift due to further bonding with sulfur and can be assigned to C_β or HS"C"H_2CH(NH_2)COOH[146-149]. The C2 peak demonstrates characteristics of C-N bonding and can be assigned to C_α or $HSCH_2$"C"H(NH_2)COOH[146-149]. The C3 and C4 peaks are in the energy region that is typical of the carboxyl group[146-149]. The decomposition of the broad structure into C3 and C4 peaks was done in accordance to that suggested by Gonella *et al.*, and can be assigned to COO^- and COOH respectively[120]. C3 and C4 peaks are often summarized by a single peak[144]; however, in order to determine the percent zwitterionic state, it is essential to decompose the broad structure into two peaks. The presence and shape of the C_{1s} spectrum

agree with the previous reporting of unaltered cysteine[120, 146-149] and concludes the success of cysteine chemisorption onto the fabricated sample.

Figure 10c illustrates the Sulfur (S_{2p}) spectrum demonstrating cysteine anchoring to the gold surface through the sulfur group and the success of the thiol chemistry. Contrary to the Au_{4f} spectrum where a high signal-to-noise ratio caused the experimental and the fitted spectra to be almost identical, the sulfur spectrum is very noisy and the fitted line describes the overall shape of the experimental line. A similar level of noise on the sulfur spectra is observed for other samples made in solution chemistry where cysteine is chemisorbed onto a gold surface[144]. Under ultrahigh vacuum deposition of cysteine onto a gold surface, Gonella *et al.* have reported a less noisy sulfur spectrum that is almost identical to the fitted spectrum in this report[120]. The experimental spectrum can be decomposed into a characteristic doublet (S1 & S2 combined) peak at 162.0 eV, which agrees with the values of 161.9±0.1eV reported for ultrahigh vacuum deposition of cysteine onto gold[120], solution chemistry of SAMs[144, 147] and alkanethiols chemisorbed on gold surfaces[145, 147]. The presence of the S3 peak is contributed by a secondary layer of cysteine as reported by Gonella *et al.*[120]. The sulfur spectrum demonstrated the success of anchoring cysteine onto the gold surface through thiol chemistry as well as the presence of secondary layer.

Figure 10d and Figure 10e illustrate Nitrogen (N_{1s}) spectrum and Oxygen (O_{1s}) spectrum respectively. The two spectra describe the presence of the zwitterionic stated of cysteine on the gold substrate. The nitrogen spectrum can be decomposed into two peaks centered at 398.4 eV (N1) and 400.2 eV (N2). These two peaks resemble the characteristic shape of NH_2 and NH_3^+ that appears in the region of 399~402 eV[120, 144, 146]. Although the values reported in this chapter for NH_2 and NH_3^+ is slightly shifted by 1eV to higher energy, the shape of the N1 and N2 peaks and spacing between the two peaks are almost identical to N_{1s} spectrum reported by Gonella *et al.*, where the surface is created by ultrahigh vacuum deposition[144]. We postulate that the shift is primarily caused by the PBS solvent used in the cysteine chemisorption and

post reaction rinse. Upon an XPS survey (not shown), the presence of sodium in trace amount (approximately 0.83 atomic %) is identified and concludes that exposure to PBS solution will leave a residue on the sample surface. The use of PBS was done intentionally as the electrolyte concentration of PBS resembles that of the human environment. By using a PBS solvent, a better representation of the zwitterionic nature of cysteine coating when operating in a physiological environment can be achieved. Identical cysteine deposition reactions were completed using DI water as opposed to PBS for both the chemisorption solvent and post-reaction rinse. The XPS spectra of these samples created with DI water (not shown) do not indicate the presence of sodium and have peak spacing and position, at 399.9eV for N1 and 401.6eV for N2, similar to that of published results[120, 144, 146]. Furthermore, the N_{1s} spectra of the samples created with DI water have almost identical shape and spacing when compared to the spectrum of samples created with PBS. Therefore, the shift in the N_{1s} spectrum of the samples created with PBS can be associated with the introduction of PBS into the system. Other potential contributions that could cause a shift in the N_{1s} spectrum are the presence of a secondary layer of cysteine and the presence of cysteine dimer. Note that more noise is observed in the N_{1s} spectrum when compared to that of carbon and gold. An analysis of the area under the curves for Figure 10c demonstrated that 90.38% of the cysteine is in the charged state (N2) whereas only 9.62% of cysteine in non-charged (N1). The oxygen spectrum, Figure 10e, exhibit a broad structure that can be assigned to oxygen atoms in COOH and COO- groups and can be decomposed into 3 peaks similar to other reports[144, 148, 149]. Since the sample was regularly exposed to oxygen during the fabrication process as well as the analysis process, the oxygen spectrum does not provide a good representation of the percent charged state of the cysteine as the nitrogen spectrum. For a complete table summarizing the peak position, full-width half maximum (FWHM), and percent area of all the chemical states for the cysteine coating refer to Supplementary Table S1.

The zwitterionic nature of fabricated cysteine coating was obtained by analyzing the intensity (I) of the N_{1s} and C_{1s} spectra. The N_{1s} spectrum provides information regarding NH_3^+ to NH_2 ratio whereas the C_{1s}

spectra provide information regarding COO^- to COOH ratio. Ideally, the fraction of charged carboxyl group can also be obtained by analyzing the O_{1s} spectrum; however, since the sample was continuously exposed to oxygen, the contribution to the oxygen spectrum is not solely based on the carboxyl group. Therefore, the charged fraction of the carboxyl group is quantified by analyzing the carbon group involved in the carboxyl moiety. The charge fraction of NH_3^+, $P_{NH3+} = I_{N2}/I_{N1+N2}$, is calculated to be at 90.38%; whereas the charge fraction of COO^-, $P_{COO-} = I_{C3}/I_{C3+C4}$, is 87.84%. In summary, 87.84% of the fabricated cysteine coating is zwitterionic, 2.54% is positively charged, and 9.62% is non-charged.

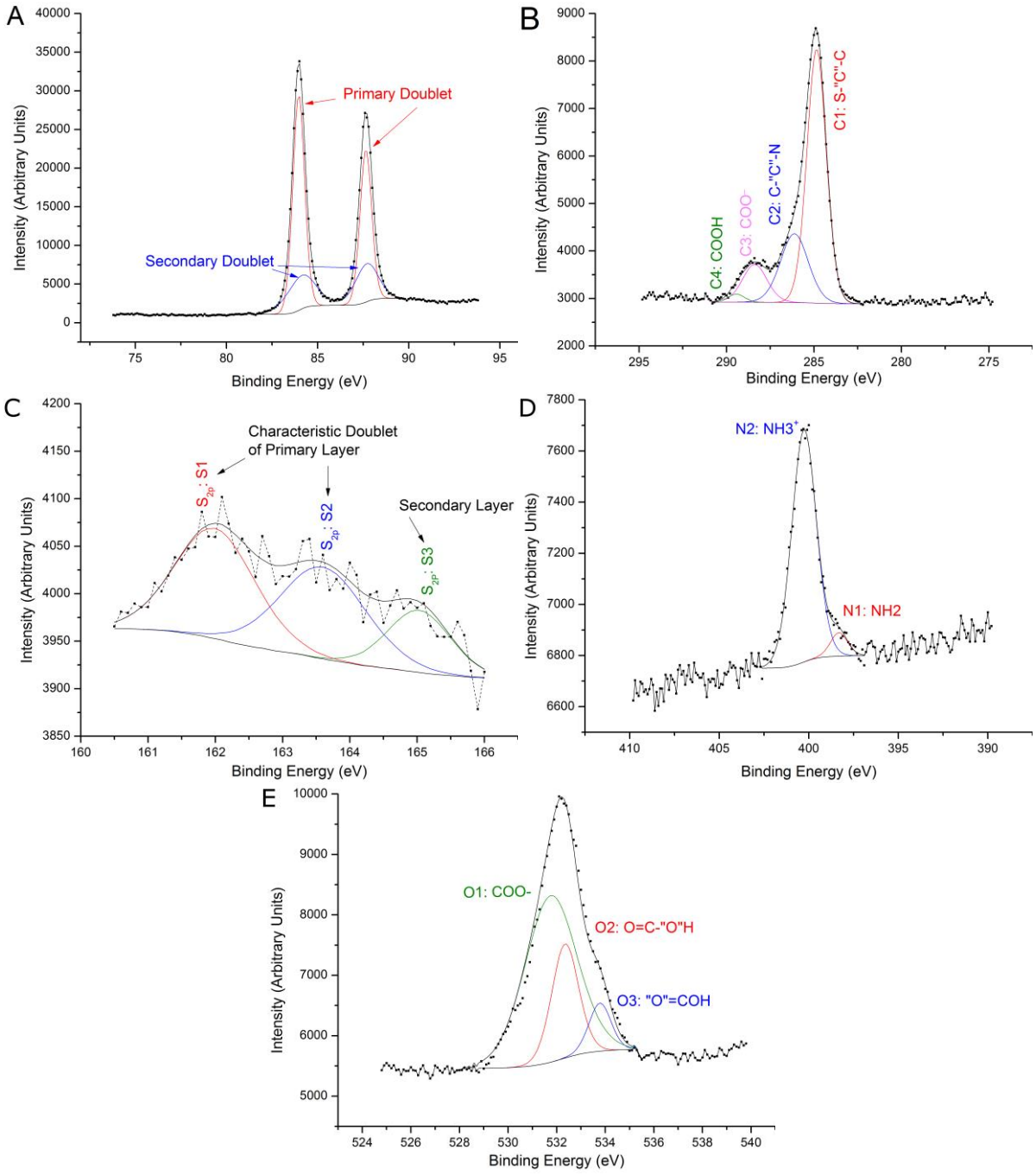

Figure 10: XPS spectra of the cysteine-coated sample.
A) Gold (Au_{4f}) spectrum illustrating characteristic doublets of metallic gold. B) Carbon (C_{1s}) spectrum illustrating unaltered cysteine. The ratio of COO^- charge group is 87.84%. C) Sulfur (S_{2p}) spectrum illustrating the secondary layer (S3 peak) and success of thiol chemistry (S1 & S2 doublet). D) Nitrogen (N_{1s}) spectrum. The ratio of the NH_3^+charge group is 90.38%. e) Oxygen (O_{1s}) spectrum. Analyzing carbon and nitrogen spectrum concludes that 87.84% of cysteine coating is zwitterionic, 2.54% is positively charged, and 9.62% is non-charged.

3.4.2 Thickness and Optical Characterization

For bioelectric therapy, the curative electrical impulse decays proportionally with respect to the working distance as governed by Coulomb's law. Therefore, in order for the proposed cysteine surface to perform as an efficient anti-biofouling coating, the thickness of the coating layer must be minimized for the success of the device. Ellipsometry was employed to determine the thickness as well as optical properties of the fabricated cysteine surface.

The thickness and optical properties of each layer were measured individually prior to the deposition of subsequent layers and are summarized in Table 4. For the stainless-steel substrate, the refractive index (n) and extinction coefficient (k) at $\lambda = 632$ nm are 2.757 and 3.792 respectively. These results match those of published sources[150]. The thickness of the stainless-steel substrate is 1/16 of an inch (0.159 cm) as given by the manufacturer and is beyond the upper limit of detection for the ellipsometer.

For the subsequent gold layer, the measured n, k, and thickness are 0.376, 3.596, and 10.40 nm respectively. The optical properties of the gold layer were different from that of published results[150, 151]; however, this observation is expected primarily because of the differences in layer roughness and thickness. The sputter-coating process produced a microscopically rough gold surface on top of an already rough stainless steel substrate as revealed by scanning electron microscopy (Chapter 3.4.4, Figure 12a & b). Therefore, the fabricated surface is a lot rougher than the smooth surfaces reported in published findings. Furthermore, the deposited gold layer is very thin (10 nm as opposed to the 200 nm reported[151]) and allows for possible optical interactions with the underlining stainless steel substrate. Both of the above properties are potential contributors to the difference in optical property of the fabricated gold layer. Herein, we demonstrated that only a very thin layer of gold (20 times less) is required to fabricate the anti-biofouling coating.

The expected thickness of the cysteine layer is approximately 10 Å, which approaches the detection limit of the ellipsometer. Therefore, instead of defining the cysteine surface as an individual layer in the software's model, the surface was defined as part of a combined layer of both gold and cysteine as inspired by Tengvall *et al.*[151]. The resulting n, k, and thickness of the combined layer are 0.286, 3.463 and 11.54 nm. The change of n and k with respect to incident wavelength is presented in Figure 11. The thickness of the cysteine layer by itself can be calculated by subtracting the previously determined thickness of the gold layer from the thickness of the combined layer, which yields a thickness of 1.14 nm.

Table 4: Thickness and Optical Characterization

	n	k	Thickness
Stainless Steel	2.757	3.792	1/16 inch*
Gold	0.376 ±0.005	3.596 ±0.057	10.404 ±0.080nm
Gold + Cysteine	0.286 ±0.024	3.463 ±0.017	11.541 ±0.150nm

*thickness beyond upper limit of ellipsometry and is given by manufacturer

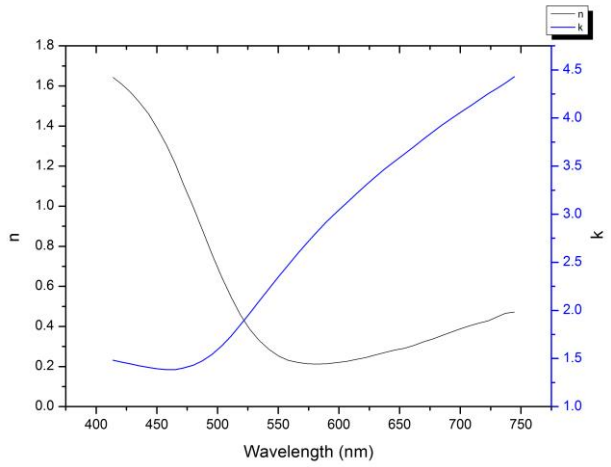

Figure 11: Ellipsometry Reading
Graph of refractive index (n) and extinction coefficient (k) with respect to incident wavelength produced by ellipsometry modeling cysteine and gold as a combined layer.

3.4.3 Protein Fouling

Following surgical insertion of implantable bioelectronics, exposure of device surfaces to nonspecific adsorption of plasma and tissue fluid protein is unavoidable and triggers a cascade of inflammatory and

wound healing responses that are typical of a foreign body response. By minimizing the amount of nonspecific protein adsorption, the degree of undesirable host response can be controlled, thus prolonging the in-vivo functionality of the device. Bovine serum albumin (BSA) was selected as the model protein for the assessment of nonspecific fouling primarily because there have been many published results of different nonfouling coatings using BSA as a model protein (PEG[8], PMMA[77], Poly(TM-SA)[69]); therefore, BSA serves as a typical benchmark that allows for easy comparison. In addition, BSA closely resembles human serum albumin (HSA), which is the most abundant plasma protein in the human blood. Furthermore, the properties and behaviors of BSA, such as a negative charge under physiological pH, is well understood and characterized[152-154], which provides the benefit of confirmation characterization in future studies.

The amount of BSA that is adsorbed onto gold, stainless-steel, and cysteine-coated surfaces is quantified by Bicinchoninic acid (BCA) protein assay. The assay is able to quantify protein by detecting the amount of Cu^{2+} that had been reduced to Cu^{+}. Under normal circumstances, the assay is not compatible with cysteine because the molecule is a reducing agent. However, in this study, cysteine was used as a coating material and was anchored onto a gold surface through thiol chemistry; therefore, the majority of the sulfur motif, which is responsible for the oxidation property of cysteine, was anchored onto the gold substrate and no longer available. To account for the remaining exposed sulfur motif, perhaps due to cysteine dimers or secondary layer of cysteine molecules, a baseline absorbance reading for cysteine samples was obtained and subtracted from the post-BSA exposure reading.

The results of the BCA assay on all three surfaces are tabulated in Table 5. The concentration of BSA was obtained by fitting the absorbance value to a set of protein standards. The baseline absorbance for cysteine sample is 0.075 ± 4.8% and was subtracted from the post exposure absorbance of 0.099 ± 5%. The total amount of BSA on each surface was obtained by multiplying the BSA concentration by the

applied volume of BCA, which is 300 µL. The surface area of each sample is the area of a circle represented by $\pi(1cm)^2$ and is assumed consistent between samples. The amount of BSA fouling onto cysteine, stainless-steel, and gold surfaces is 3.92 $\mu g/cm^2$, 61.48 $\mu g/cm^{2,}$ and 261.79 $\mu g/cm^2$ respectively. The cysteine-coated surface has successfully demonstrated a 93.62% reduction compared to stainless steel and 98.50% reduction compared to gold.

The work presented herein differs from the published ultra-low fouling surfaces in two fundamental aspects: coating thickness and experiment conditions. The objective of our study was to design a zwitterionic coating while minimizing interferences with the underlying bioelectronic. Following this design criteria, cysteine was selected as the ideal candidate because we believe cysteine coating provided the least increase in surface thickness. Long-chain polymer brushes, such as those used to achieve fouling in ng/cm^2 range, are known to improve resistance to protein fouling because of the steric repulsion that occurs when the long polymer chains are compressed due to the adsorption of proteins[12, 13]. However, for applications in bioelectric therapy, a thick polymer brush coating would be detrimental to the device performance, because the curative electrical impulse decays proportionally with respect to the working distance as governed by Coulomb's law. Therefore, our work aimed to create a monolayer of surface coating (1.14 nm) as opposed to the polymer brushes (10-15 nm[126]) found in ultra-low fouling surfaces. Since the effective electric field is inversely proportional to the distance, having a thinner surface will allow a cysteine-coated device to exhibit a stimulation that is 10 to 15 times stronger than a surface coated with polymer brush. In addition, the experimental conditions, mainly the protein concentration and exposure time, varies between different groups. Surfaces reported having ultra-low fouling capability are generally exposed at 1 g/L of protein for 10-15 min[63, 69, 118] whereas, our work was conducted with a concentration of 6.6 g/L and an exposure time of 60 min. A higher protein concentration and a longer exposure time are expected to result in a greater degree of surface fouling. Comparing to a recently

published result using cysteine as a coating, our design outperforms that of the published by 17 times (66 μg/cm^2) [143]. These findings are comparable with recently published nonfouling hydrogel[155], zwitterionic coatings[156, 157] and PEG-based polymer brush[83].

Table 5: Quantification of BSA fouling by BCA assay

	Abs.	Con. (μg/mL)	Total BSA (μg)	Fouling (μg/cm^2)
Gold	1.601	2741.44	822.43	261.79 ± 6.39 (N=3)
Stainless Steel	0.376	643.84	193.15	61.48 ± 2.31 (N=3)
Cysteine	0.024	41.10	12.33	3.92 ± 0.19 (N=5)

A baseline absorbance reading was subtracted for the cysteine sample.

3.4.4 SEM Analysis

The purpose of the SEM analysis is to complement the BCA protein assay by qualitatively assessing and verifying the performance of cysteine coating in reducing nonspecific protein adsorption. The performance of the cysteine coating was compared to stainless steel and gold surfaces. Figure 12a illustrates the BSA cluster on stainless steel surface demonstrating the characteristic spherical clusters similar to the published SEM[158-160] and AFM images[161]. Figure 12d illustrates the SEM image of stainless steel (SS) subsequent to BSA exposure. Although the stainless-steel disks appear well polished on a macroscopic level, SEM images returned cracks with rough grain-like structures that are capable of trapping BSA clusters (Figure 12a). These cracks were observed in SEM images (not shown) of stainless steel sample prior to BSA exposure. The unexposed stainless steel disks were sputter coated with gold to create a gold substrate for cysteine deposition (Figure 12b). Figure 12b and 12c illustrates, respectively, gold and cysteine-coated surfaces prior to BSA exposure. The recurring cracks observed in stainless steel samples disappeared once the sample was sputter coated with gold, as demonstrated by Figure 12b, leaving a continuous surface without cracks. As a result, cysteine-coated surfaces are also free from cracks since they are fabricated using the gold-coated surface as a substrate. It is important to note that, in both Figure 12b and 12c, there are debris or clumps present. We postulate that these debris are most

likely artifacts from the gold sputter coating process primarily because, during the coating process, not all of the gold are discharged as plasma and a percentage of gold could be deposited in chunks.

The SEM images of the post-BSA exposure stainless steel surface, the gold surface, and the cysteine-coated surface are presented as Figure 12d-f respectively. These series of SEM images provide a qualitative assessment of the degree of BSA adsorption onto each surface. Comparing these three images, BSA adsorption is clearly most prominent on the gold surface (Figure 12e) as large and localized cluster of BSA deposits can be found throughout the gold surface and small spheres of BSA are observed in between. These large clusters of BSA are not present on stainless steel and cysteine surfaces, where only small spherical BSA proteins are observed. The adsorption of BSA onto the stainless-steel surface (Figure 12d) is distributed more evenly when compared to the gold surface and only sparse amount of BSA is sparkled throughout the stainless-steel.

Figure 12f illustrates the amount of BSA adsorbed onto a zwitterionic surface. There were significantly fewer BSA clusters found on the cysteine surface and the contrast of this image was slightly adjusted to make the visual analysis less challenging. In order to qualitatively conclude that the cysteine coating exhibits a better performance, the post-exposure image of the cysteine surface was taken at almost double the imaging area compared to gold and stainless steel and presented as Supplementary Figure S1. Even at this increased imaging area, the SEM image for cysteine-coated simple demonstrated significantly less amount of BSA adsorption when compared to the images of stainless steel and gold surfaces. These qualitative assessments complement the quantitative results of BCA assay.

Magnified images of the cysteine-coated samples, illustrated as Figure 13, revealed an underlying layer of periodic wave-like nanostructures approximately 10 nm in width. This image suggests the presence of a secondary layer of cysteine which agrees with the results from XPS analysis (Figure 10e). The

underlying wave-like structure is of interest primarily because rough nanostructures have previously been shown to improve nonfouling behaviors[162-164].

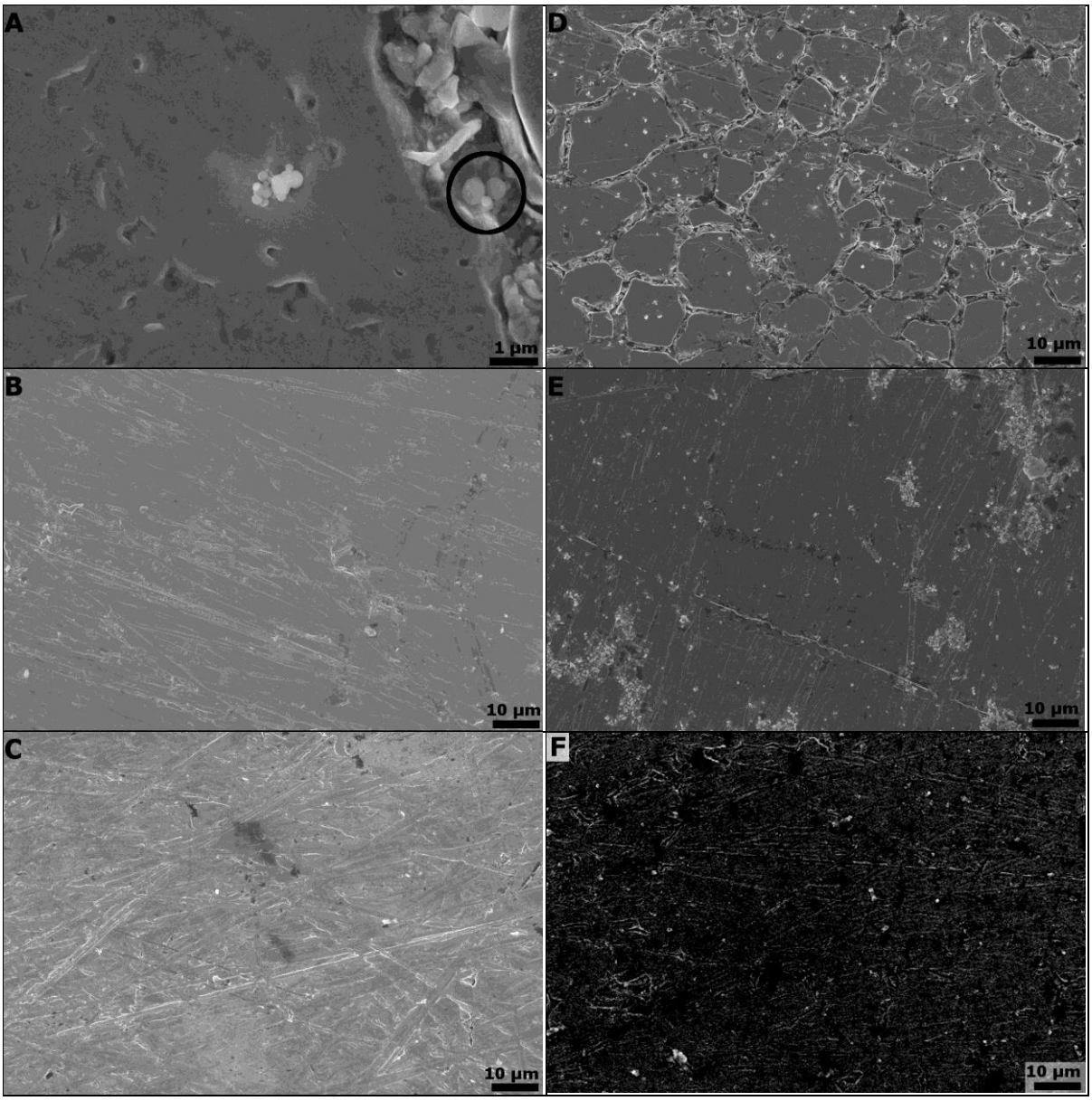

Figure 12: BSA Fouling

A) Stainless-steel surface subsequent to BSA exposure. Note the BSA clusters found in cracks. B) & C) are unexposed gold and cysteine surfaces, respectively. Cracks observed in stainless steel surfaces have been covered by gold sputtering. D), E) & F) are stainless steel, gold, and cysteine surfaces, respectively, subsequent to BSA exposure. The visual assessment qualitatively concludes that BSA fouling is most prominent on the gold surface, then stainless-steel, followed by cysteine surface. The magnifications are 10,010X for A, 965X for B, C, D, E, and F. Supplementary Figure S1 presents a zoomed-out SEM image of Figure F at 572X magnification. This image displays an area of the cysteine surface that is almost twice as large as that of the gold and stainless steel in this figure, but still demonstrated less BSA fouling.

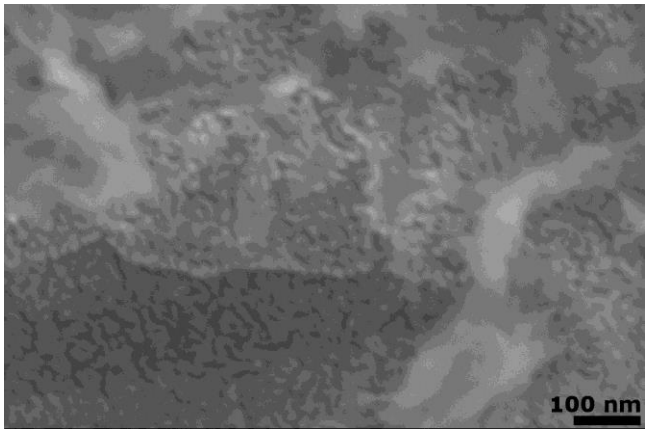

Figure 13: SEM images of cysteine samples
This image demonstrates an underlying layer of wave-like nanostructures and secondary layer that agree with XPS results. The magnification for this image is 118,190X.

3.4.5 Serum and Plasma Exposure

Bovine serum albumin (BSA) was used for the protein fouling study primarily because of the necessity for easy comparison with other published results, as well as its close resemblance to human serum albumin (HSA). In order to obtain a better understanding towards the performance of cysteine-coated surfaces inside a host, this study investigates the anti-biofouling properties of zwitterionic cysteine when exposed to a complex environment composed of a full range of plasma proteins. Gold and cysteine surfaces were exposed to undiluted human serum (HS) and incubated at 37°C for 15 min. A reduced fouling of plasma proteins, as well as electrolytes, was observed for the cysteine surface.

The amount of serum protein fouling was quantified by BCA protein assay using the same method described in the previous section. Similar to the study done with BSA, cysteine-coated surface demonstrated a significant improvement in regards to the amount of plasma protein adhesion than the gold. The absorbance reading for the cysteine surface was measured by BCA protein assay to be at 0.494, which is 68.95% less than the reading for the gold surface.

SEM images (Figure 14) demonstrated a reduced fouling of electrolytes on the cysteine-coated surface compared to the gold surface. On both surfaces, long dendritic electrolyte crystals were observed that are similar to reported dendritic salt patterns such as silver nano-dendrites[165], sodium chloride crystals[166], dendritic gold[167], and dendritic copper[168]. The dendritic patterns observed on both surfaces are formed when the electrolytes present in human serum undergoes anisotropic crystal growth based on the diffusion-limited aggregation (DLA) effect[165, 169, 170].

The observed dendritic crystals are significantly more prominent on the gold surface compared to the cysteine-coated surface as illustrated by comparing Figure 14a to Figure 14b. The direction and the shape of the deposits are consistent throughout the gold surface. The deposits on the cysteine surface have a tendency to branch outwards from a central nucleation point indicated by red arrow in Figure 14a. In order to compare the performance of the two surfaces, SEM images of both gold and cysteine-coated surfaces are taken under different magnifications while demonstrating a similar degree of fouling. The comparison is presented as 14b to 14c and based on the difference in magnification of the two images; a qualitative assessment would suggest that the cysteine surface can reduce the amount of electrolyte fouling by more than 50%.

The reduced electrolyte fouling on the cysteine-coated surface is likely a result of the zwitterionic nature of the surface. Zwitterionic surfaces are known for the formation of a hydration layer, which is a layer of water molecule tightly bounded by ionic solvation[164]. Given that the size of the water molecules is many times smaller than the radii of electrolytes such as potassium and sodium, the hydration layer acts not only as an energetic barrier but also as a physical barrier that the electrolytes have to overcome in order to adsorb onto the surface[87, 164]. This phenomenon is best illustrated by observing the pattern of crystal growth on both surfaces. For the cysteine surface, the dendritic pattern expands from a central nucleation point (Figure 14a & c), whereas for the gold surface the crystal growth appears to be random

(Figure 14b), and hence, suggesting the presence of many more nucleation points. The salt pattern around an area of the cysteine surface that is speculated to contain more surface defects is presented in Supplementary Figure S2. The presence of the hydration layer on the zwitterionic surface renders it more difficult for the electrolytes to adhere and create initial nucleation points for crystal growth. As a result, less electrolyte fouling was observed on the cysteine surface.

It is meaningful to investigate the performance of the cysteine coating when exposed to biomolecules involved in the clotting cascade. Using the same procedure as the HS exposure, cysteine and gold surfaces were individually exposed to sheep plasma, which contains fibrinogen and other clotting factors in addition to serum proteins. The absorbance reading for the cysteine surface was measured by BCA protein assay and demonstrated a 67.49% reduction in fouling compared to the gold surface. This result concludes that the cysteine surface is capable of functioning as an anti-fouling surface even in the presence of fibrinogen and other clotting factors.

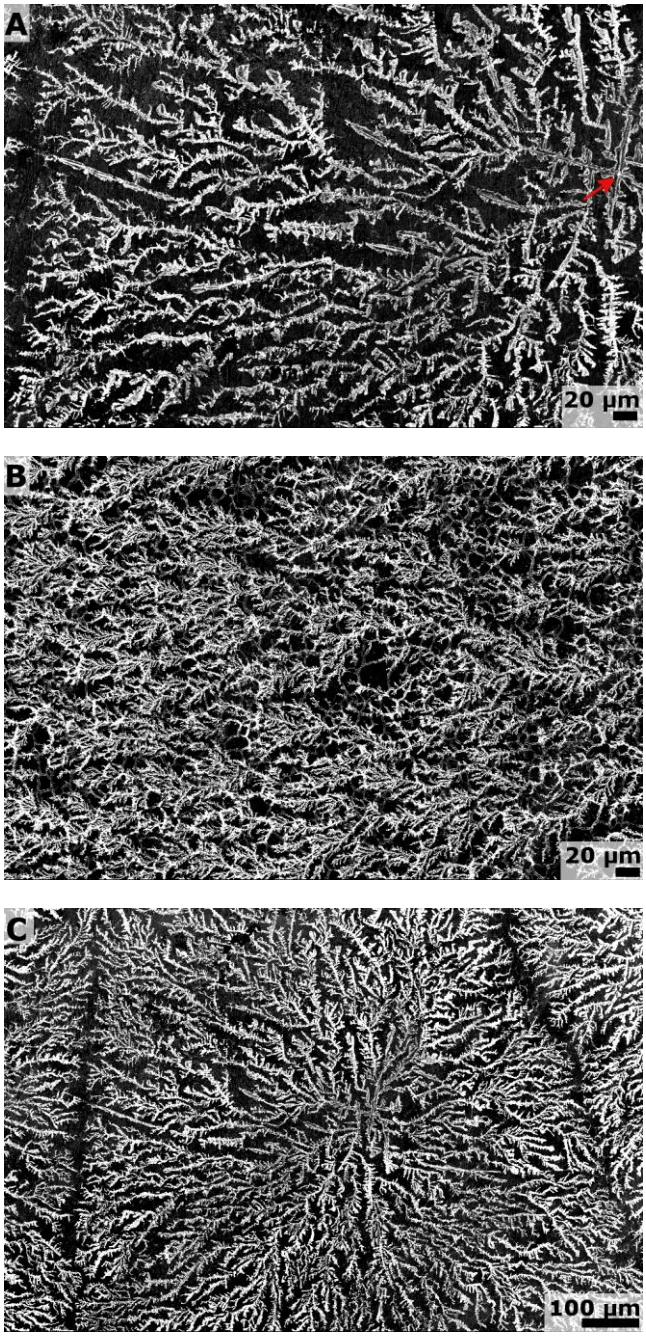

Figure 14: SEM images of dendritic electrolyte pattern subsequent to serum exposure.
Cysteine surface: 5a, and 5c. Gold surface: 5b. Note that the electrolyte deposit for cysteine surface appears to grow outwards from a central nucleation as indicated by the red arrow in 5b. The magnification is 203X for A and B, and 100X for C. Image B and C are taken under different magnifications, but demonstrated a similar degree of fouling. Based on the difference in magnification, the cysteine surface exhibits more than 50% less fouling than the gold surface.

3.4.6 SPRi Analysis

The effect of coating thickness on the anti-biofouling performance of cysteine was determined by SPRi analysis. In this study, SPRi gold sensor chips were coated in different concentrations of cysteine solution in order to produce cysteine coatings of different thicknesses. The unaltered gold surface of the sensor chip was used as the control. Figure 15 compares the protein adsorption levels on a pure gold surface with those on cysteine surfaces coated in 1 mM and 10 mM solutions. All samples were first exposed to a running PBS buffer (region I) before introducing 10g/L BSA to the system (region II) followed by the running buffer again (region III). The SPRi result presented in Figure 15 are calibrated by eliminating extreme values caused by experimental defects. The signal difference between the buffer baseline (region I) and the post-exposure washing (region III) provides a quantitative assessment of the level of nonspecific protein adsorption. The spikes observed in region 2 for both of the cysteine-coated samples are experimental defects caused by small air bubbles introduced during the analysis.

The cysteine-coated surfaces demonstrated a significant reduction in BSA fouling, which supports the results from the BCA assay. Although the amount of reduction in BSA fouling observed in the SPRi analysis may appear to be less than that observed in the BCA assay, it is important to note that the samples analyzed by BCA assay was exposed to proteins for 60 minutes, which was almost 11 times longer than the exposure time of 5.5 minutes during the SPRi analysis. A continuous increase in the signal during BSA exposure (region 2) for the gold surface also suggests that the gold surface is not saturated with BSA and further exposure will increase the amount of fouling onto the gold surface. This continuous increase is not observed for both of the cysteine-coated samples, indicating that the amount of BSA fouling onto cysteine surfaces will not increase significantly when further exposed to the protein solution.

Although both cysteine-coated surfaces demonstrated a significant reduction in BSA fouling when compared to the control, the surface coated in 1 mM of cysteine solution exhibits a better performance

than the surface coated with 10 mM cysteine solution. This observation can be explained by attributing a reduced percentage of zwitterionic state to a thicker coating. A surface fabricated under a lower concentration of cysteine solution will produce a thinner layer of coating, and as the coating thickness decreases (approaching a monolayer), the percentage of cysteine in the zwitterionic state will increase[120]. As a result, a thicker coating will contain a lower percentage of cysteine in the zwitterionic state and hence, a poorer performance in resisting protein because the zwitterionic property of cysteine is responsible for the anti-biofouling behavior.

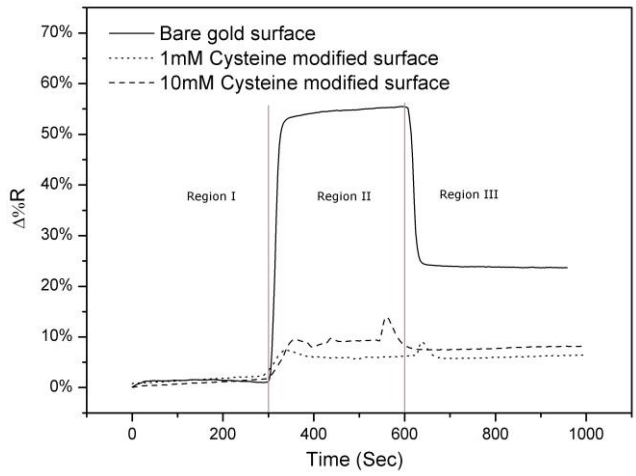

Figure 15: SPRI Results
Bare gold surface (solid line). Cysteine surface coated in 1mM solution (dotted line), and Cysteine surface coated in 10mM (dashed line). Region 1 represents the baseline sensor response for the PBS buffer only. BSA was introduced in Region 2, and a wash using PBS was done in region 3.

3.5 Conclusion

A zwitterionic cysteine surface was successfully fabricated through solution thiol chemistry on a gold-coated stainless steel substrate. X-ray photoelectron spectroscopy returned results of unaltered cysteine anchored to the gold substrate through the sulfur group. Secondary layers of cysteine are confirmed both through XPS and SEM as expected from solution chemistry. From the assessment of the nitrogen (N_{1s})

and carbon (C_{1s}) spectra, it can be concluded that 87.84% of the fabricated cysteine surface is zwitterionic, 2.54% is positively charged, and 9.62% is non-charged. BCA protein assay demonstrated that cysteine surface exhibits a BSA fouling of 3.92 μg/cm^2, which is 93.62% and 98.50% lower than stainless steel and gold surfaces respectively. SPRi analysis returned similar results and suggest that a thinner cysteine coating will enhance performance. Serum fouling on cysteine surface is 68.95% less than that of gold. SEM analyses were performed to complement the findings of BCA protein assay and the results from the two characterization techniques are in agreement. The results reported in this study demonstrated that cysteine is a promising candidate for zwitterionic anti-biofouling coating and has the potential of serving as a PEG-alternative for long-term implantable bioelectronics due to its thin coating thickness, zwitterionic nature, and stability in-vivo.

Chapter 4
Antifouling Mechanisms of Zwitterions

4.1 Summary

After the successful demonstration of the antifouling property of cysteine in chapter 3, this chapter focuses on exploring the antifouling mechanisms behind both hydrophilic and zwitterionic materials. It is widely accepted that surface hydrophilization is the primary method for creating antifouling surfaces. However, arguments based solely on surface hydrophilicity are quickly overthrown. Silica, for example, is super hydrophilic, but is also highly prone to protein fouling. Thus, even though surface hydration is a key property to consider for designing an antifouling surface, there are still multiple mechanisms that must also be considered. This chapter focuses on zwitterionic materials and how their antifouling mechanisms suppress those employed by the traditional hydrophilic material. Topics discussed include the degree of hydration, the structure of surrounding water, the residence time of associated water molecules, the effect of ion-coupling, and benefits of steric repulsion. Following the successful proof-of-concept presented in Chapter 3, molecular dynamics simulation of zwitterionic cysteine was performed using Gromacs to investigate the antifouling properties of the cysteine on a molecular level and compared with other zwitterionic antifouling materials currently available.

4.2 Introduction

Recent inventions of new bioelectronics and biomaterials have stipulated an increasing demand for novel materials to prolong the functionality of medical implants[171], biosensors[2], and marine membranes[172]. In the field of membrane separation technology, protein fouling initiates multiple degradation pathways and promotes subsequent biological adsorption that decreases membrane

permeability, selectively, and ultimately longevity[173]. For bioelectronic implants, nonspecific protein adsorption initiates a cascade of foreign body response (FBR) that causes a gradual loss of device functionality and ultimately results in implant isolation by fibrous encapsulation which renders the device non-functional[29, 30]. Existing implant materials such as polyurethane, siloxane polymers, and titanium are considered medical grade not because these materials significantly resist protein adsorption[60, 174], but simply because the amount of fouling is tolerable for the location, function, and duration for which the devices are used for. With the recent introduction of more advanced membranes and sensitive implantable sensors that have a significantly lower tolerance for biological absorbents[5, 6, 31, 133], now, more than ever, has there been a demand for novel strategies to resist surface fouling.

It is commonly accepted that reducing the interfacial energy of device surface with water, or hydrophilization, is an effective strategy to resist nonspecific fouling[50, 55, 175]. By modifying the surface to contain extensive water in a similar state to the bulk water, the adsorption process is not favorable as replacing a protein/water interface with a protein/surface interface will not gain any free energy[176]. Ethylene glycol (EG) and its derivatives are perhaps the most representative and well-studied hydrophilic antifouling material[7]. By forming a strong hydration shell, EG coated surfaces demonstrated a decreased interaction with the biological environment[8-11]. Polymerization of ethylene glycol to create a dense layer of PEG brushes further improves the material's resistivity to protein adsorption through steric repulsion, which describes the entropically unfavorable compression of the polymer chain due to foulants[7, 12, 13]. However, in-vitro studies of PEG-based material have reported short-term stability that is hypothesized to be caused by oxidation stresses in biological environment[72, 73]. As a result, recent research focuses have shifted towards finding PEG alternatives that are more biocompatible and biostable.

Mimicking the abundant zwitterions on the headgroups of phospholipids that constitute the external mammalian cell membranes[17], zwitterionic surfaces have demonstrated a strong resistance against

biofouling since the 1970s (mainly phosphatidylcholine or PC[18]) and had undergone many iterations in the past decade[7]. Zwitterions, which form a stronger hydration layer through ionic solvation compared to hydrogen bonding[19], often outperform traditional hydrophilic polymers in resisting biofouling and are recognized as the next-generation antifouling material. Integration of zwitterionic monomers (methacryloyloxylethyl PC) into bulk polymer material (hydroxyethyl methacrylate) to improve biocompatibility and reduce fouling have since been ubiquitous (omafilcon A, a commercially available contact lens material[20]). More often, zwitterions are deposited on a surface as an antifouling coating, as oppose to integration into the bulk material, through various graft-to[177] and graft-from[67, 178] techniques. As outlined in Chapter 2, recent advances in zwitterionic self-assembled monolayers (SAMs) by Whitesides[134] and Jiang's[179] group offers several promising materials such as sulfobetaine (SB)[180, 181] and carboxybetaine (CB)[182] to choose from when designing an antifouling coating. Zwitterionic cysteine has also demonstrated promising antifouling properties on gold surfaces[174] and silica nanoparticles[117]. Although much experimental work has been done to demonstrate the capability of zwitterionic material in resisting biofouling, less has been done on investigating the fundamental mechanism behind the antifouling preparties of zwitterions, especially from a molecular simulations perspective.

This chapter complements chapter two by providing a focused discussion on the fundamental mechanisms behind antifouling materials from a molecular simulation perspective and provides a comparison with the similar experimental works when appropriate. Following the successful proof-of-concept presented in Chapter 3, molecular dynamics simulation of zwitterionic cysteine was performed using Gromacs at room temperature and body temperature in order to investigate the antifouling properties of the cysteine on a molecular level. It is important to note that although several zwitterionic monomers have demonstrated excellent antifouling properties in simulations, the complicated synthesis of monomers in experimental work limits their application (e.g. MPC)[183].

4.3 Antifouling Mechanism

4.3.1 Surface Hydration

The antifouling mechanism is traditionally attributed to the presence of a hydration layer on the surface. Simulations done by Zheng *et al.*[51] demonstrated that a layer of bonded water molecules adjacent to hydrogen-bonding acceptors on various SAMs is responsible for repelling lysozyme and that oligo(ethylene glycol), having the largest number of bonded water molecules out of the three simulated SAMs, exhibited the highest repulsive force. Experimental results also agree with these simulation findings and indicated that an increase in hydrophilicity reduces protein fouling. For example, Warkentin demonstrated that reducing the hydrophilicity of silica by grafting hydrophobic methyl groups resulted in an increased BSA fouling[175]. Similarly, Tsai *et al.*[60] has demonstrated that by modifying the hydrophobic polyurethane with the more hydrophilic dextran, the amount of protein adsorbed is reduced to less than half for numerous plasma proteins including serum albumin, fibrinogen, and haptoglobin Hp2. When designing an antifouling surface using polymer brush, surprisingly, a highly dense polymer coating does not always perform as well as its less dense equivalent. For example, an experimental study of OEG-SAMs between 60-80% packing density actually demonstrated better resistance to fibrinogen fouling compared to those with packing density 80% and above[96]. This observation can be explained by considering the degree of hydration associated with the different packing density. In a set of simulations[52], OEG SAMs at both high and low packing densities exhibited a lower number of bonded water molecules due to reduced water permeation and reduced hydrogen-bonding acceptors, respectively. However, OEG SAMs fabricated between 50-80% surface packing density demonstrated a noticeably higher number of bonded water molecules. Therefore, there appears to be a strong correlation between the number of hydrogen-bonded water molecules and OEG-SAMs' ability to resist protein fouling. This correlation leads to the widely-accepted guideline that materials capable of forming a larger amount of hydrogen-

bonds with the surrounding water molecules exhibit better antifouling property. Simulations by He *et al.*[184, 185] on this topic are particularly informative.

When comparing surface hydration for the purpose of reducing fouling, it is beneficial to quantify the amount and mobility of water molecules inside a moiety's hydration shell. Herein, the term hydration shell refers to the area surrounding a specific moiety where water molecules exhibit a different ordering from the bulk water, and the term hydration layer refers to the layer of water molecules associated with the surface, including those integrated into the polymer brush. In simulations[185-187], the radius of the hydration shell is often defined by the first minimum position of the radial distribution function (RDF) generated from the oxygen atom of water (O_w) and the charged moiety. Following the guideline that an increase in hydrophilicity will result in a reduction of protein adsorption, it is expected that an increase of water molecules in the hydration shell will also improve a material's antifouling property. The mobility of associated water molecules is assessed by quantifying the length of time that water molecules spend inside the hydration shell (also referred to as residence time). A longer residence time means a longer duration of which water molecules spend near a moiety and a lower mobility of associated water. Figure 16 conceptualizes the method for calculating residence time. When assessing residence time, simulations[185-187] only follow the water molecules that originally existed inside the hydration shell. Thus, residence time is defined as the total length of time that the original water molecules spent inside the hydration shell. This value is calculated by recording the fraction of original water molecules that remained inside the hydration shell throughout the simulation and integrating this fraction with respect to the simulation time. Table 6 and Table 7 summarize simulation findings of the amount and residence time of water molecules for zwitterionic materials and hydrogen bonding for hydrophilic material.

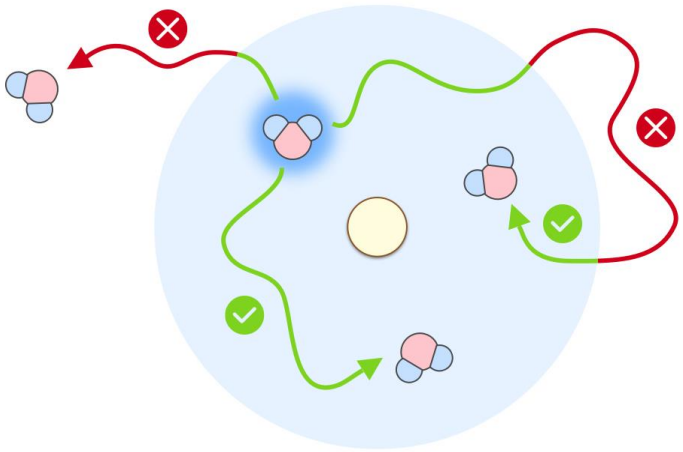

Figure 16: Illustration of residence time
Residence time provides a means to quantify the mobility of water molecules associated with a specific moiety. Simulations track water molecules that are originally inside the hydration shell and quantify the total duration that these molecules spend inside the shell. If a water molecule leaves the hydration shell but returns at a later time, the duration of which it spent outside the hydration shell is disregarded.

Table 6: Summary of MD Results for Hydration of Zwitterionic Material

This table summarizes simulation results regarding the water molecules associated with various zwitterions. Starting with a center methylene group, the row and column headings refer to the negatively and positively charged end groups of a zwitterion. For example, the cell between NH_3 and CO_2 refers to the molecule NH_3-CH_2-COO. The blue values in the cell refer to the properties of anionic group whereas the red values refer to the properties of the cationic group. The values in the first row of a cell refer to the number of associated water molecules, the values in the second refer to the residence time, and the last value refers to the hydration free energy. $CO_2CH_2(CH_2)N(CH_3)_3$ refers to carboxybetaine (CB), and $SO_3CH_2(CH_2)N(CH_3)_3$ refers to Sulfobetaine (SB). [186, 187]

	NH_3		$N(CH_3)$		$N(CH3)_2$		$N(CH3)_3$		$(CH_2)N(CH3)_3$	
CO_2	4.99	3.37	5.00	11.75	5.08	15.38	5.18	17.12	5.94	18.54
	15.44ps	8.63ps	15.88ps	19.16ps	17.44ps	23.95ps	21.33ps	29.16ps	35.72ps	25.77ps
	-216 kJ/mol		-230 kJ/mol		-224 kJ/mol		-261 kJ/mol		-404 kJ/mol	
SO_3	6.42	3.62	6.50	12.75	6.40	15.38	5.92	16.75	7.08	18.64
	15.55ps	10.6ps	16.61ps	20.00ps	16.72ps	24.16ps	15.61ps	25.00ps	25.43ps	23.08ps
	-240 kJ/mol		-249 kJ/mol		-259 kJ/mol		-251 kJ/mol		-519 kJ/mol	
OSO_3	6.34	3.87	6.38	12.75	6.24	15.62	5.84	16.87	Legend	
	14.94ps	11.06ps	15.5ps	18.12ps	16.05ps	24.37ps	12.77ps	24.37ps	N_{aionic}	$N_{cationic}$
									t_{aionic}	$t_{cationic}$
	-296 kJ/mol		-290 kJ/mol		-303 kJ/mol		-238 kJ/mol		Hydration Free Energy	

Table 7: Number of Hydrogen Bonds

For hydrophilic polymers acquired through MD simulations.[52, 188]

	$(EG)_4$	HYDROXYL MANNITOL	HYDROXYL SORBITOL	METHYL MANNITOL	METHYL SORBITOL
NUMBER OF H-BONDS	1.31	2.47	2.36	2.17	2.25

4.3.2 Effect of Water Structure and Distance Between Zwitterion Charges

When discussing mechanisms affecting the antifouling performance of zwitterions on a molecular level, the structure of water molecules associated with the charged moiety is a topic of much contradiction. Traditional hydrophilic polymers, such as PEG, are known to form a network of hydrogen bonds with the surrounding water molecules[52] and disrupting this network comes with a high energy cost[189]. This

energy barrier is speculated to be the dominating force behind the antifouling property of hydrophilic polymers[52]. Zwitterionic materials, on the other hand, have been reported to associate with surrounding water molecules through ionic solvation in various simulations[184, 185]. This ion-dipole interaction is stronger than hydrogen-bonding as reflected by a lower mobility of associated water molecules[185-187]. The superior performance of zwitterions in resisting fouling is often credited to this stronger energy barrier created by the oppositely charged moieties[58].

However, increasing the number of associated water molecules and forming a highly-structured water network around the charged group will also reduce entropy. Another school of thought believes that perturbing the surrounding water molecules is actually unfavorable for resisting protein fouling. The argument is that if the hydration layer formed by the surface is in a similar state as bulk water, then the adsorption process is not favorable because replacing a protein/water interface with a protein/surface interface will not gain any free energy. Experimental studies by Kitano *et al.* using Raman and FTIR spectroscopy on zwitterionic polyelectrolytes demonstrated that zwitterions do not perturb the hydrogen bonding of the surrounding water structure, including those associated[19, 190, 191]. Following this argument, it is desirable to ensure that the structure of associated water remains unperturbed compared to bulk water in order to promote antifouling performance. It is speculated that zwitterions, having two oppositely charged groups in close proximity, supports the polarity of water between the charged groups. Figure 17 illustrates the two lines of arguments presented above.

It is important to note that the antifouling mechanisms discussed up to this point do not only apply to monomers that are zwitterions; these mechanisms also apply to amphoteric polymers composed of alternating monomers of opposite charges. However, the distance between these opposite charges plays an important role in dictating a material's antifouling performance. A set of molecular simulations was done by Shao *et al.*[192] to investigate the effect of distance between opposite charges within a zwitterion.

The charge distribution, hydration, and ionic interactions were computed for a carboxybetaine (CB) monomer containing zero to four methylene groups. The results indicate that the species with zero methylene group performed significantly worse across all categories. In terms of surface hydration, the species with one methylene slightly underperforms compared to those with 2-4 methylene groups, all of which demonstrated a similar level of performance. The lowest surface hydration energy is observed for the species containing 3 methylene groups and this energy remains relatively similar between species containing 3 to 8 methylene groups. Overall, this simulation suggests that a zwitterionic surface is effective at resisting fouling if the opposite charges are separated by least one methylene group in distance.

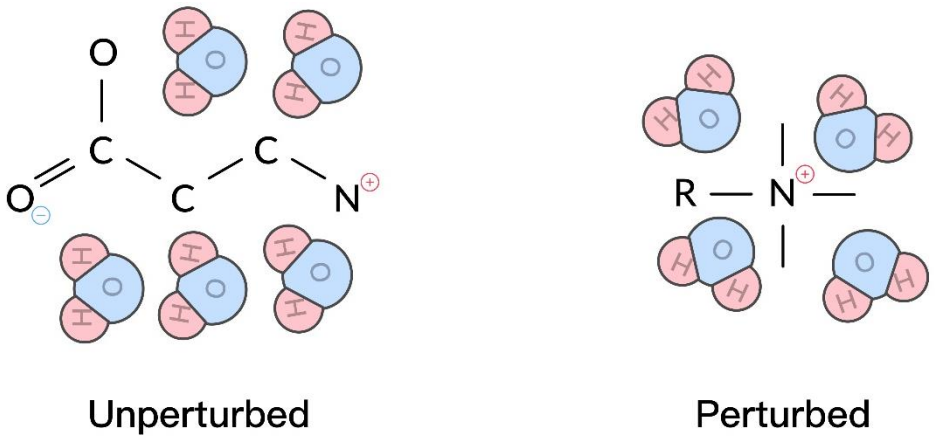

Figure 17: An illustration of two possible structures of associated water molecules
The structure of associated water molecules that is beneficial to antifouling is a contradicting topic. One line of argument indicates that forming a strong ionic interaction with the associated water, and perturbing its structure, will create an energy barrier that protein must overcome in order to adsorb onto the surface. Another line of argument indicates that if the associated water is in a similar state as bulk water (unperturbed), then protein adsorption is not favorable because replacing a protein/water interface with a protein/surface interface will not gain any free energy.

4.3.3 Steric Repulsion and Ion-Coupled Driving Force

The two concepts discussed in this section are relevant to a wider variety of surfaces as opposed to only hydrophilic and zwitterionic. Steric repulsive force is attributed to the compression of polymer brush

network, such as PEG[12, 193], due to the invasion of adsorbates. This compression will reflect in an unfavorable entropy penalty arisen from the loss of configurational entropy of the polymer chain and from the displacement of water to create osmotic pressure. Therefore, long polymer chains are often preferred when designing an antifouling surface in order to benefit from the steric repulsive force. The adsorbed protein will often denature to gain conformation entropy.

Not all hydrophilic surfaces resist protein fouling. Silica, for example, is strongly hydrophilic, but is prone to protein adsorption. Therefore, there must be additional force(s) in play beyond simple hydration that governs protein adsorption. Recent colorimetric study of HSA adsorbed onto silica powers reveals that the adsorption process is actually endothermic[194]. For the adsorption to be spontaneous, there should be a stronger entropic gain. An ion-exchange mechanism was proposed by Schlenoff *et al.*[195] to account for the entropic driving force. The adsorption of a positive protein domain onto the negative silica surface will result in the formation of ion-pairs that release twice the amount of counterions and the net entropy gain is approximated to be kT for each ion released[196]. Due to their intrinsic charge neutrality, zwitterionic or hydrophilic surfaces are unlikely to form ion pair with the adsorbate because no ions can be released from the surface. This ion-coupled driving force speculates why some hydrophilic surfaces are not resistant to protein fouling.

4.4 Cysteine Molecular Dynamic Simulation

In order to determine the antifouling property of zwitterionic cysteine from a molecular perspective, the hydration layer of zwitterionic cysteine was investigated through molecular dynamic simulation and the quantified results compared to the findings presented earlier in this chapter. This section will discuss the zwitterionic cysteine model, molecular dynamics methodology and simulation results.

4.4.1 Simulation Methodology

The cysteine model was acquired from the New York University library database in a .pdb format[197] and converted to a zwitterionic state by removing the hydrogen on the carboxyl group and adding an extra hydrogen to the amine group. The zwitterionic cysteine was placed in the center of a cubic box where the edge of the box was at a distance of 1.0 nm from the cysteine molecule. The simulation box was solvated with 541 water molecules which are described by the SPC/E model because this model adequately describes the dipole moment, dielectric constant, and diffusion property of water molecules[198]. The OPLSAA force field[199, 200] was used to describe the bonding and nonbonding interactions in the system.

The energy of the solvated system was minimized in a ~10 ns molecular dynamics simulation (MD) that processed until the maximum force was less than 50 .0 kJ/mol/nm with an energy step size of 0.01. After energy minimization, the system was equilibrated in a canonical ensemble (NVT) for 1 ns with a step size of 2 fs. Afterward, the system was equilibrated in an isobaric-isothermal ensemble (NPT) for 1 ns with a step size of 2 fs. After the two equilibrium steps, a 30 ns simulation was performed without position constraints and with a step size of 2fs. In all the MDs, the short-range electrostatic and van der Waals cutoffs were set to 1.0 nm. The temperature coupling was done using the Berendsen Thermostat algorithm[201, 202] and set to 300K with a 0.1ps time constant. The pressure coupling, disabled in NVT ensemble, was done using the Parrinello-Rahman algorithm[203] and set to 1 bar with a compressibility of 4.5×10^{-5} bar^{-1} (isothermal compressibility of water). The simulations were done using Gromcs.2016.2. Figure 18 provides an illustration of simulation box captured using VMD.

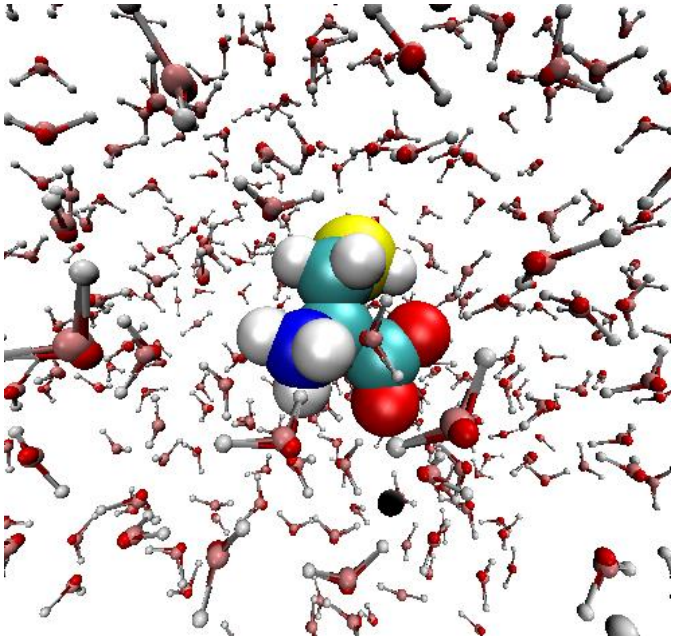

Figure 18: Simulation Box Containing Zwitterionic Cysteine
Generated by VMD. Atoms include: Oxygen (Red), Nitrogen (Blue), Carbon (Green), Sulfur (yellow)

4.4.2 Hydration of Cysteine

The system was relaxed over 10ns and Figure 19 illustrates the change in potential energy over simulated time. The graph converges to just below $-3x10^4$ kJ/mol, indicating that the system was well relaxed. As discussed in earlier parts of this chapter, the water molecules associated with the charged moieties of a zwitterionic molecule are the primary contributors to the material's antifouling performance. To study the important interactions between water molecules and the zwitterionic cysteine, we must first define a spatial distribution of which water molecules are considered associated with the charged groups. This distance of solute-water distribution is often represented by the radial distribution function and the first minimum of the function defines the hydration shell, as discussed in Section 4.3.1. The radial distribution functions (RDF) are acquired between the charged moieties and the oxygen atoms of water molecules in accordance to publish results[187]. For example, the RDF for the negatively charged carboxyl

terminal of zwitterionic cysteine was generated between the oxygen atoms of the carboxyl and the oxygen atoms of water molecules. Figure 20 illustrates the RDF for the charged carboxyl and amine groups of zwitterionic cysteine.

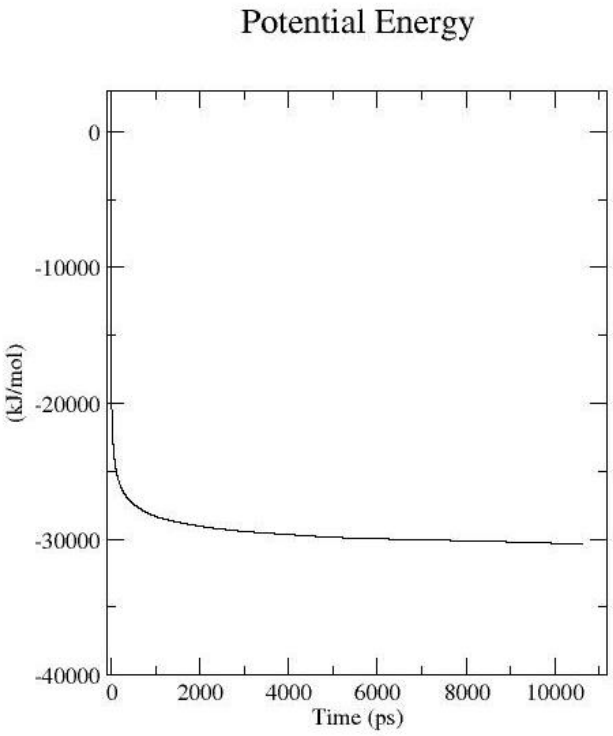

Figure 19: Energy Minimization for the Simulated Environment.
The energy minimization step was done over 10.614 ns and until the maximum force was less than 50 .0 kJ/mol/nm.

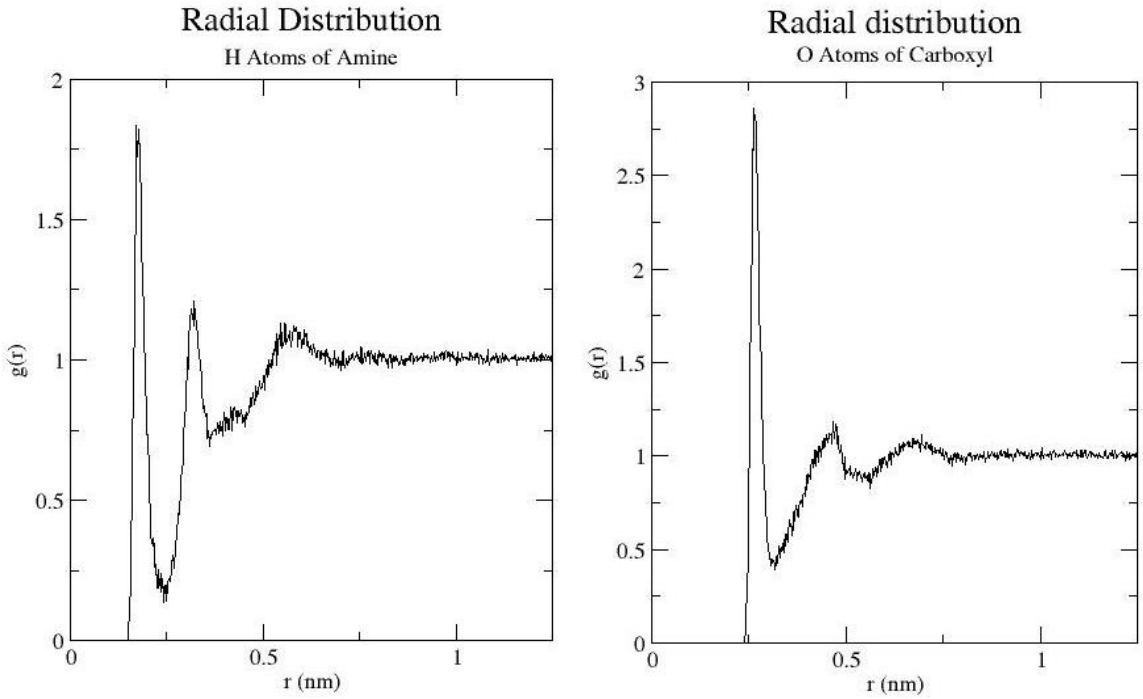

Figure 20: Radian Distribution Function of the Charged Groups
RDF of cationic amine terminal (left) and anionic carboxyl terminal (right).

The RDF of the carboxyl terminal contains a maximum at around 0.25 nm and a minimum at 0.315 nm. The significant maximum indicates the existence of a coordination shell around the carboxyl group. The RDF of the amine terminal contains a maximum at around 0.172 nm and a minimum at 0.25 nm. Similarly, a significant maximum was observed for the amine group. The difference in correlation between the maximum and minimum for the carboxyl group is comparable to sulfobetaine (SB), but less than carboxybetaine (CB). However, the difference for the amine group is significantly larger than both CB and SB, by almost three times[187]. This observation suggests that water is more coordinated around the amine group of cysteine than the methyl groups in CB and SB ($N(CH_3)_3^+$). Based on these findings, the radius of the hydration shell for the charged carboxyl group is 0.315 nm and for the amine group is 0.25nm. These results align very closely with the published result[186].

The number of water molecules inside the hydration shell (N_w) strongly correlates to a material's antifouling performance as discussed earlier in this chapter. The water molecules associated with the charged moieties of zwitterionic cysteine over the course of the simulation is presented in Figure 21. Calculations show that the average number of water molecules associated with the anionic carboxyl is 5.56 ± 0.71 and with the cationic amine group is 3.07 ± 0.48. These values are significantly larger than those observed for EG monomers, which only associate a maximum average of 0.44 hydrogen bonds per monomer when polymerized[52]. Compared to the anionic carboxyl group on CB, N_w = 5.94, cysteine performed similarly. Compared to the anionic SO_3^- on SB[187], cysteine has one less associated water. This observation is expected because the anionic sulfonate group contains one extra oxygen compared to the carboxyl on cysteine. Compared to the cationic $N(CH_3)_3^+$ on SB and CB[187], N_w = 18.64, the amine group associates a lower amount of water; however, this difference in number does not account for the size and number of the molecules in the methyl groups. The N_w for SB and CB were calculated based on the three CH_3, which include a total of 12 atoms as oppose to the mere three H atoms present on the amine group. In addition, the size of these H atoms is also significantly smaller than that of the carbon atoms. The combination of these differences is reflected in the large hydration radius observed for $N(CH_3)_3^+$ (0.46 nm). To put these values into context, the volume of the hydration shell for $N(CH_3)_3^+$ is 6.23 times larger than that of amine, which roughly equals the difference in associated water molecules (6.07 times)[187]. Incorporating the volume of the hydration shell, zwitterionic cysteine associates 43.89 water molecules per nm^3, which is comparable to that of SB and CB (47.19/nm^3 and 44.91/nm^3 respectively)[187]. The same simulations on cysteine were repeated at the average body temperature, 37ºC, and the number of associated water molecules is almost identical to the simulation at room temperature (5.54 ± 0.72 and 3.02 ± 0.49 for the carboxyl and amine groups, respectively). The MD results presented in this section indicate that zwitterionic cysteine is a very promising antifouling material and it exhibits a hydration

layer that is comparable to SB and CB, which are widely recognized as the flagships for zwitterionic antifouling coating.

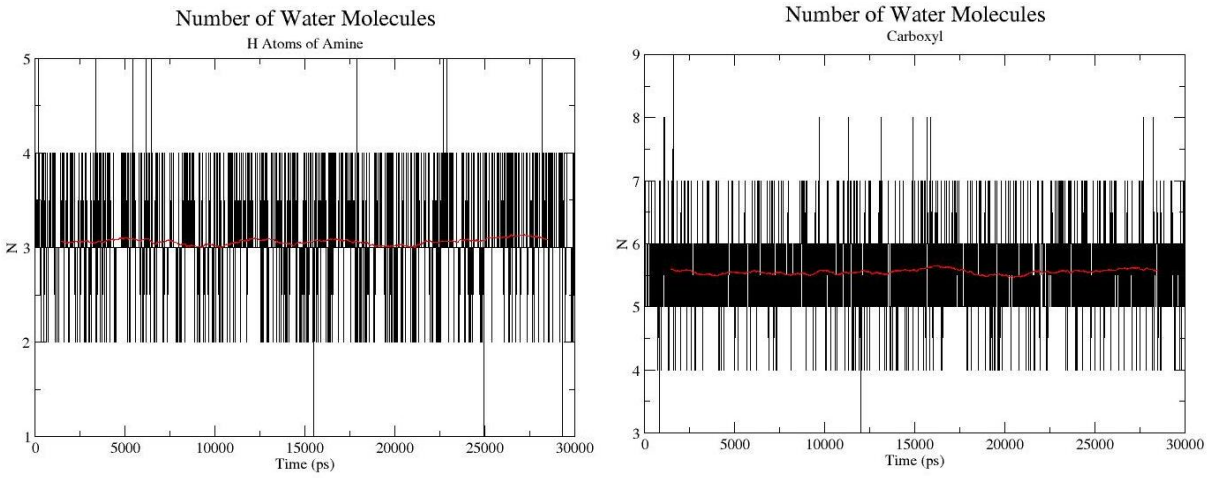

Figure 21: Number of Associated Water Molecules
Change in the number of associated water molecules with respect to simulation time for the amine group (left) and the carboxyl group (right). The average number of associated water molecules are 3.07 and 5.56, respectively.

4.5 Conclusion

This chapter highlights the various mechanisms contributing to the antifouling behavior of a material. It is widely accepted that surface hydrophilization is the primary method for creating antifouling surfaces and the properties of the hydration layer will dictate a material's antifouling performance. Quantification of the amount and mobility of associated water molecules allows for comparison between the hydration layers formed by different materials. The structure of associated water molecules that is beneficial for antifouling is a contradicting topic. Arguments supporting both perturbing and perturbing the surrounding water network are discussed. Factors beyond surface hydration that contributes to antifouling, such as steric repulsion through the compression of polymer chains and ion-coupling, are also outlined.

Simulation results indicate that almost all zwitterions outperform poly(ethylene glycol), a flagship representing traditional hydrophilic antifouling coatings. MD investigations into the hydration layer formed by cysteine demonstrate that it is a promising candidate for protein-resistant material. Although cysteine does not perform as well as zwitterions such as MPC or SB in simulations, the results were comparable and cysteine is advantageous in its shorter chain length and ease of synthesis. Complex synthesis of zwitterionic monomers, such as MPC, limit their applications.

Chapter 5
Fabrication of Highly Zwitterionic Cysteine SAM Through Solution Chemistry

5.1 Summary

Zwitterionic polymers have recently demonstrated superior performance compared to traditional hydrophilic polymers in resisting biofouling due to their overall electrical neutrality and their ability to form a highly-hydrated layer through strong electrostatic interaction. Cysteine is a promising candidate for antifouling coating because the molecule is small, biocompatible, and zwitterionic under physiological pH. Coating thickness is critical for applications involving electric pulses, such as electrotherapeutic device, where the curative electric signal decays proportionally with the thickness of the coating as governed by Coulomb's law. The work presented in this chapter is the first of its kind to fabricate, through solution chemistry, a monolayer of cysteine exhibiting zwitterionic state as high as 95%. X-ray photoelectron spectroscopy analysis of the sulfur 2p emission line demonstrated an absence of secondary layers and confirmed that the fabricated coatings are indeed one monolayer in thickness. The carbon (C1s) and nitrogen (N1s) spectra indicate that 80.53% of the cysteine self-assembled monolayer (SAM) is zwitterionic for samples created at room temperature and this zwitterionic fraction is increased to 94.5% for SAMs created at 330K. This increase in the zwitterionic fraction is attributed to a reconfiguration of the bonds between cysteine and the underlying gold substrate observed at a higher temperature. Irradiation damage to the SAMs in the form of C-S bond cleaving was observed during prolonged XPS analyses and is discussed. The adsorption kinetics of cysteine SAM on a gold surface was examined using a dynamic quartz crystal microbalance in real time. The experimental data can be described by Langmuir adsorption isotherm and were fitted using both OriginPro and MatLab. The dissociation constant is negligible as expected from the strong thiol-on-gold bond. The results reported

in this study demonstrate that highly zwitterionic cysteine SAMs can be fabricated through solution chemistry and has the potential of serving as an effective antifouling coating.

5.2 Introduction

Surface properties of biomaterials and bioelectronics are of tremendous importance in determining their biocompatibility and biofunctionality *in-vivo*. Complex interactions governed by surface topology, van der Waal's interactions, electrostatic interactions, hydrogen bonding, and hydrophobic interactions[204-209] dictate the degree of nonspecific biomolecular fouling, which is one of the major contributors to device failure[1, 40, 41]. In an attempt to control these interfacial interactions, enormous efforts have been devoted to developing engineered surfaces that are hydrophilic, well solvated, and high in conformational freedom[7]. Surface modification with a self-assembled monolayer is an effective method for creating an orderly packed coating exhibiting consistent properties throughout the interface. SAMs of polymer brushes, such as poly(ethylene glycol) (PEG), have long been reported to reduce biomolecule, cell, and bacteria fouling[210, 211]. However, PEG has a number of inherent limitations, including thermal instability above 35°C[92] and oxidation under physiological conditions[49, 212].

As discussed in Chapter 2, zwitterionic polymers have gained tremendous popularity as a PEG-alternative for surface modification. Jiang's group reported zwitterionic carboxybetaine (CB) and sulfobetaine (SB) SAM are capable of reducing protein fouling to the ng/cm^2 range[181, 182, 213]. Chen *et al.* reported that a mixed SAM of 1:1 alternating Glu/Lys or Asp/Lys[118] exhibited ultra-low protein adsorption in the range of <0.3 ng/cm^2.

The results presented in Chapter 3 as well as by Chu *et al.*[214] demonstrated that surface modification with a monolayer of cysteine is a promising new avenue for creating protein resistive coatings. Being an amino acid that naturally exists in the body, cysteine is highly biocompatible and zwitterionic under

physiological pH. In addition, the small molecular structure of cysteine ensures that the monolayer coating will be extremely thin at 7.1Å[215-217]. Coating thickness is critical for applications involving electric pulses, such as electrotherapeutic device, where the curative electric signal decays proportionally with the thickness of the coating as governed by Coulomb's law. Finally, the sulfhydryl group on cysteine allows for easy and established self-assembly onto a gold surface through a strong Au-thiol chemical bond (184 kJ/mol)[218] and desorption of the monolayer is often considered insignificant[219]. Recent studies have shown that cysteine as a coating material is capable of stabilizing both silicon and gold nanoparticles in protein solutions with minimal protein adsorption[117, 141].

Molecular simulations and experimental analyses presented in Chapter 4 have shown that the hydration layer formed on zwitterionic surfaces through electrostatic interactions is responsible for the materials' antifouling property[179],[7],[19]. However, few studies have been done to investigate the overall degree of ionization, chemical stability, and adsorption mechanism of a cysteine SAM fabricated through solution chemistry. The closest investigations were completed by Gonella *et al.* through an ultrahigh vacuum deposition using a synchrotron beamline[120, 147, 220]. A major benefit of cysteine SAMs fabricated from solution over those fabricated by evaporation under an ultrahigh vacuum is achieving a higher yield of the preferred zwitterionic state, which is the primary contributing factor for cysteine SAMs' antifouling property[87, 113]. Results presented in this chapter demonstrate the fabrication of a 95% zwitterionic monolayer of cysteine through solution chemistry in phosphate buffered saline. To the author's best knowledge, this is the first demonstration of a confirmed monolayer of self-assembled cysteine fabricated through solution chemistry that exhibited this high level of zwitterionic percentage. Compared to cysteine SAMs fabricated though ultrahigh vacuum deposition[120], the cysteine SAMs fabricated in this study through solution chemistry demonstrated over one-and-a-half times of improvement in zwitterionic fraction (from ~60% to 95%). The effect of reaction temperature was investigated by fabricating cysteine

SAMs at room temperature and 330K. The fraction of zwitterions, as well as layer thickness, were confirmed through a thorough elemental analysis of the cysteine-on-gold SAMs by using x-ray photoelectron spectroscopy (XPS). A quartz crystal microbalance was used to monitor the self-assembly of cysteine onto a gold surface in real-time and the adsorption kinetics was determined by fitting the experimental data.

5.3 Materials and Method

5.3.1 Materials

L-cysteine ($HSCH_2CH(NH_2)(CO_2H)$, 97% purity) was used as received from Sigma-Aldrich. Phosphate buffered saline (PBS) was purchased from Invitrogen and Sigma-Aldrich.

5.3.2 X-ray Photoelectron Spectroscopy (XPS)

Samples were fabricated by coating 10 mm by 5 mm by 3 mm (length, width, height) rectangular cyclic olefin copolymer (COC) substrates with 10 nm of zinc oxide (ZnO) followed by 48 nm of the gold film. The substrates were submerged in 0.1 mM of L-cysteine in PBS buffer for 16 hours followed by 3 hours of post reaction wash in PBS solution. The reactions were allowed to continue at either room temperature or 330K. The samples were dried with nitrogen and loaded into the XPS chamber immediately. Samples were characterized by ESCALAB 250Xi X-ray photoelectron spectrometer (Thermo Scientific). The X-ray gun was set to image a 500 μm^2 area at 15kV and 150W power at 80% dispersing power. Elements investigated were gold (Au_{4f}), carbon (C_{1s}), oxygen (O_{1s}), sulfur (S_{2p}), nitrogen (N_{1s}) for 1, 36, 29, 60, and 60 scans respectively and the scan total time was kept under 2 hours for each sample. A background XPS reading was acquired on an untreated gold substrate at the same time as the samples by scanning the identical elements for the identical number of scans. The results were analyzed using the software CasaXPS.

5.3.3 Quartz Crystal Microbalance (QCM)

The QCM measurements were performed at room temperature with the AT-cut quartz crystal from ANT technology Co., Ltd. (Taipei, Republic of China). Frequency shift was detected by the Affinity Detection System (ADS) type QCM instrument from the same manufacturer. The frequency of the loaded crystal (f_0) was 8.97MHz with a standard deviation of 0.026%. The piezoelectrically active crystal area was 0.1cm^2 given by the manufacturer. The samples were allowed ample time to establish a stable baseline under a continuous flow of phosphate buffered saline (PBS) before a 0.1 mM cysteine solution in PBS was introduced to the system. The time required to establish a steady baseline varied among samples, and only the portion of data directly proceeding the introduction of a cysteine solution was presented in the figures to allow for easy viewing of the data. The baseline was considered stable when the change in resonance frequency falls within the machine's inherent signal drift given by the manufacture as ±0.3Hz per minute. The signal drift, which is considered as a background noise, was removed from the data using a calibration process provided with the manufacture's signal acquisition software. After exposing the sample surface to the cysteine solution, a PBS solution was again flowed across the sample surface and the resonance frequency was allowed time to stabilize. The change in frequency, ΔF, was calculated by subtracting the frequency of PBS baseline from PBS wash.

5.4 Discussion

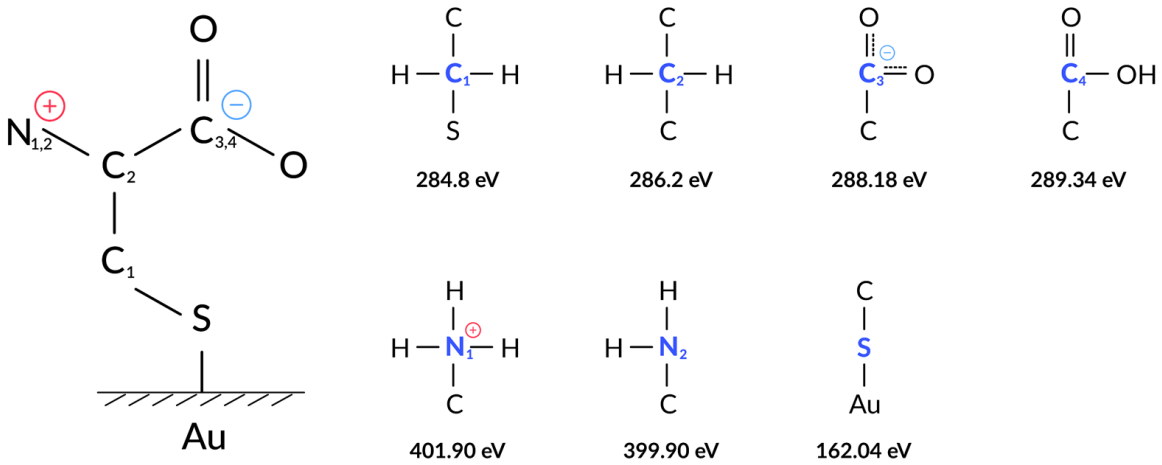

Figure 22: Schematic representation of cysteine on a gold substrate and its possible species
Values are the expected peak positions acquired using XPS. Hydrogen atoms are not shown on the cysteine structure to ensure clarity of the illustration.

5.4.1 Monolayer Composition

The presence of a zwitterionic cysteine monolayer was confirmed by the XPS analysis. Under physiological pH, the carboxyl group of cysteine will be deprotonated and become negatively charged, whereas the amine group will be protonated and become positively charged. Thus, to ensure that cysteine is in its zwitterionic configuration, the molecule must be anchored through the sulfur head to expose both the amino and carboxylate groups. However, previous studies have suggested that a portion of cysteine initially adsorbs via the amino group onto a gold substrate before reorienting itself to the more stable thiol bond as coverage increases over time[219, 221] and, from a thermodynamics perspective, a higher temperature will promote this reorientation. This investigation provides key understanding on the effect of temperature towards the molecular orientation of the chemisorbed cysteine, surface coverage, and a

percentage of the monolayer that is in the preferred zwitterionic state. Two reaction temperatures, room temperature and 330K, were studied.

The photoelectron spectra of gold for both temperatures showed the characteristic bulk Au $4f_{7/2}$ doublet situated at 83.98 ± 0.02 eV and 87.66 ± 0.01 eV (Supplementary Figure S3). Since the gold peaks were almost identical to the theoretical value at 83.97 eV, no additional calibration was made in this study towards the binding energy (BE) scale. The spectral region of the sulfur S2p core level (Figure 23) shows a doublet composed of two peaks located at 162.04 ± 0.03 eV and 163.17 0.01 eV with the same full-width half maximum (FWHM) of 0.8 eV. The peak profile of this doublet aligns with the reported spin-orbit induced energy splitting of the sulfur 2p core level into $2p_{1/2}$ and $2p_{3/2}$ energy states approximately 1.18 eV apart with a ratio intensity of 2:1 that is common for organosulfur molecules on gold[222-227]. Indeed, this characteristic doublet represents the thiolate species formed by a chemical reaction between the thiol on cysteine and the gold substrate[144, 146, 174]. A less intense third peak (S3) was observed at the lower energy shoulder located at 161.30 ± 0.01 eV and can be assigned to parts of a doublet from a different sulfur species. The presence of this motif is speculated to be the result of irradiation damage caused by prolonged exposure to photoelectrons during the XPS analysis. Cavalleri *et al.* reported that the intensity of the S3 component increased significantly with respect to the primary doublet under extended irradiation (2 hours)[220]. Strong evidence reported on other organosulfur SAMs suggest that radiation damage occurs in the form of molecular scission of the C-S bond[224, 226-228] and to a greater degree on short-chain monolayers as a consequence of their weaker barrier property[227]. Indeed, referring to the previous study of multilayer cysteine coating presented in Chapter 3, radiation damage from the XPS analysis was less prominent[174]. It is also interesting to note that the peak position of S3 matches that of atomic sulfur on gold[229]. These findings indicate that prolonged exposure to x-ray causes C-S bond cleaving and produce atomic sulfur that either remains on the gold substrate or redeposits back onto a

neighboring molecule. X-ray damage was unavoidable in this study primarily because a large number of scans (60 scans, ~40 min) was needed for the S2p spectra in order to separate the signal from background noise and signs of radiation damage appear after approximately 5min of exposure[220, 230]. Even with the extensive scanning, the fit for the sulfur spectra still exhibited higher error in a range of 5-7% estimated by Monte Carlo simulation due to the low signal-to-noise ratio whereas the well-defined gold spectra exhibited an error range of only 0.7-1% after only three scans. Comparing the spectra of the two temperatures, the higher reaction temperature resulted in almost doubled the amount of damaged sulfur (13%) compared with the surface created at RT (7.6%). The increase in damage to cysteine SAMs was also previously observed for samples annealed between 80-100°C[220]. It is important to note that the presence of a secondary layer of weakly physisorbed cysteine in the region 164~165.5 eV[120] was not observed; thus, confirming that the fabricated cysteine surface is indeed a monolayer.

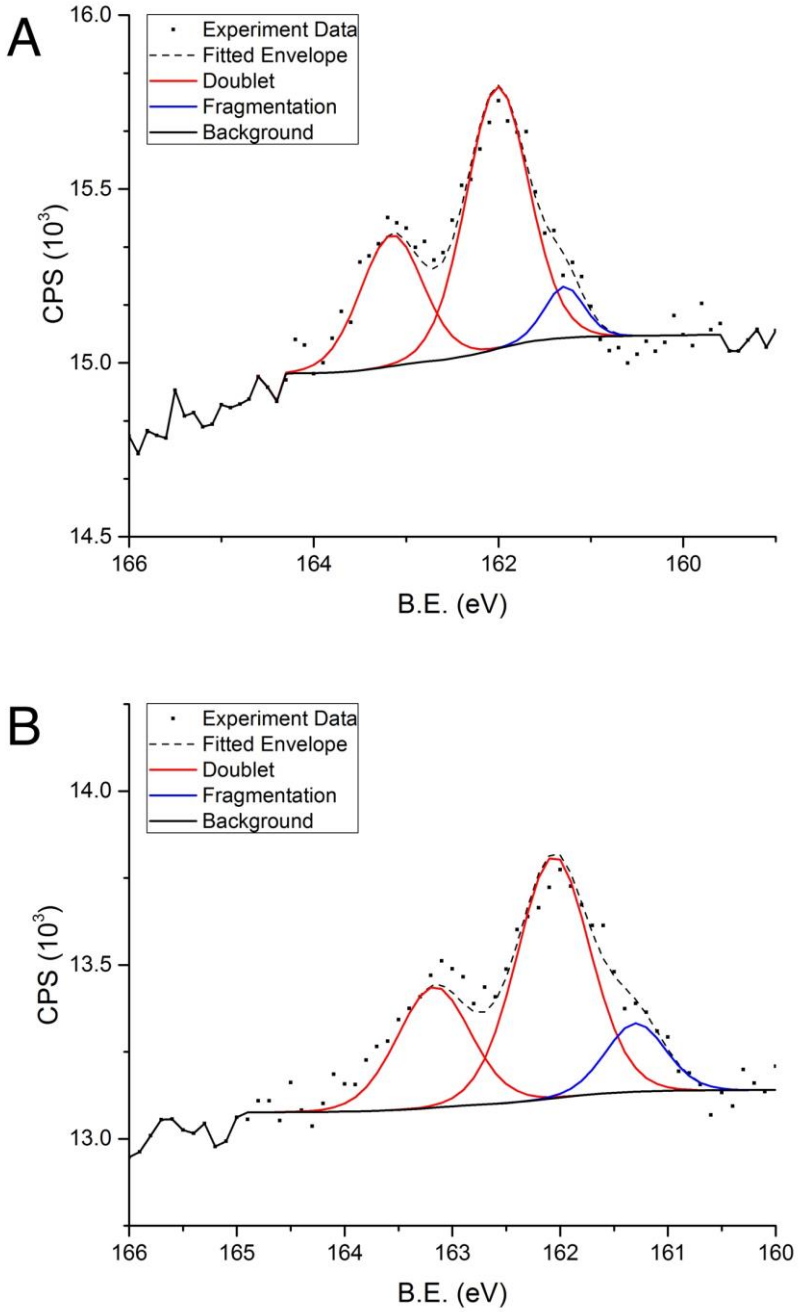

Figure 23: Sulfur 2p XPS spectra of cysteine deposited onto a gold substrate
A) at room temperature B) at 330K.

The spectral region of the carbon C1s core level (Figure 24) confirms the presence of zwitterionic cysteine and its characteristic 4-peak profile. Background readings of untreated gold substrate revealed the presence of organic surface contamination acquired from the ambient environment. Since this study investigates cysteine SAMs fabricated from solution chemistry, exposure to ambient air and the associated contaminants was unavoidable especially during the transport between the deposition step and the analysis step. A similar level of environmental contamination was also observed in other published results involving samples prepared by dipping in an ambient environment[144, 231]; however, for cysteine SAMs prepared and analyzed completely under an ultra-high vacuum, environmental contamination was not observed[120]. A major benefit of cysteine SAMs fabricated from solution over those fabricated by evaporation under an ultra-high vacuum is achieving a higher yield of the preferred zwitterionic state, which is the primary contributing factor for cysteine SAMs' antifouling property[87, 164]. The yield of zwitterionic state will be discussed in detail in a later section. The C 1S core level emission contributed from environmental contaminations was acquired from an untreated gold substrate and subtracted from the spectra of the cysteine samples.

In the resulting spectra (Figure 24), a total of four peaks were identified in the deconvolution of the spectra. Two well-developed peaks positioned at 284.8 eV and 286.2 eV can respectively be assigned to the C1 and C2 carbons as shown in Figure 22. Following the literature of cysteine SAMs assembled under an ultra-high vacuum[120, 146, 149], the C1 peak centered at 284.8 ± 0.08 eV with an FWHM of 0.9 eV matches the characteristic peak profile of a carbon involved in a C-C bonding with a slight shift due to further bonding with sulfur. The C2 peak centered at 286.2 ± 0.1 eV with an FWHM of 1.3 eV matches the peak profile of a carbon involved in the C-N bonding. The intensity or area under the curve of C1 and C2 peaks is almost identical across all samples and this 1:1 ratio confirms the integrity of the cysteine structure from a molecular stoichiometry perspective. A third but much broader peak can be identified in the range

of 187~189 eV, an energy region that is typical of the carboxyl group[120, 146, 148, 149]. Indeed, this broader peak envelope can be deconstructed into two peaks at 288.18 ± 0.07 eV (C3) and 289.24 ± 0.06 eV (C4), and can be assigned to the COO- and COOH moiety respectively[148, 149].

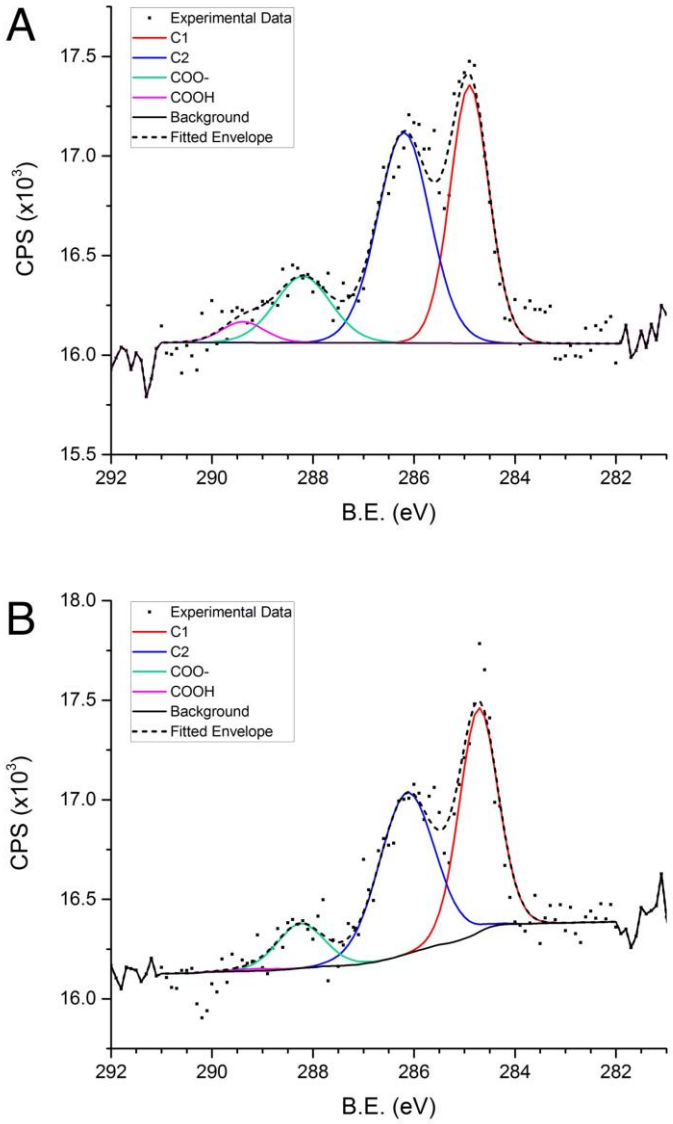

Figure 24: Carbon 1s XPS spectra of cysteine samples deposited onto a gold substrate
A) at room temperature. B) at 330K. To account for surface contamination acquired from the ambient environment, background spectra were acquired from an untreated gold substrate and subtracted from the carbon spectra presented here.

The presence of the unaltered amine group on cysteine as well as its protonated cationic form was confirmed by the nitrogen 1s core level emission lines. As explained in the previous discussion on carbon spectra, the contribution from environmental contaminations was unavoidable and was subtracted from the nitrogen 1s emission. The resulting spectra (Figure 25) can be decomposed into two broad peaks centered at 401.90 eV ± 0.08 eV (N1) and 399.90 eV ± 0.08 eV (N2). These two peaks, approximately 2 eV apart, resemble the characteristic peak profile of NH_2 and NH_3^+ that appears in the region of 399~402 eV[120, 144, 146]. The bonding of an additional cation, in this case, hydrogen, to the amine end group will increase the binding energy of the ionized nitrogen by affecting its electric field in accordance to XPS principles[232]. Thus, the peak with the higher binding energy, N1, is assigned to the ionized NH_3^+ species whereas the N2 peak, having a lower binding energy, is assigned to the neutral NH_2 species. These two nitrogen peaks reported in this chapter are shifted by approximately 0.4 eV compared to the positions reported for cysteine SAMs fabricated through vacuum deposition[120]. We postulate that the shift is caused by the PBS solvent used in the cysteine chemisorption and post reaction rinse. A shift in peak position was also observed in our previous results involving PBS[174]; however, when the identical reaction was completed in DI water in the same study, a shift in peak position was not observed. The shift observed in this study is significantly less than what was observed previously (0.4 eV as oppose to 1.0 eV) and further confirms the absence of secondary physisorbed layers indicated by the sulfur spectra. The use of PBS was done intentionally as the electrolyte concentration of PBS mimics that in a physiological environment. By using a PBS solution, a better representation of the zwitterionic nature of cysteine coating when operating in a physiological environment can be achieved. Similar to the sulfur spectra, the molecular stoichiometry of cysteine compels the ratio of one nitrogen (and sulfur) to three carbons and the reduction in nitrogen quantity is reflected in the poor signal-to-noise ratio of the nitrogen 1s core level emission. Table 8 summarizes the XPS findings presented in this section.

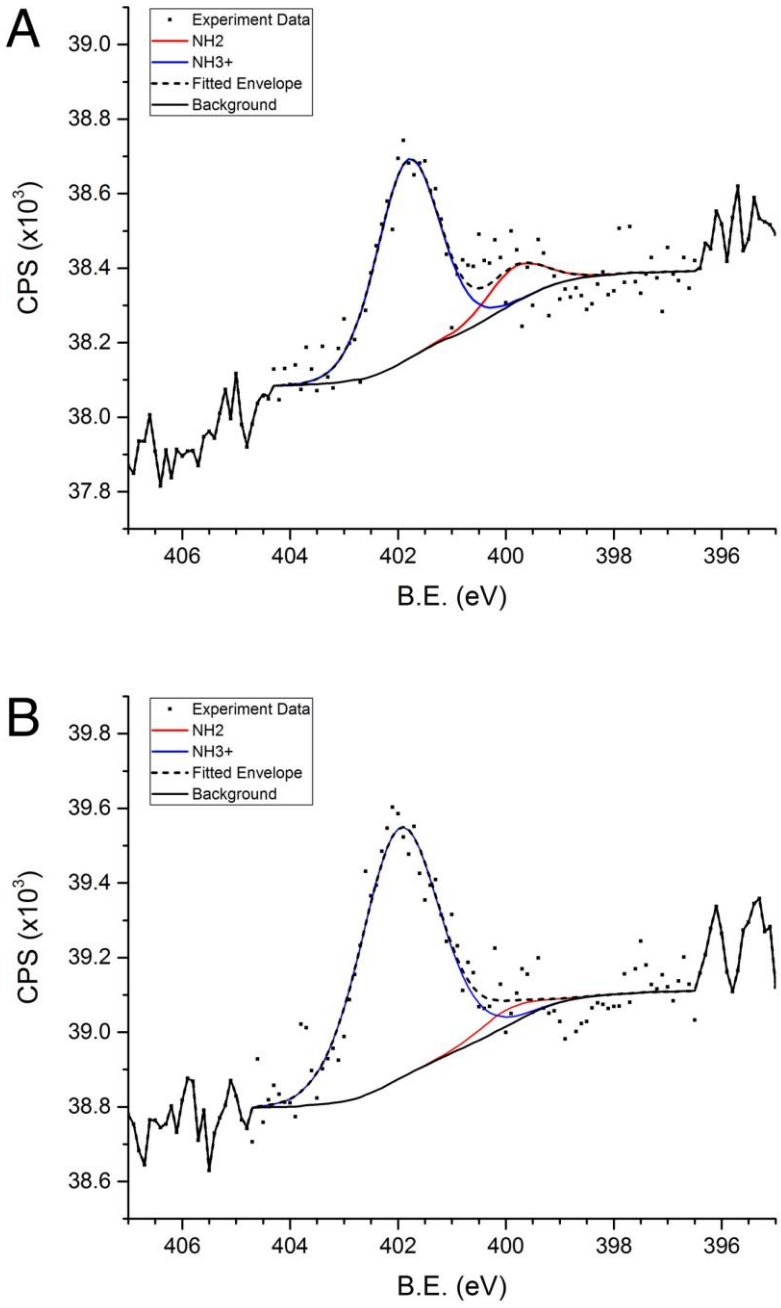

Figure 25: Nitrogen 1s XPS spectra of cysteine samples deposited onto a gold substrate
A) at room temperature and B) at 330K. To account for surface contamination acquired from the ambient environment, background spectra were acquired from an untreated gold substrate and subtracted from the nitrogen spectra presented here.

Table 8. Summary of XPS findings
This table summarizes the findings presented in Section 5.4.1.

	Species	Position (eV)	FWHM (eV)	Area 330K	Area RT
Sulfur 2p	S1	162.04±0.03	0.8±0.01	57.77%	61.61%
	S2	163.17±0.01	0.8±0.01	28.87%	30.79%
	S3	161.30±0.01	0.58±0.075	13.36%	7.60%
Carbon 1s	C1	284.81±0.09	0.90±0.01	43.60%	38.94%
	C2	286.20±0.10	1.26±0.04	45.22%	43.08%
	C3 (COO^-)	288.18±0.07	1.21±0.10	10.67%	14.48%
	C4 (COOH)	289.24±0.06	1.06±0.06	0.50%	3.50%
Nitrogen 1s	N1 (NH_3^+)	401.90±0.08	1.43±0.05	4.65%	14.07%
	N2 (NH_2)	399.90±0.08	1.27±0.02	95.35%	85.93%

5.4.2 Zwitterionic Fraction of Cysteine SAMs

The zwitterionic state of cysteine is achieved by a simultaneous deprotonation of the carboxyl group to form an anionic moiety and protonation of the amine group to form a cationic moiety. Therefore, by investigating the charged fraction of both moieties, the percentage of cysteine that is in its zwitterionic state can be determined. The charged fraction of the anionic carboxyl group (P_{COO-}) can be calculated from the intensity (I) ratio of C3 to C4, where $P_{COO-} = I_{C3}/I_{C3+C4}$. Theoretically, exactly the same fraction of charged carboxyl group can also be obtained from the O1s spectra, where ($P_{COO-} = I_{O531.2eV}/I_{Ototal}$), as demonstrated by cysteine SAMs prepared and analyzed completely under an ultra-high vacuum[120]. In this study, however, regular exposure to oxygen from the ambient environment was unavoidable and thus the contribution to the oxygen spectra is not solely based on the carboxyl group of the cysteine SAM. The oxygen spectrum does not provide a good representation of the percent charged state of the cysteine as the nitrogen spectrum. We believe the carbon spectra provide a better representation of the carboxyl group primarily because the 3:2 atomic ratio of carbon to oxygen based on the molecular structure of cysteine is expected to yield a higher level of carbon contribution over that of oxygen. As a result, the carbon

spectra are less subjectable to errors contributed from environmental contaminations when compared to the oxygen spectra. It is important to note that this claim is only true under the assumption that the error generated by environmental contaminations contribute equally to the oxygen and carbon spectra and since we have not found any evidence that suggests otherwise, we believe this assumption is accurate. Indeed, the total contribution from cysteine observed in the carbon spectra is greater than that in the oxygen spectra. Therefore, the charged fraction of the carboxyl group was calculated based on the carbon contribution involved in the carboxyl moiety.

For the cysteine sample fabricated at room temperature, the charged fraction of the carboxyl group is 80.53% which is in close agreement with our previous study presented in Chapter 3[174]. This fraction increased to 95.50% for samples created at 330K. The increased yield of the anionic carboxyl group from higher reaction temperature is as predicted by the thermodynamics of cysteine adsorption. The second-most preferred orientation of a cysteine molecule adsorbed onto an [110] gold surface is a flat geometry anchored onto the substrate through a thiolate-Au bond, amine-Au bond, and carboxyl-Au bond through the hydrogen bonding[233]. Under a higher reaction temperature, the cysteine molecule will more likely be adsorbed in a less preferred orientation that does not involve the carboxyl anchor, thus releasing the carboxyl group from bonding to the surface and create additional anionic moieties. The release of the carboxyl anchor also frees up an additional adsorption site and allows for additional cysteine adsorption through the thiolate-Au bond. The charge fraction of the cationic amine group can be calculated from the intensity (I) ratio of N1 to N2, where $P_{NH3+} = I_{N1}/I_{N1+N2}$. For samples fabricated at room temperature, the charged fraction of the amine group is 85.95% and increased to 94.47% for samples created at 330K. Similar to the carboxyl group, the increased yield of ionic species (in this case, the cationic amine) from a higher reaction temperature is as predicted by the thermodynamics of cysteine adsorption. A higher reaction temperature releases additional amine anchors, thus allowing the formation of additional cationic

moieties. It is important to note that cysteine molecules adsorbed at lattice defects (steps and grain boundaries) tend to prefer a flat orientation involving sp-bonding and can exhibit a higher affinity towards bind onto the gold substrate through all three end groups[224]. Therefore, increasing the reaction temperature will have less of an effect on these molecules and this may be one of the reasons that is preventing the fabrication of a completely zwitterionic cysteine SAM. In summary, 80.53% of the cysteine SAM is zwitterionic for samples created at room temperature and this zwitterionic fraction is increased to 94.5% for SAMs created at 330K.

This study demonstrates the importance of fabricating cysteine SAMs in a PBS solution. Over 94 % of the SAM fabricated through solution chemistry in this study is zwitterionic. This value is over one-and-a-half times of improvement compared to the cysteine SAMs fabricated though ultrahigh vacuum deposition where only ~60% of the surface is zwitterionic[120]. The zwitterionic nature of the cysteine molecule is what give rise to the antifouling property of the SAMs through the formation of a strong hydration layer[87, 113]. Thus, a higher fraction of surface zwitterions is expected to be more resistant to protein fouling. We believe the presence of PBS buffer during the reaction facilitates the ionization of the carboxyl and amine groups on the cysteine and the absence of this buffer during vacuum deposition is responsible for the lower degree of zwitterionic fraction. A similar phenomenon was observed in our previous study where cysteine surfaces fabricated in Millipore water resulted in a lesser fraction of zwitterions than the surfaces fabricated in PBS buffer[174]. Studies that have shown cysteine SAMs fabricated in other solutions with a similar level of zwitterionic fraction, but did not confirm or was ambiguous on whether the coating was actually a monolayer[146, 148]. Monolayer thickness is critical for applications involving electric pulses, such as electrotherapeutic device, where the curative electric signal decays proportionally with the thickness of the coating as governed by Coulomb's law. To the authors'

best knowledge, this is the first demonstration of a confirmed monolayer of self-assembled cysteine fabricated through solution chemistry that exhibited this high level of zwitterionic percentage.

5.4.3 Kinetics of Cysteine Self-Assembly

A quartz crystal microbalance was used to monitor the self-assembly of cysteine onto a gold surface in real-time. Cysteine is a zwitterionic amino acid under physiological pH through the protonation of its amine group to create a cationic end group and deprotonation of its carboxyl group to create an anionic end group. The molecule is reported to bind to a gold substrate primarily through its thiol group but binding can also involve either or both of the carboxyl and amine groups[233]. Reports indicate that as surface coverage increases, more of the cysteine molecules reorient their binding to only involve the thiol group[219]. It is unclear whether an increase in the number of neighboring cysteines induces the reorientation of the molecule or the reorientation of cysteine allows for an increase in coverage.

We examined the adsorption kinetics of cysteine SAM on gold surfaces using a dynamic quartz crystal microbalance where the change in resonant frequency can be directly translated to a change in adsorbed cysteine. The relationship between a change in frequency (Δ F) and a change in mass at a liquid interface can be expressed by Sauerbrey Equation in a solution (Equation 1)[234-236],

$$F = -\frac{2f_0^2}{A\sqrt{\rho_q \mu_q}} m - \frac{f_0^{3/2}}{\sqrt{\pi \rho_q \mu_q}} (\eta_L \rho_L)^{1/2}$$

$$\Delta F = -\frac{2f_0^2}{A\sqrt{\rho_q \mu_q}} \Delta m - \frac{f_0^{3/2}}{\sqrt{\pi \rho_q \mu_q}} \Delta (\eta_L \rho_L)^{1/2}$$

Equation 1

$$\boldsymbol{\Delta F = -C_1 \Delta m - C_2 \Delta (\eta_L \rho_L)^{1/2}}$$

Where ρ_q is the density of quartz crystal (2.648 g·cm^{-3}), μ_q is the shear modulus of quartz (2.947x10^{11} g·cm^{-1}·s^{-2}), f_0 is the frequency of the loaded crystal, A is the piezoelectrically active crystal area (given

by the manufacturer as 0.1 cm^2), Δm is the change in mass, η_L is the viscosity of the liquid and ρ_L is the density of the liquid. Assuming that the change in viscosity and density of the solution is negligible during the experiment ($\Delta\sqrt{\eta_L\rho_L} = 0$), the change in frequency can be directly translated the change in surface adsorbents where $\Delta F = -C_1\Delta m$. The intrinsic constants (C_1) of each chip vary slightly with respect to the intrinsic frequency of the loaded quartz crystal (f_0), but the variance is very low (0.026%), and the deposited mass can be related to the resonance frequency in this study by:

Equation 2 $$\boldsymbol{\Delta m\ (ng) = -0.549 \pm 0.00030 \Delta F (Hz)}$$

Figure 26 illustrates the real-time adsorption of cysteine from a PBS solution onto a gold substrate at room temperature. The adsorption kinetics can be described by the Langmuir adsorption isotherm where the fraction of available sites (Θ) can be related to the concentration (C) by:

$$\frac{d\theta}{dt} = k_a(1-\theta)C - k_d\theta$$

Equation 3 $$\boldsymbol{\theta = \frac{C \cdot k_a}{C \cdot k_a + k_d}\left(1 - e^{-(C \cdot k_a + k_d)t}\right)}$$

k_a is the association constant, k_d is the dissociation constant. Two numerical solvers, MatLab and OriginPro 2016, were used to fit Equation 3 to the QCM data. The initial spike in the QCM data is an artifact of the experimental procedure caused during the switch between solutions. During this step, the flow speed was temperately increased to ensure that the new solution was introduced to the sample surface as soon as possible. If the flow speed was not increased, the newly introduced biomolecules would have been given enough time to diffuse into the previously introduced buffer solution in the machine tubing and create an unnecessary concentration gradient (splash-over effect). The necessity to increase the flow speed combined with the possible introduction of small air bubbles oftentimes created significant spikes and/or dips in frequency readings that shortly follows the introduction of a new solution. This

artifact was removed from the curve fitting process by ignoring data points prior to 1500 seconds. The fitted graph by OriginPro using nonlinear curve fitting through orthogonal distance regression algorithm is illustrated in Figure 26 and the R^2 value was calculated to be 0.97997. The estimated kinetic parameters are k_a = 4.20902 L•mol^{-1}•s^{-1} (standard error of 0.00496) and k_d = 0 (standard error of 0.00153). These parameters are almost identical to those estimated through a curve fitting by MatLab where k_a = 4.21031L•mol^{-1}•s^{-1} and $k_d = 2.66 \times 10^{-9}$ (R^2 = 0.98001). The almost negligible desorption of cysteine is as expected since the strength of the thiol-on-gold chemisorption bond is large (125-167 kJ/mol)[237, 238] and any desorption is unlikely as reported in an SPR study by Tawil *et al.*[219].

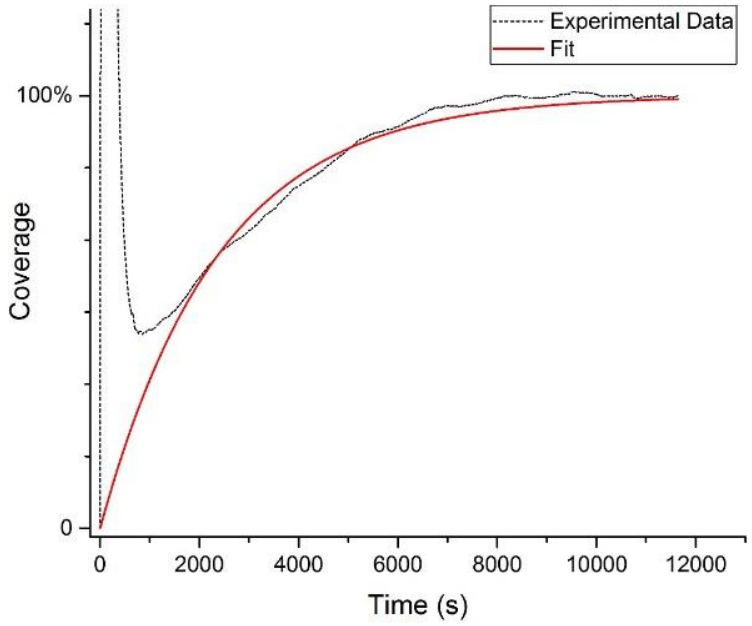

Figure 26: The adsorption of cysteine onto a gold surface
The dotted line represents experiment data monitored in real-time by a QCM. The solid line represents the result fitted using OriginPro. The initial spike is an artifact of the experimental procedure and experimental data prior to 1500s are ignored. The R^2 value is 0.97997.

5.5 Conclusion

Zwitterionic cysteine self-assembled monolayers were successfully fabricated through solution chemistry on gold-coated cyclic olefin copolymer substrates. X-ray photoelectron spectroscopy analysis of the sulfur 2p emission line demonstrated an absence of secondary layers and confirmed that the fabricated coatings are indeed one monolayer in thickness. The fraction of cysteine SAMs in its zwitterionic state was calculated by assessing the carbon (C1s) spectra of the carboxyl group and the nitrogen (N1s) spectra of the amine group. 80.53% of the cysteine SAM is zwitterionic for samples created at room temperature and this zwitterionic fraction is increased to 94.5% for SAMs created at 330K. The increase in the zwitterionic fraction is attributed to a rearrangement of the bonds between cysteine and the underlying gold substrate. At a higher reaction temperature, cysteine molecules will more likely be adsorbed in a less preferred configuration that does not involve either the carboxyl or amine end group. The release of these end group from binding to the gold surface will allow for additional ionic moieties and hence an increase in the zwitterionic fraction. Prolonged exposure to x-ray during XPS analysis was necessary to acquire meaningful results, but causes C-S bond cleaving and produce atomic sulfur that either remains on the gold substrate or redeposits back onto a neighboring molecule. The adsorption kinetics of cysteine SAM on gold surfaces was examined using a dynamic quartz crystal microbalance in real time. The experimental data can be described by Langmuir adsorption isotherm and were fitted using both OriginPro and MatLab. The dissociation constant is negligible as expected from the strong thiol-on-gold bond. The results reported in this study demonstrate that highly zwitterionic cysteine SAMs can be fabricated through solution chemistry and has the potential of serving as an effective antifouling coating.

Chapter 6
Low-Fouling and Ultra-Thin Zwitterionic Cysteine SAM: A QCM and SPR Study

6.1 Summary

Surface fouling with unwanted biological solutes is an exigent issue for any biological implants as these foulants greatly reduce device efficiency and hasten degradation. Surface modification with antifouling polymers has become indispensable for prolonging the longevity of modern devices *in-vivo*. Recently, zwitterionic self-assembled monolayers have been the focus of antifouling coatings due to their overall electrical neutrality and ability to capitalize on strong electrostatic interaction to form a highly hydrated layer. Numerous reports using various composition of zwitterionic polymer brushes have demonstrated ultra-low fouling in the ng/cm^2 range; however, for electrotherapeutic devices, the thick polymer brush coatings significantly hinder the effectiveness of the curative electrical pulse as governed by Coulomb's Law. Herein we report an antifouling surface composed of 8.64Å (1.22 monolayer) of zwitterionic cysteine fabricated through an economical thiol chemistry in solution. The antifouling performance of this surface was evaluated in bovine serum albumin (BSA), fibrinogen, and human blood by quartz crystal microbalance (QCM) and compared to an untreated gold surface. The cysteine surface demonstrated 95% reduction (44 ng/cm^2) to BSA adsorption after 3 hours and 90% reduction after 24 hours. Similarly, the cysteine surface is able to achieve 93% reduction to fibrinogen adsorption as well as human blood. The surfaces were imaged with scanning electron microscopy and cellular adsorption was not observed on the cysteine surface, but was prominent on the gold surface. These findings suggest that a zwitterionic cysteine surface is capable of resisting the adsorption of key proteins in the signaling cascade for inflammatory cells. Surface plasmon resonance imaging was used to complement the results of the QCM. The results reported in this chapter demonstrate that cysteine, due to its zwitterionic nature,

biostability, and small size, is a promising alternative candidate to the conventional PEG-based materials for improving the long-term biofunctionality of implantable bioelectronics.

6.2 Introduction

Recent advances in biotechnology have enabled more sensitive diagnostic sensors and effective therapeutic devices. However, rapid device degradation, caused by surface oxidation, fibrous encapsulation and/or nonspecific protein fouling, continues to be a pervasive obstacle to the success of these bioelectronics *in-vivo*[7, 239, 240]. Taking implantable glucose sensors as an example, the current minimally invasive glucose sensors approved by the FDA are only capable of performing optimally for 7 days once implanted[5]. Long-term biocompatibility and biofunctionality *in-vivo* are arguably one of the major obstacles that are hindering bioelectronics from becoming a conventional treatment in clinical care and from receiving the popularity that these devices deserve[241-243].

Protein fouling, in the form of nonspecific adsorption, is one of the major contributors to device failure that occurs in the very early stages of implantation[1, 40, 41]. Upon surgical insertion, the surface of the device is spontaneously covered with a layer of plasma proteins which triggers a cascade of host responses that ultimately result in fibrous encapsulation, where the device becomes isolated by a layer of fibroblast or smooth muscle cell sheet[29, 30]. Formation of the fibrous capsule will prevent further interaction of the bioelectronics with the surrounding host environment and will compromise the functionality of the device. As a result, implanted bioelectronics often require a secondary surgery to remove or replace the device.

Recent strategies for extending the lifetime of implantable bioelectronics focus on minimizing the amount of nonspecific plasma protein adsorption at the initial stage of implantation[3, 41, 244], with special emphases on self-assembled zwitterionic molecules as a nonfouling coating[49, 134, 174]. Figure 27 provides

a cartoon illustration of a zwitterionic antifouling surface in action. As discussed in Chapter 2, zwitterions are molecules that consist of an equal ratio of positive and negative charges in close proximity, and thus preserve an overall electrical neutrality, which is essential for anti-fouling surfaces[49]. Chapter 4 discussed the importance of forming a layer of tightly bonded water molecules through ionic solvation[58, 175] that allows zwitterionic surfaces to exhibit superior performance in resisting protein fouling compared to conventional hydrophilic polymers such as (PEG)[19].

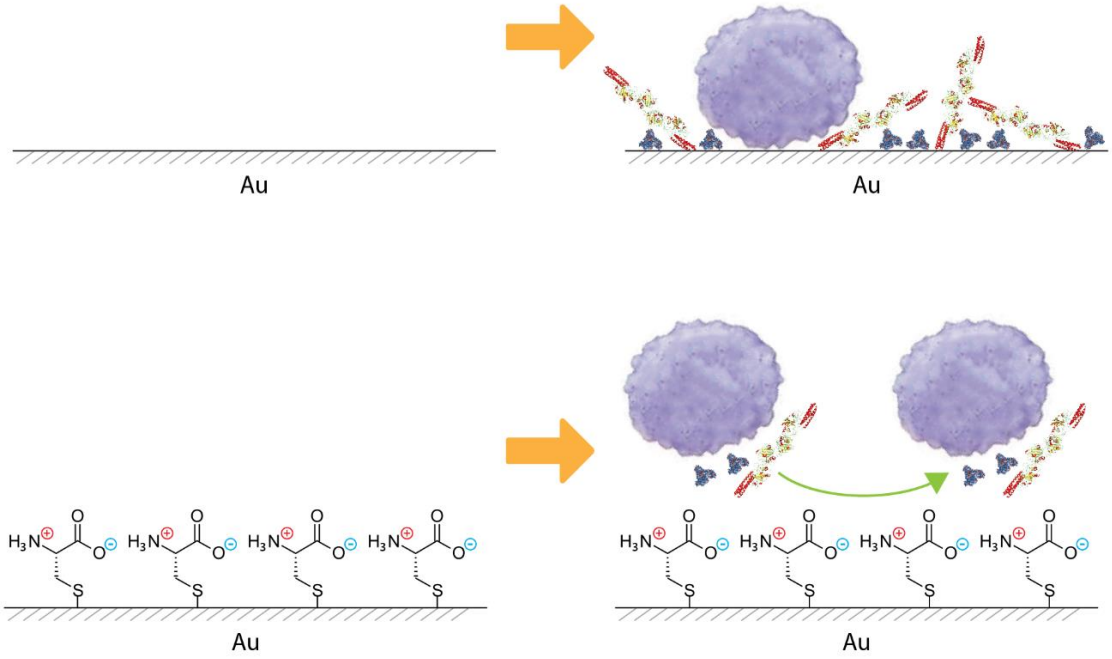

Figure 27: Cartoon illustration of zwitterionic cysteine coating for resisting biofouling.
Results presented in this chapter indicate that a layer of zwitterionic cysteine coating is capable of significantly reducing protein and cellular adsorption.

Although zwitterionic surfaces have demonstrated promising results in resisting nonspecific protein adsorption, the resistive coating is far from universal and often requires designs tailored to the specific

bioelectronic's intended operation conditions. Taking implantable electrotherapeutic devices as an example, the curative electric signal decays proportionally with the thickness of the coating as governed by Coulomb's law; therefore, the thickness of the coating is critical to the performance of the device. Results from Chapter 3 and 5 demonstrate that cysteine is a promising zwitterionic candidate for coating these devices due to its inherent zwitterionic nature, small size, and established thiol chemistry. Through self-assembly, the sulfhydryl group on cysteine allows for easy fabrication of a monolayer on gold surfaces, whereas, the small molecular structure ensure that the curative signal is significantly more effective than devices coated with conventional polymer brush. Cysteine also exists naturally in our body as an amino acid and thus, has high inherent biocompatibility. Recent studies have shown that cysteine as a coating material is capable of stabilizing both silicon and gold nanoparticles in protein solutions with minimal protein adsorption[117, 141].

Chapter 3 had demonstrated that a layer of highly zwitterionic cysteine coating is capable of significantly reducing BSA and sheep serum protein adsorption compared to an untreated gold surface[174]. This work further investigates the feasibility of cysteine as an anti-fouling coating by applying analytical tools with a higher level of precision in conjunction with a wider variety of biological solutions. This chapter demonstrates the fabrication of 1 monolayer of cysteine through solution chemistry. The antifouling performance of cysteine surfaces was evaluated in bovine serum albumin (BSA), fibrinogen, and human blood by quartz crystal microbalance (QCM). The cysteine surface demonstrated over 90% reduction to the adsorption of all three biological solutions compared to untreated gold surfaces. The surfaces were imaged with scanning electron microscopy (SEM) and cellular adsorption was not observed on the cysteine surface, but was prominent on the gold surface. These findings suggest that a zwitterionic cysteine surface is capable of resisting the adsorption of key proteins in the signaling cascade for

inflammatory cells. Surface plasmon resonance imaging (SPRi) was used to complement the results of the QCM.

6.3 Material and Method

6.3.1 Materials

L-cysteine ($HSCH_2CH(NH_2)(CO_2H)$, 97% purity), bovine serum albumin (BSA), and Fibrinogen from human plasma (Fg) were used as received from Sigma-Aldrich. Undiluted human whole blood in BD Vacutainer plastic tube coated with 7.2mg of K2 EDTA was provided by National Taiwan University Hospital (NTUH). Phosphate buffered saline (PBS) was purchased from Invitrogen and Sigma-Aldrich.

6.3.2 Quartz-Crystal Microbalance

The QCM measurements were performed at room temperature with the AT-cut quartz crystal from ANT technology Co., Ltd. Frequency shift (ΔF) was detected by the Affinity Detection System (ADS) type QCM instrument from the same manufacturer. The frequency of the loaded crystal (f_0) was 8.97MHz with a standard deviation of 0.026%. The piezoelectrically active crystal area and reaction chamber volume is $0.1cm^2$ and 30 μL respectively, given by the manufacturer. For all QCM analyses conducted in this study, the samples were first allowed ample time to establish a stable baseline under a continuous flow of phosphate buffered saline (PBS) before a biological solution was introduced to the system. The time required to establish a steady baseline varied among samples, and only the portion of data directly preceding the introduction of a biological solution was presented in the figures to allow for easy viewing of the data. The baseline was considered stable when the change in resonance frequency fell within the machine's inherent signal drift given by the manufacture as ±0.3 Hz per minute. The signal drift, which is considered as a background noise, was removed from the data using a calibration process provided by the manufacture's signal acquisition software. After exposing the sample surface to a

biological solution for the desired amount of time, a PBS solution was again flowed across the sample surface and the resonance frequency was allowed time to stabilize. The change in frequency, ΔF, was calculated by subtracting the frequency of PBS baseline from PBS wash. The flow speed was kept at 30µL/min. Cysteine coated surfaces were fabricated by introducing a 0.1mM L-cysteine solution to the gold portion of QCM chip and allowed to react overnight in accordance with our previous work[174].

6.3.3 Surface Plasma Resonance Imaging (SPRi)

Trapezoidal cyclic olefin copolymer (COC) prisms (n = 1.51) were designed and fabricated with precise angles and dimensions by injection molding at Silitech Technology Co, Inc. A 47 nm gold film was deposited onto the prism using a radio-frequency (13.56 MHz) sputtering system at a working pressure of approximately 3×10^{-3} Torr. Double-sided adhesive (F9460PC, 3M, USA) was cut with a laser machine and used to join the prism to the sample holder.

The SPRi system was an in-house custom-made model designed for real-time monitoring of reflectivity changes based upon the Kretschmann configuration. The optical module consisted of a 1W 850 nm near-infrared (NIR) LED, an achromatic doublet, and a polarizer that provided a p-polarized collimated beam for irradiating the surface of the 47nm gold film on the prism. The light was coupled using a COC prism to generate a surface plasmon resonance and was reflected onto a CCD camera connected to a computer through an IEEE 1394 interface. The incident angle of the light source was manually adjusted so that the value of the reflective intensity was one-third of the difference between the maximum and the minimum reflection. The reflected light was detected by a 12-bit grayscale CCD camera. The abovementioned SPRi subsystems were controlled by a program developed in-house using LabVIEW 8.2. Additional information on this custom-made SPRi system can be found in our previously published paper[245]. A liquid injection system was used to first introduce a PBS buffer to the SPR prism in order to acquire a steady baseline before exposing the surfaces to the biological analyte and followed by a PBS buffer wash. The

change in reflective intensity (ΔRU) was calculated by subtracting the signal of the PBS baseline from that of the post reaction PBS wash. The SPR measurements were completed under zero-flow and, to prevent any dilution effects, at least 3 mL of each solution was injected to flush out the reaction chamber (30 µL).

6.3.4 Scanning Electron Microscopy Characterization

A field emission scanning electron microscope (FE-SEM, Zeiss Leo 1550) was used for the scanning electron microscopy (SEM) analysis. The electron gun energy was kept at 10.00kV and the vacuum was kept approximately at $6x10^{-6}$ mbar. The samples were subjected to SEM analysis without any additional sample preparation.

6.4 Results and Discussion

Upon surgical insertion of any implantable bioelectronics, the body spontaneously smears the device surface with a layer of plasma and tissue fluid proteins to identify the device as foreign and attempts to destroy or isolate the implant. The nonspecifically adsorbed proteins interact with adhesion receptors on inflammatory cells and trigger a cascade of inflammatory responses that is typical of a foreign body response. By minimizing the amount of nonspecific protein adsorption, the degree of undesirable host response can be controlled, thus prolonging the in-vivo functionality of the implant. Preliminary work presented in Chapter 3 demonstrated that a layer of highly zwitterionic cysteine coating can significantly reduce BSA and sheep serum protein adsorption compared to an untreated gold surface. This chapter further investigates the feasibility of cysteine as an anti-fouling coating by incorporating analytical tools with a higher level of precision in conjunction with a wider variety of biological solutions. The amounts of bovine serum albumin (BSA), fibrinogen (Fib), and human blood sample (HBS) adsorbed onto

cysteine surfaces are quantified by a dynamic quartz crystal microbalance and compared with that of untreated gold surfaces.

6.4.1 QCM Calibration

Detection of trace amounts of protein adsorbed onto antifouling surfaces is often difficult and requires extremely sensitive instruments. For this study, a quartz crystal microbalance was selected as the preferred method of measuring surface fouling because this instrument is capable of translating a change in resonant frequency directly to a change in adsorbed mass. This section discusses the calibration employed for this translation and explains all artifacts created as a result of the experimental procedure. When one face of the quartz crystal resonator is in contact with a liquid, the change in frequency (ΔF) can be expressed by Equation 4[234-236],

$$F = -\frac{2f_0^2}{A\sqrt{\rho_q \mu_q}} m - \frac{f_0^{3/2}}{\sqrt{\pi \rho_q \mu_q}} (\eta_L \rho_L)^{1/2}$$

$$\Delta F = -\frac{2f_0^2}{A\sqrt{\rho_q \mu_q}} \Delta m - \frac{f_0^{3/2}}{\sqrt{\pi \rho_q \mu_q}} \Delta (\eta_L \rho_L)^{1/2}$$

Equation 4
$$\boldsymbol{\Delta F = -C_1 \Delta m - C_2 \Delta (\eta_L \rho_L)^{1/2}}$$

Where ρ_q is the density of quartz crystal (2.648 g·cm^{-3}), μ_q is the shear modulus of quartz (2.947x10^{11} g·cm^{-1}·s^{-2}), f_0 is the frequency of the loaded crystal, A is the piezoelectrically active crystal area (given by the manufacturer as 0.1 cm^2), Δm is the change in mass, η_L is the viscosity of the liquid and ρ_L is the density of the liquid. From Equation 4, the resonance frequency can be disturbed by either a change in surface mass (caused by film deposition or decay), a change in viscosity of the liquid, or a change in density of the liquid. If the change to resonator mass is assumed to be zero, thus ignoring the first term of Equation 4, the equation provides information on the change of resonance frequency when the system is disturbed from a gaseous interface to a liquid interface. Taking a crystal with a load frequency (f_0) of

8.96MHz as an example, when the crystal interface transforms from a vacuum interface to a pure water interface, the resonance frequency is expected to decrease by approximately $-1715Hz$ (calculated using Equation 4 at 20ºC and assuming zero change in mass). On the reverse, if a gas bubble is introduced to a liquid-crystal interface, an increase in resonance frequency is expected. This phenomenon was observed on some graphs presented in this QCM study when small gaseous bubbles were introduced to the liquid interface amidst the exchange between different solutions. These gaseous bubbles created temporary spikes in resonance frequency as the bubbles traveled across the liquid-crystal interface.

Operating the QCM under stable conditions, where the change in root product of viscosity and density of the liquid ($\Delta\sqrt{\eta_L\rho_L}$) is negligible, the change in frequency directly reflects the change in surface adsorbents. Therefore, the addition or removal of mass on the surface of the crystal resonator is proportional to the change in resonance frequency by the intrinsic constant C_1 (i.e. $\Delta F = -C_1\Delta m$). Since the intrinsic frequency of the loaded quartz crystal (f_0) varies slightly between each chipset, variation between the intrinsic constants (C_1) of each chip was also expected. However, the variance is very low (0.026%) for the chipsets used in this study and deposited mass can be related to the resonate frequency by:

Equation 5 $$\boldsymbol{\Delta m\ (ng) = -0.549 \pm 0.00030 \Delta F (Hz)}$$

The change in resonance frequency was continuously monitored and recorded in real-time. The QCM figures are composed of three portions (PBS baseline, exposure, and PBS wash) and the portions are separated by dotted red lines. ΔF is calculated by subtracting the stable frequency value acquired during PBS baseline from that acquired during PBS wash; therefore, the wash procedures employ the same buffer solution as that used during the baseline in order to mimic the exact experimental conditions for

accurate calculation. Any biological substances that are weakly adhered on the surface would have also been removed during the post exposure PBS wash.

The flow speed was temporary increased when switching between solutions in order to prevent a splash-over effect by ensuring that the new solution was introduced to the sample surface as soon as possible. If the flow speed was not increased, the newly introduced biomolecules would have been given enough time to diffuse into the previously introduced buffer solution in the machine tubing and create an unnecessary concentration gradient. The necessity of increased flow speed combined with the introduction of small air bubbles oftentimes created significant spikes and/or dips in frequency readings that shortly follows the introduction of a new solution. These artifacts of the experimental procedure resolve themselves and the samples were always allowed ample amount of time to return to a steady reading.

6.4.2 Monolayer Fabrication

For any bioelectrical devices for application in electrotherapy, the curative electrical pulse decays proportionally with respect to the working distance as governed by Coulomb's law. Therefore, fabricating a thin monolayer is essential to avoid hindering the underlying function of these devices. A quartz crystal microbalance (QCM) was used to monitor the monolayer fabrication overnight as well as determine the final coating thickness. Cysteine SAMs were fabricated by coating L-cysteine onto the gold portion of a QCM chipset in accordance with previous work presented in Chapter 3[174] and the reaction was monitored overnight under a continuous flow (Figure 28). In the same study, it was demonstrated that the resulting cysteine surfaces are highly zwitterionic (87.8%) through X-ray photoelectron spectroscopy. The system was allowed ample time to establish a steady baseline under a continuous flow of PBS before the cysteine solution was introduced. For easier visualization of this large set of data, Figure 28 incorporates two modifications to the x-axis. Firstly, only the last 5 minutes of the stable PBS baseline is shown as

additional data points cluster the figure and do not contribute any new information. Secondly, only the initial 3 hours of the overnight reaction is shown in order to preserve the adsorption trend; after 3 hours of exposure, the change in frequency plateaus and additional changes are very gradual with the exception of spikes caused by the introduction of air bubbles. Subsequent to the overnight reaction, a PBS wash was employed to remove any physisorbed layers of cysteine. The PBS wash portion of the figure illustrates the signal approaching a plateau after 60 minutes, indicating that most of the secondary layer are removed; however, the data trend suggests that lengthening the PBS wash step will remove additional physisorbed molecules. Indeed, almost 12 hours are required to completely remove all the physisorbed molecules. The dip in signal observed when switching from the PBS to cysteine solution is the result of an artifact of the experimental process. The total change in frequency, calculated by subtracting the reading during PBS baseline from the plateau portion of PBS wash, is -19.75 Hz which translates to 10.84 ng of cysteine adsorption in accordance with Equation 5. The average adsorbed cysteine is 11.01 ± 1.34 ng (N=9). A typical Au[111] surface is reported to have $4.5x10^{14}$ adsorption sites/cm^2 when maximum coverage is obtained[246, 247] or 9.05 ng of cysteine on a 0.1 cm^2 gold surface. Based on these findings, the fabricated cysteine surfaces have a complete coverage and the average thickness is 1.22 monolayer. An upright cysteine molecule adsorbed through the sulfur group onto a gold surface is reported to have a height of 7.1Å[215-217]; a 1.22 monolayer coating would translate to an average coating thickness of 8.64 Å.

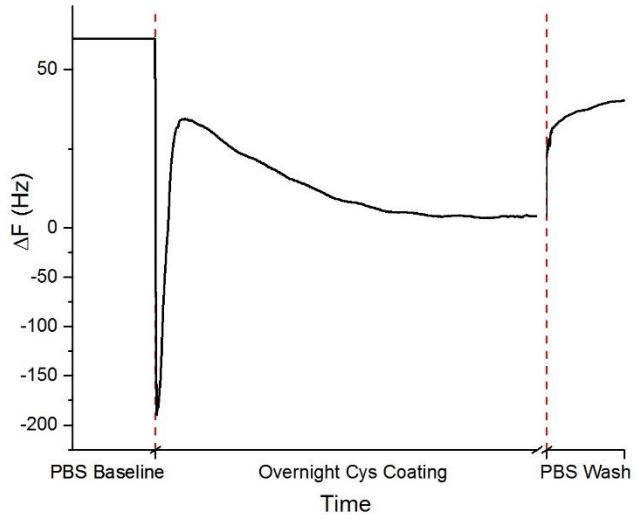

Figure 28: Fabrication of a cysteine surface.
For ease of data visualization, this figure only incorporates data from the last 5 minutes of PBS baseline, initial 3 hours of thiol reaction, and 60 minutes of post-exposure PBS wash. The x-axis is rescaled for the PBS portions to preserve the data trend. ΔF of $-19.75 Hz$ was observed, translating to 10.84 ng cysteine adsorption or 1.20 monolayer of coating thickness.

6.4.3 Biological Fouling

The *in-vivo* performance of any bioelectronics is greatly hindered by nonspecific adsorption of plasma and tissue fluid proteins. This study employs a dynamic QCM to investigate the antifouling property of cysteine SAMs in common protein solutions such as bovine serum albumin (BSA) and fibrinogen (Fg) as well as in complex biological medium such as whole human blood. Untreated gold surfaces were used as the control in this study.

BSA was selected as a model protein for assessing nonspecific fouling primarily because the characteristics of BSA, such as size, charge, and amino acid sequence, are well understood[153, 154] and this protein closely resembles human serum albumin (HSA), which is the most abundant plasma protein in the blood. Furthermore, a majority of published literature in surface biofouling assess the performance of their coating using BSA (PEG[8], PMMA[77], Poly(TM-SA)[69]); therefore, the extent of BSA adsorption serves as a typical benchmark for easy comparison with other established technologies. Figure 29a

illustrates the change in resonance frequency with respect to time for an untreated gold surface when exposed to a BSA solution. This figure depicts a 30 minute PBS baseline before a 3 hours BSA exposure followed by a PBS wash. The PBS wash was allowed to continue until the signal plateaued, thus ensuring the removal of all weakly adsorbed BSA molecules. ΔF of -147.11Hz was observed, which translates to 80.77ng of BSA fouling onto the untreated gold surface. Figure 29b reports BSA adsorption onto a cysteine surface. This figure depicts a 45 min PBS baseline followed by a 3 hours BSA exposure. The PBS wash was allowed to continue for the same duration of time as what had transpired during the BSA-on-gold experiment. A resulting ΔF of -8.02Hz was observed which translate to 4.40ng of BSA fouling. Compared with the untreated gold surface, the cysteine coated surface was able to reduce BSA fouling by 92.78%. The QCM results agrees with the SEM images (Figure 34a & Figure 34b), where spherical BSA clusters were observed throughout the untreated gold surface whereas these clusters were very rarely observed on the cysteine surface. To further demonstrate the anti-fouling property of zwitterionic cysteine, a 24-hour exposure to BSA was conducted under the same experimental conditions and 8.03ng of BSA fouling was observed on the cysteine coated surface (QCM figure not shown).

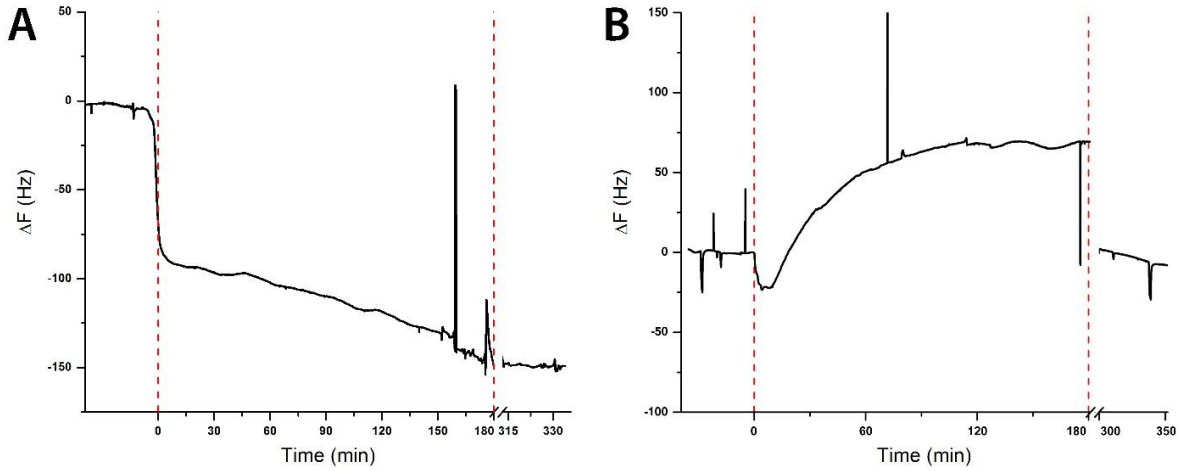

Figure 29: BSA adsorption for 3 hours
A) onto an untreated gold surface and B) a cysteine coated surface. The total amount of BSA fouling was 80.77 ng and 4.40 ng for gold and cysteine surfaces respectively. Compared with the untreated gold surface, the cysteine coated surface was able to reduce BSA fouling by 92.78%.

Fibrinogen (Fg) is one of the primary proteins in the clotting cascade and is widely viewed as a significant determining factor for the longevity of implantable devices[248, 249]. Figure 30a and Figure 30b illustrates the amount of fibrinogen adsorbed onto an untreated gold and a cysteine coated surface, respectively. For the gold surface, the figure depicts a 10 minute PBS baseline followed by 3 hours of fibrinogen exposure. The PBS wash was allowed to continue until the signal plateaued in order to remove any weakly physisorbed fibrinogen. ΔF of -180.59 Hz was observed, which translates to 99.10ng of fibrinogen fouling onto the untreated gold surface. Considering the impressive performance of cysteine in resisting BSA fouling, a more lengthy exposure was conducted for the cysteine surface. Fibrinogen was exposed to the cysteine surface for 14 hours. The PBS wash was allowed to continue for the same duration of time as what had transpired during the Fg-on-gold experiment. For easier visualization of this large set of data, only the initial 10 hours of the exposure is shown. In addition, the x-axis has been rescaled for the PBS baseline and the PBS wash portion of this figure in order to preserve the data trend. A ΔF of -16.56 Hz was observed, which translates to 9.09 ng of fibrinogen fouling onto the cysteine

SAM. Compared with the untreated gold surface, the cysteine coated surface was able to reduce fibrinogen fouling by 90.82%. The QCM results agrees with the SEM images (Figure 35a-d), which reveals large clusters of fibrinogen on the gold surface whereas these clusters are absent on the cysteine surface.

The adsorption of albumin onto both surfaces is initially rapid and, as coverage increases, adsorption begins to slow as proteins have to compete for the fewer free sites. This single step adsorption profile is as expected since albumin is approximately globular in shape and thus, adsorption in any orientation would not alter the packing density. In contrast, the adsorption process for fibrinogen appears to occur in a multistep fashion, where the protein initially adsorbs rapidly in a flat orientation saturating the surface with its long axis parallel to the sample surface. After some time, fibrinogens begin to rearrange into a perpendicular orientation that exposes additional adsorption sites on the surface and allows for additional protein adsorption. This second adsorption step is more gradual compared with the initial step, as expected, since the rearrangement of surface protein is a slow process. A schematic depiction of fibrinogen's multistep adsorption process is shown as the inserts in Figure 30b. The rearrangement of adsorbed fibrinogen and its multistep adsorption profile have been reported in other QCM studies[250, 251] and are believed to be driven by favorable hydrophobic interactions as long axes of fibrinogen become parallel to one another.

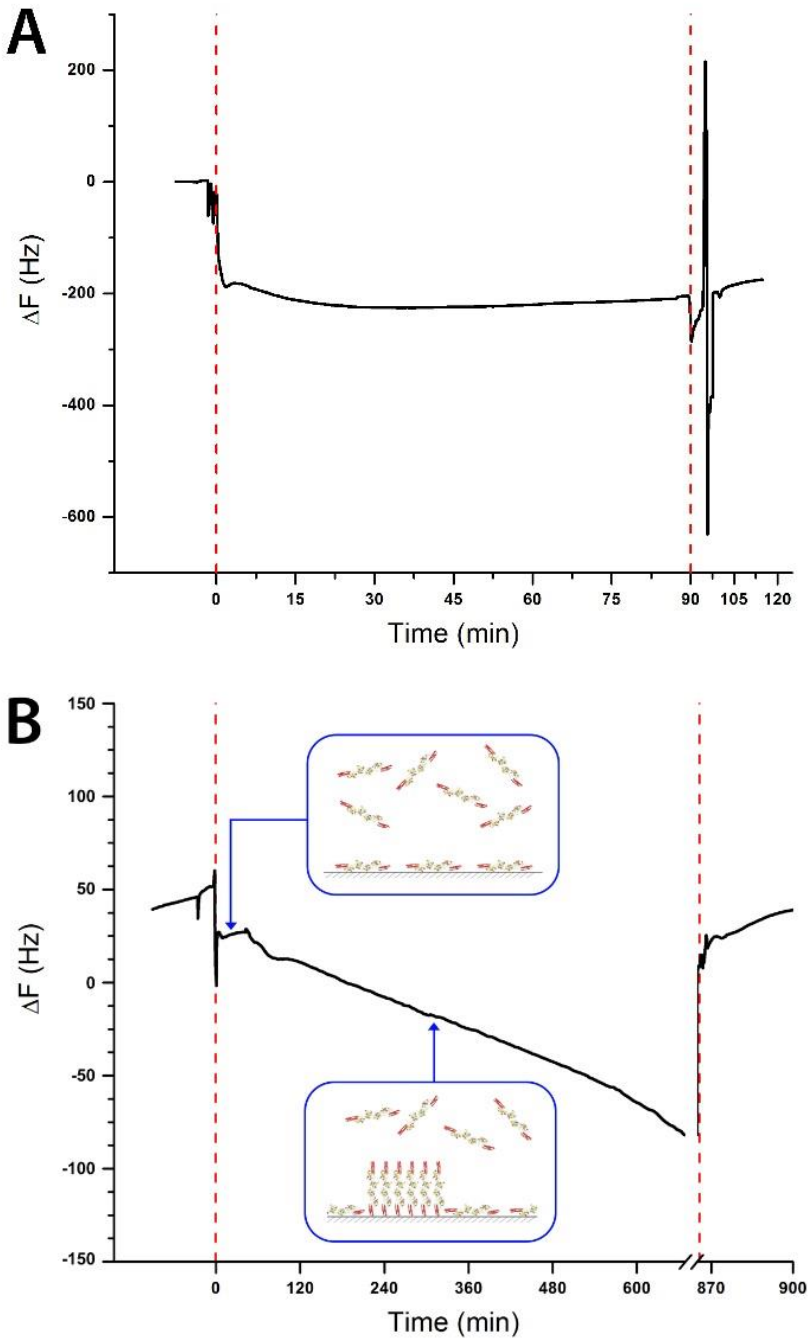

Figure 30: Fibrinogen adsorption
onto an untreated gold surface for 3 hours (panel A) and a cysteine coated surface for 14 hours (panel B). For ease of data visualization, only the initial 10 hours of exposure is displayed for the cysteine surface and the x-axis has been rescaled for the PBS portions in order to preserve the data trend. The total amount of fibrinogen fouling was 99.10 ng and 9.09 ng for gold and cysteine surfaces respectively. Compared with the untreated gold surface, the cysteine coated surface was able to reduce BSA fouling by 90.82%.

The signaling and control of the foreign body response are ultimately achieved through a complex system of adsorbed protein interactions with adhesion receptors on inflammatory cells. The presence of adsorbed proteins such as albumin, fibrinogen, complement, fibronectin, vitronectin and γ globulin, regulate inflammatory cells interactions and adhesion, and thus, are critical determinants of subsequent degradation and isolation cascade[252-255]. To fully investigate this complex interaction, a half diluted human blood sample (50%HBS) was applied to cysteine and gold surfaces. The dilution of HBS was necessary in order for the QCM detector to obtain a proper reading. During experiments involving undiluted HBS, the QCM detector became unresponsive as soon as the surface was exposed to pure HBS. We hypothesize the loss of signal was caused by the high intrinsic viscosity of undiluted human blood (typically 4-5 times greater than water). By exposing the quartz crystal to a solution with high viscosity, a very sudden and sharp change in resonance frequency is expected in accordance with Equation 4, and this sudden change in frequency is believed to be the cause of the signal loss from the QCM detector. Figure 31a and Figure 31b illustrates the adsorption profile of biological substances onto an untreated gold and a cysteine coated surface, respectively. The gold surface was exposed to 50%HBS for one hour followed by a PBS wash that lasted until the signal plateaued. The ΔF was -3012.06 Hz, which translates to 1653.68 ng of biological fouling onto the untreated gold surface. The QCM response for the untreated gold surface is very jagged and exhibits sudden rapid decreases (for example, from 30 to 35 min, and again from 47 min to 53 min), which greatly differs from the smooth and continuous adsorption profile exhibited by homogeneous protein studies presented earlier. This observation indicates a strong case of protein-enhanced adsorption where the presence of specific proteins on a surface induces further adsorption of other proteins and cells through complex biological interactions[256]. Indeed, images captured by the SEM showed ruptured cells throughout the untreated gold surface (Figure 36d).

Considering the impressive performance of cysteine in resisting BSA and fibrinogen fouling, a more lengthy exposure was conducted for the cysteine coated surface. The surface was exposed to 50%HBS for 1.5 hours and the PBS wash was allowed to continue until the signal plateaued. The ΔF was -217.36 Hz, which translates to 119.20ng of biological fouling onto the cysteine surface. Compared with the untreated gold surface, the cysteine coated surface was able to reduce biological fouling by 92.79%. Furthermore, the QCM response for the cysteine surface is very smooth and has leveled off after 300s of exposure. Additional decrease in signal was very gradual and the adsorption trend is very similar to that of the homogeneous protein studies presented earlier. This adsorption profile suggests that the extent of protein-enhanced adsorption is not significant on a cysteine coated surface. SEM images support this observation as there were no indications of adsorbed cells on the cysteine coated surface.

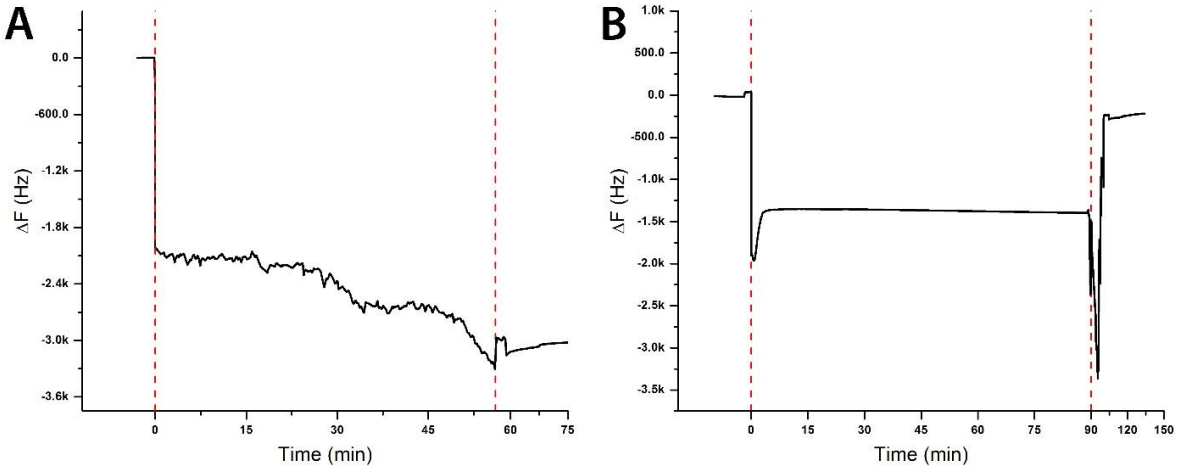

Figure 31: Half-diluted human blood exposure
onto an untreated gold surface for 1 hour (panel A) and a cysteine coated surface for 1.5 hours (panel B). Adsorption data for the untreated gold surface are very jagged and exhibit sudden rapid decreases (from 30 min to 35 min, and from 47 min to 53 min), which greatly differs from the smooth and continuous adsorption profile exhibited by homogeneous protein studies presented earlier. This observation indicates a strong case of protein-enhanced adsorption, which was not observed on the cysteine SAM. The total amount of biological fouling was 1653.28 ng and 119.20 ng for gold and cysteine surfaces respectively.

Table **9** summarizes the results of the QCM study. Compared with recently published nonfouling cysteine coatings, our design outperforms those coatings significantly (44.05 ng/cm^2 BSA fouling as opposed to 66 µg/cm^2 [143], and 5.45% BSA fouling as oppose to 55%[257]). Similarly, our results are comparable to, if not exceed, the performance of recently published nonfouling hydrogel[155], zwitterionic coatings[156, 157, 258], cellulose[259], PEG-based polymer brush[83, 260]. Long-chain zwitterionic polymer brushes that benefit from steric repulsion, the compression force of the polymer chains[12, 13], are known to achieve ultra-low BSA fouling in the <5 ng/cm^2 range. However, for applications in bioelectric devices, a thick polymer brush coating would be detrimental to the device performance, because the curative electrical impulse decays proportionally with respect to the working distance as governed by Coulomb's law. Therefore, our coating is intentionally designed with the criteria of incorporating a small monomer as oppose to thick polymer brushes in order to minimalize interferences with the underlying bioelectronic. The reported cysteine coating is composed of 1.22 monolayer and an average thickness of 8.64 Å. Compared with the ultra-low fouling polymer brushes that have a thickness of 10-15 nm[126], a cysteine-coated electrode will exhibit a stimulation that is 12 to 17 times stronger since the effective electric field is inversely proportional to the distance. Furthermore, the experimental conditions, mainly the protein concentration and exposure time, varies between different groups. Surfaces reported having ultra-low fouling capability are generally exposed at 1 g/L of BSA for 10-15 min[69, 118, 155] whereas, our work was conducted with a concentration of 6.6 g/L and an exposure time of 3 to 24 hours. A higher protein concentration and a longer exposure time are expected to result in a greater degree of surface fouling.

Table 9: Summary of QCM results.
This table summarizes the results presented in section 6.4.3. N = 3 for trials done with replicates.

	ΔF (Hz)	Fouling (ng)	Areal Fouling (ng/cm²)
BSA on Gold	-150.79	82.79	827.86 ± 24.40
BSA on Cys	-7.82	4.30	42.95 ± 6.91
BSA on Cys - 24h	-14.63	8.03	80.30
Fg on Gold	-177.35	97.36	973.64 ± 16.68
Fg on Cys	-11.87	6.51	65.14 ± 12.14
Fg on Cys -14h	-16.56	9.09	90.91
Blood on Gold	-3,012.06	1,653.62	16,536.23
Blood on Cys	-217.36	119.33	1,193.33

6.4.4 Extended Protein Study with SPRi

The SPR analysis was conducted to complement the QCM findings. Compared with the QCM, the SPR instrument was less sensitive to signal distortion caused by ambient vibrations; therefore, results from the SPR study exhibited a higher signal-to-noise ratio. The added stability of the SPR instrument allowed for experiments involving prolonged exposure to protein solutions, which was difficult to monitor using the QCM. A custom-built surface plasmon resonance instrument was used for this study. In brief, an 850±50 nm NIR-LED was used as a light source for excitation. The collimated light beam projects onto the gold surface of a COC prism at an incident angle of approximately 66°. The limit of detection for this instrument was previously determined to be 0.01 nM ml^{-1} with a signal-to-noise ratio of three[245]. The intensity of the reflected light varied with respect to the amount of adsorption onto the measuring surface; therefore, by detecting the changes in the intensity of reflected light (ΔRU), we were able to obtain a measure of total surface fouling onto the prism's gold surface. The SPR software, developed in-house using LabVIEW, averaged all the gray-scale pixels in the region of interest to produce a response unit

(RU). The maximum and minimum signal typically observed in this setup were 2700 RU and 200 RU respectively. The injection of a new solution occasionally created a temporary spike in the SPR response.

Given the successful demonstration of protein resistivity during the QCM study, cysteine coated surfaces were exposed to the protein solutions for a significantly longer period of time compared with the gold control. For exposures to BSA solutions, the SPR response for an untreated gold surface increased by 49.6 RU after 1 hour, whereas that of a cysteine surface was increased by only 8.93 RU after 68 hours (Figure 32a and Figure 32b, respectively). Compared to the gold surface, a cysteine surface exhibited less than 18% BSA after 68 hours. This finding agrees with the findings from the QCM study where a cysteine coated surface exhibited 9.94% BSA fouling after 24 hours compared to an untreated gold surface. For exposures to fibrinogen, a gold surface demonstrated an increase of 439.5R U after 1.5 hours whereas a cysteine surface demonstrated an increase of only 86.5 RU after 36.5 hours (Figure 32c and Figure 32d, respectively). For both cysteine and gold surfaces, the removal of loosely bound fibrinogen during the PBS wash appeared to be more gradual compared with that of BSA. This phenomenon is perhaps best observed by comparing the PBS wash portion of Figure 32b to Figure 32d. The SPR response for BSA exposure (Figure 32b) had rapidly reached a plateau during 40 minutes of PBS wash; however, for Fg exposure (Figure 32d), the response decreased gradually and had yet to reach a plateau after the same amount of time.

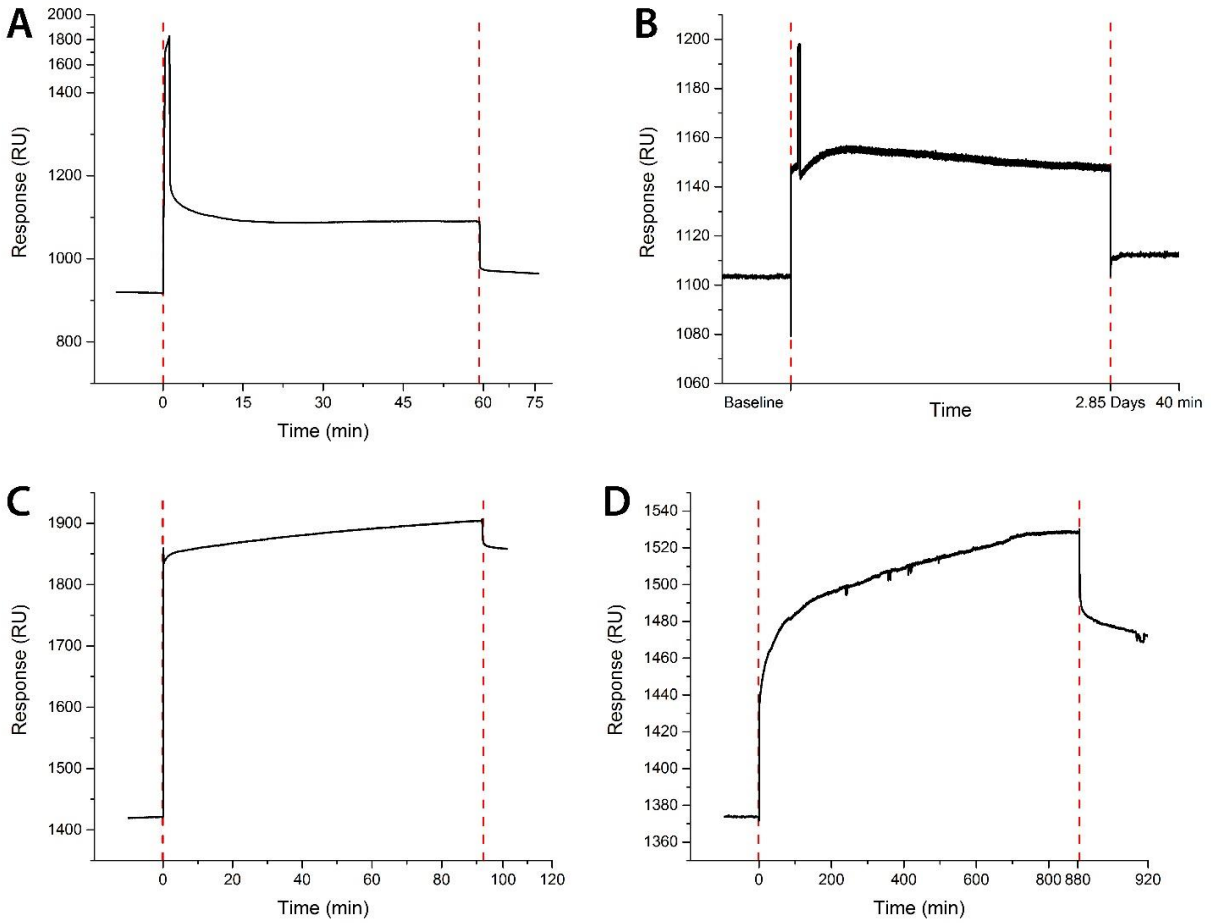

Figure 32: SPR Measurements of BSA and Fg Fouling
Panel A and B illustrate SPR measurements of BSA fouling onto a gold surface and a cysteine surface respectively. Compared with an untreated gold surface, a cysteine coated surface was able to reduce BSA fouling by 82% even after a prolonged exposure. Panel C and D illustrate SPR measurements of Fg fouling onto a gold and cysteine surface respectively. Fg fouling was reduced by 80% even after a prolonged exposure. For both cysteine and gold surfaces, the removal of loosely bounded fibrinogen during the PBS wash appeared to be more gradual compared with that of BSA.

6.4.5 Scanning Electron Microscopy

The purpose of the scanning electron microscopy (SEM) analysis is to provide a qualitative understanding towards the degree of protein fouling in order to complement the quantitative analytical findings presented in earlier sections of this article. By visually inspecting each surface, we can acquire information regarding important features such as surface morphology, topological information, as well

as localized protein aggregation. The performance of cysteine coated surfaces in resisting BSA, fibrinogen, and human blood is compared with that of untreated gold surfaces. The native gold surfaces refer to the analytical portion that came with the QCM chipsets and characterized as is, whereas cysteine surfaces were fabricated by exposing a cysteine solution to the native gold portion of the QCM chipset (refer to Materials and Method). Figure 33a illustrates the untreated gold surface on a QCM chipset prior to any exposure to organic solution. This figure is taken over a large area (389 μm by 258 μm) and reveals a continuous surface with a similar level of roughness throughout the sample. Figure 33c provides a zoomed-in image of the gold surface, revealing the characteristic large grain size that is common to these surfaces. Figure 33b, taken over the same dimension as Figure 33a, illustrates a cysteine surface that was fabricated by exposing the native gold chipset to cysteine solution through QCM. Similar to its gold counterpart, the cysteine sample exhibits a continuous surface; however, much of the surface roughness was not observed. Indeed, a zoomed-in image of the cysteine surface, Figure 33d, reveals that much of the grain size are absent, although deeper crevices are still observable.

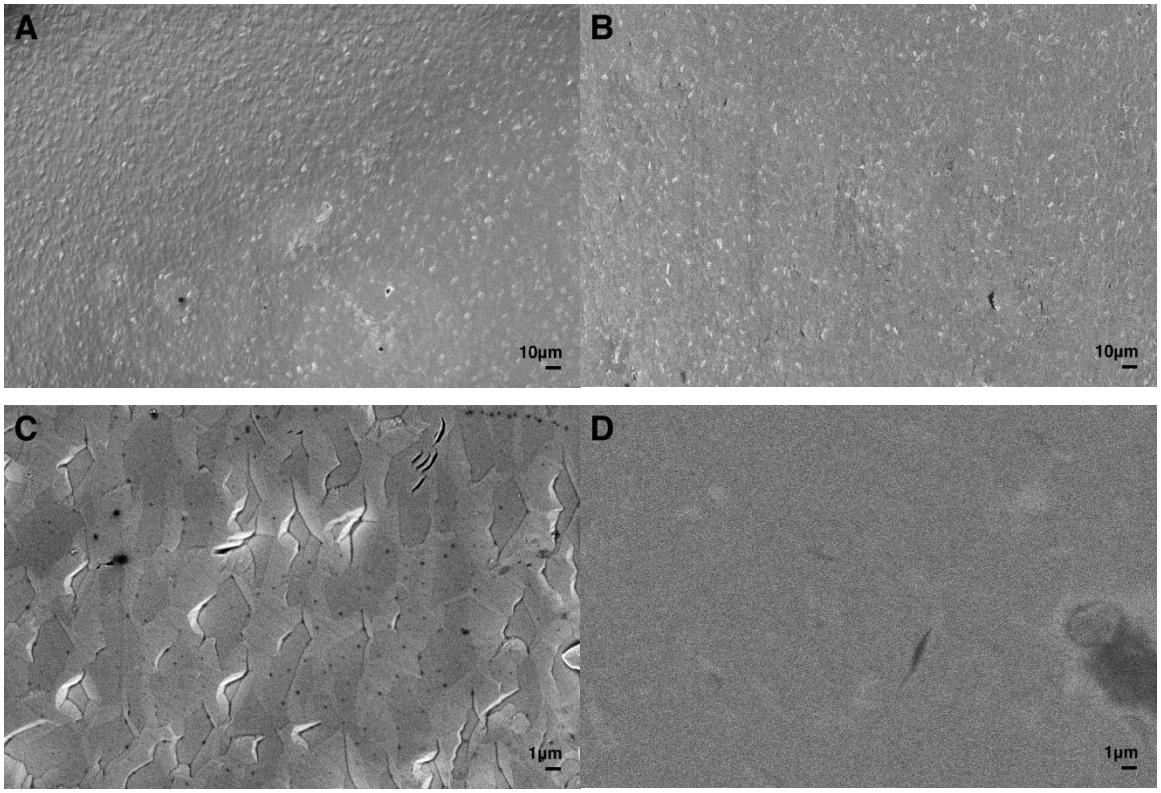

Figure 33: SEM images of gold and cysteine surfaces before exposure to biological solutions
Panels A and B illustrates the wide view of, respectively, untreated gold and cysteine surface prior to exposure to organic solution. Images demonstrate continuous surfaces without large defects. Panel C and D illustrates the magnified images of, respectively, untreated gold and cysteine surface. The characteristic grain size of gold can be clearly seen in panel C, but disappears after the coating as shown in panel D.

Figure 34a and Figure 34b illustrates BSA adsorption onto gold and cysteine surfaces, respectively, taken over a wide imaging area in order to better provide a non-localized depiction of the surfaces. On both surfaces, BSA adsorption appears to be sparse, which is in agreement with the QCM findings, and the distribution of protein is uniform. It is important to note that even though the cysteine surface depicts many white dots, which are often indications of protein clusters, these dots are actually inorganic crystals as revealed by Figure 34c and Figure 34d. The organic crystals illustrated in these zoomed-in images are postulated to originate from salts in the PBS solvent as a result of the drying process and are not to be

mistaken as protein deposits. A SEM image of a characteristic spherical BSA cluster is provided in the Appendix (Supplementary Figure S4).

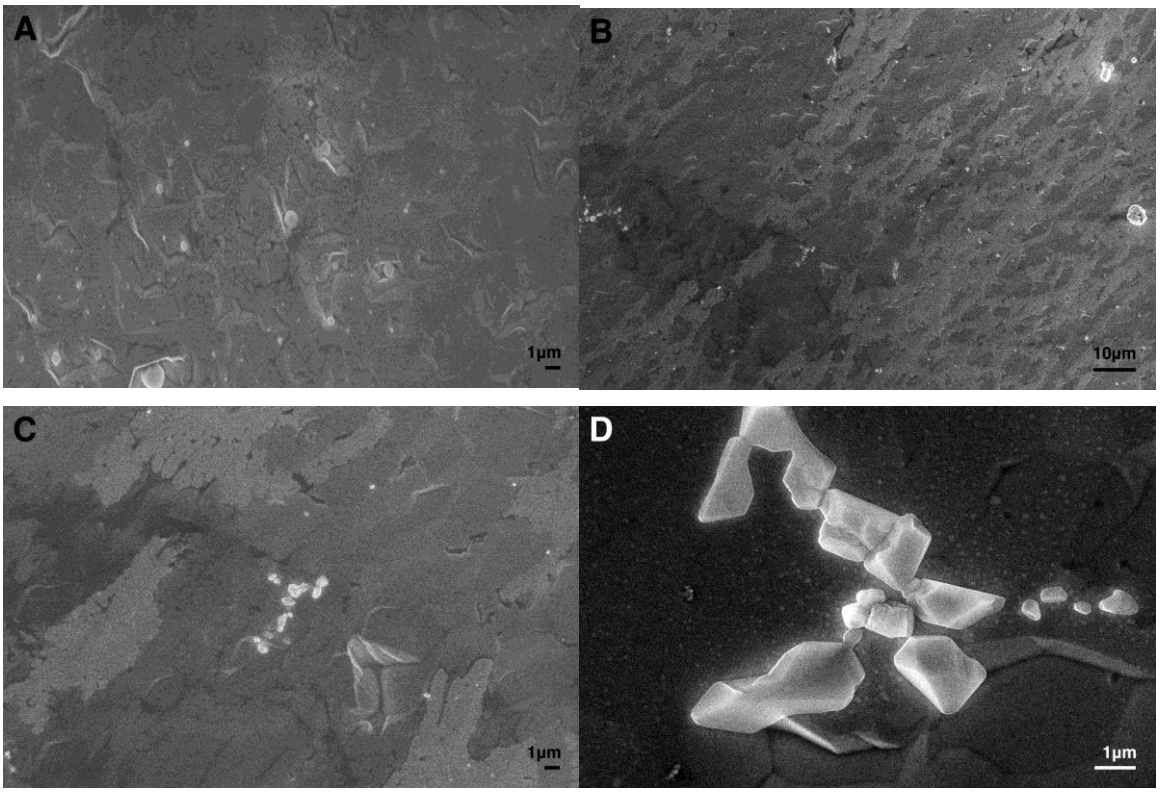

Figure 34: SEM images of gold and cysteine surfaces after exposure to BSA solution
SEM images of BSA adsorption onto untreated gold (panel A) and cysteine surface (panel B to D). BSA adsorption on the gold surface appears in the form of characteristic spherical aggregates. BSA adsorption onto the cysteine surface is sparse and as illustrated by panel C and D, the majority of surface adsorbates are actually salt crystals that are artifacts of the drying process.

Figure 35a and Figure 35b illustrates fibrinogen adsorption onto gold and cysteine surfaces, respectively, taken over a wide imaging area in order to better provide a non-localized depiction of the surfaces. Comparing these two images, the gold surface clearly exhibits a larger amount of deposits than the cysteine surface, which is in agreement with the QCM findings. In fact, fibrinogen adsorption onto the cysteine surface was observed very infrequently and in similar degree as the BSA adsorption. Closer inspections of the deposits on the gold surface reveal salt crystals that encapsulate protein clusters (Figure

35c). We postulate that this phenomenon was caused during the drying process where salt in the PBS solution crystallizes around the adsorbed protein, thus encapsulating the smaller protein clusters. A large fibrinogen cluster is illustrated in Figure 35d.

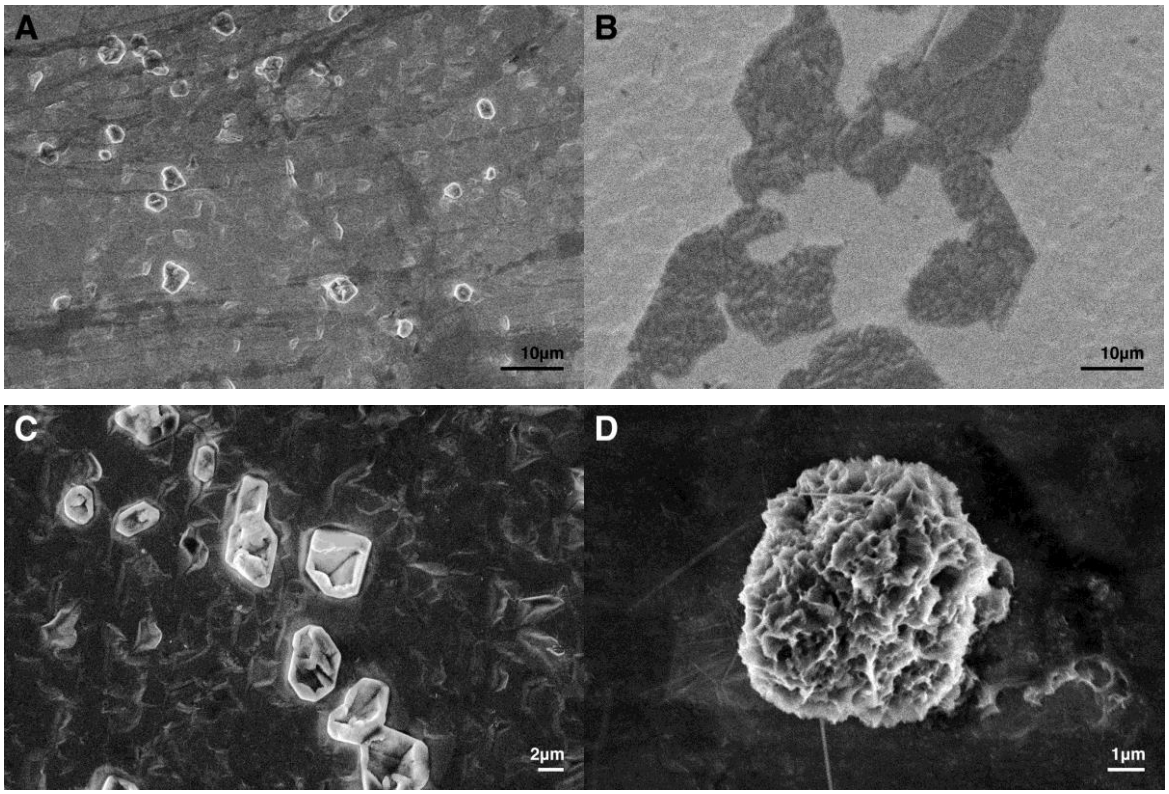

Figure 35: SEM images of gold and cysteine surfaces after exposure to fibrinogen solution.
Fibrinogen adsorption onto an untreated gold surface (panels A, C, and D) occurred as large clusters (panel D) and salt crystals with encapsulated protein clusters (panel C) are common. Only a small degree of fibrinogen adsorption was observed on the cysteine surface (panel B).

Figure 36a and Figure 36b respectively illustrates cysteine and gold surfaces subsequent to blood exposure. These images were taken over a wide area in order to better provide a global depiction of the surfaces. Similar to previous observations, a cysteine surface demonstrated a significant improvement over a native gold surface in resisting adsorption. Large chunks of deposits can be identified throughout the gold surface even under low magnifications, whereas deposits can only be observed under high magnifications on the cysteine surface (Figure 36c). It is unclear from the SEM analysis whether these

clusters on the cysteine surface are proteins or salt crystals due to the irregular shapes and sizes; it is entirely possible that these clusters are composed of both entities similar to what was observed in Figure 35c. Remnants of cells, Figure 36d, were observed throughout the gold surface in the size range of 8-10 µm, which is comparable to red blood cells at 6-8 µm and white blood cells at 12-15 µm. Cellular adsorption was not observed on the cysteine sample.

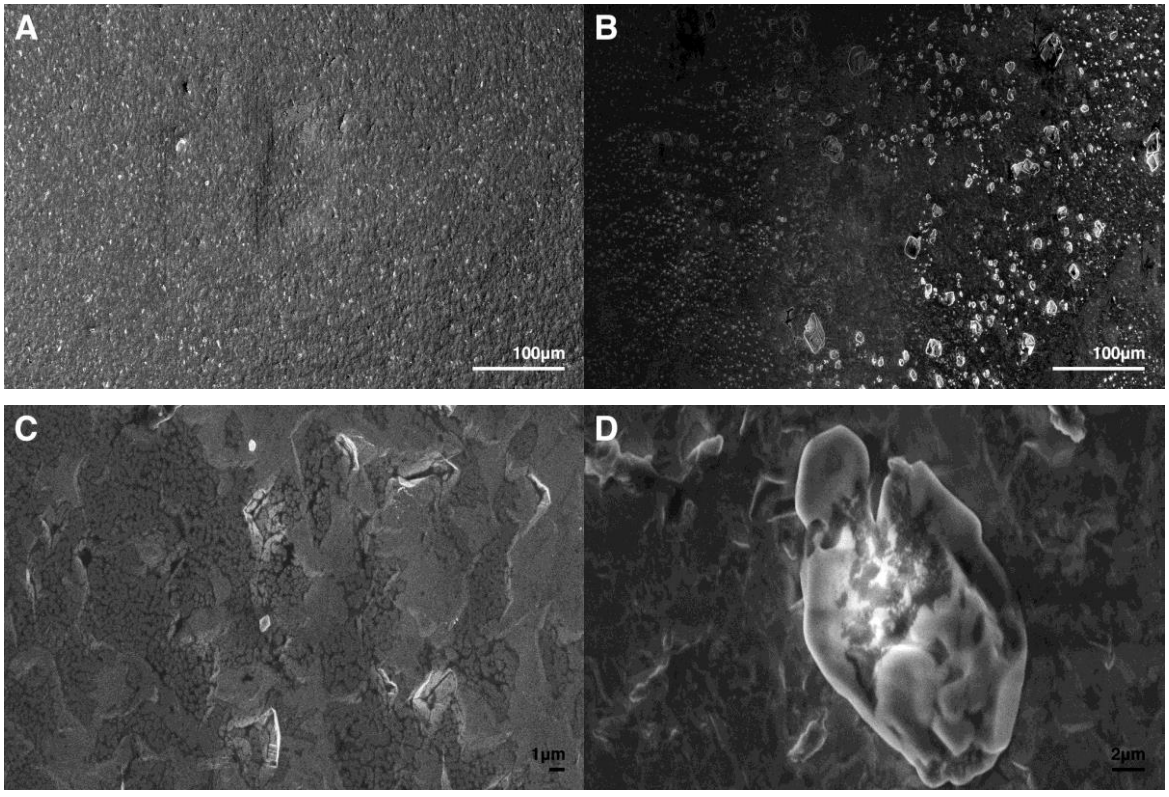

Figure 36: SEM images of gold and cysteine surfaces after exposure to diluted human blood
SEM images of cysteine (panel A) and gold (panel B) surface after exposure to human blood. Large chunks of deposits can be identified throughout the gold surface, whereas deposits can only be observed under high magnifications on the cysteine surface. Cellular adsorption, as shown in panel D, was commonly observed on the gold surface, but not observed on the cysteine surface (panel C).

6.5 Conclusion

Herein we have demonstrated the successful fabrication of zwitterionic cysteine surfaces through thiol chemistry on gold substrates in a solution. The reaction was monitored and recorded in real time by a quartz crystal microbalance, which returned a coating thickness of 1.22 monolayer or 8.64Å after one hour of post reaction wash. The removal of the entire secondary layer can be achieved by extending the post reaction wash to 12 hours. QCM was also used to measure the real-time adsorption of various proteins onto both cysteine-coated and untreated gold surfaces in order to provide effective comparisons. The cysteine surface was able to reduce bovine serum albumin, fibrinogen, and half-diluted human blood fouling by 94.55%, 90.82%, and 93.80% respectively compared to an untreated gold surface. BSA fouling onto a cysteine surface was minimized to 44ng/cm^2 after 3 hours of exposure, which is a significant improvement compared with other published cysteine coatings. SEM imaging was performed to complement the finds of QCM analysis and the results from the two characterization techniques are in agreeance. For samples exposed to human blood, cellular adsorption was observed by both the SEM and QCM for the untreated surface, but was not observed on the cysteine surface. These findings confirm that cysteine, due to its thin coating thickness, zwitterionic nature, and stability *in-vivo*, is a promising candidate for replacing the conventional PEG-based material for improving long-term biofunctionality of implantable bioelectronics.

Chapter 7
Conclusions and Future Work

7.1 Summary

This thesis presents new findings in the field of self-assembled monolayers, antifouling, zwitterionic materials, and chemical engineering. Cysteine SAMs hold tremendous potential as protein-resistant coatings for implantable bioelectronics due to their intrinsic biocompatibility, zwitterionic nature, and thin coating thickness. Zwitterionic surfaces are capable of resisting protein fouling by forming a strong hydration layer that is energetically unfavorable for adsorption and these surfaces are known to be superior to traditional hydrophilic coatings. The research presented here demonstrates that cysteine, existing as a zwitterion under physiological conditions, can form a highly zwitterionic surface by controlling the self-assembly reaction. Additionally, the coating created by a monolayer of cysteine is extremely thin and analysis concluded a coating thickness of less than one nanometer. The coating thickness is extremely important for electrotherapeutic bioelectronics where the curative electrical signal decays proportionally with respect to surface distance. Finally, a monolayer of highly zwitterionic cysteine demonstrated a strong resistance to biological fouling by significantly reducing the adsorption of serum albumin, fibrinogen, and human blood. This thesis produced promising results for synthesizing a zwitterionic antifouling coating composed of a cysteine SAM as an alternative to traditional hydrophilic polymer brushes that often are not biocompatible and hinder the underlying bioelectronics.

7.2 Conclusions

Cysteine self-assembled monolayers can be synthesized by anchoring the sulfur group onto a gold surface through thiol chemistry in solution. The surface coverage, coating thickness, and zwitterionic

percentage can be directly controlled by reaction time and temperature. Increasing reaction time allows anchored cysteine molecules to reorient themselves in order to free up additional adsorption sites on the gold substrate to accommodate additional cysteine adsorption, thus achieving a higher surface coverage. Using a quartz crystal microbalance (QCM) to monitor the adsorption of cysteine onto a gold substrate in real-time, over 99% surface coverage was observed after 3 hours of reaction in a 0.1mM solution of L-cysteine. The thickness of cysteine coatings was analyzed using QCM and ellipsometry. A monolayer coating was determined to be less than 1 nanometer in thickness. The adsorption kinetics can be described by Langmuir adsorption isotherm and experimental data were fitted using both OriginPro and MatLab. The dissociation constant is negligible as expected from the strong thiol-on-gold bond.

Increasing reaction temperature to 330K allows a higher percentage of the surface to be in the preferred zwitterionic state by releasing the amine groups that are anchored onto the gold substrate through a reconfiguration of the cysteine-gold bonds. X-ray photoelectron spectroscopy (XPS) was employed to analyze the carbon (C1s), nitrogen (N1s), and sulfur (S2p) emission lines. Results indicate that 80.53% of the cysteine SAM is zwitterionic for samples created at room temperature and this zwitterionic fraction is increased to 94.5% for SAMs created at 330K. Irradiation damage to the SAMs, caused by prolonged exposure to photoelectrons during the XPS analysis, was observed in the form of C-S bond cleaving and produces atomic sulfur that either remains on the gold substrate or redeposits back onto a neighboring molecule.

The antifouling performance of zwitterionic cysteine SAM towards homogeneous protein solutions and complex biological media were evaluated using bicinchoninic acid (BCA) protein assay, surface plasmon resonance imaging (SPRi) and QCM. Compared to untreated gold surfaces, the cysteine coating demonstrated 95% reduction to BSA adsorption after 3 hours and 90% reduction after 24 hours. Similarly, the surface demonstrated over 90% reduction in the adsorption of fibrinogen as well as human blood.

Cellular adsorption was prominent on the untreated gold surface, but was not observed on the cysteine surface as confirmed by scanning electron microscopy (SEM). This finding suggests that a zwitterionic cysteine surface is capable of resisting key proteins in the blood that are responsible in the signaling cascade for inflammatory cells.

Overall, cysteine is an excellent antifouling material for prolonging the *in-vivo* lifetime of implantable bioelectronics. By reducing nonspecific protein adsorption *in-vitro*, cysteine coatings demonstrated the potential to control or delay undesirable host responses that are detrimental to the device functionality. Assessing the performance of cysteine coatings *in-vivo* is the logical next-step.

7.3 Future Work

1. The interaction between adsorbed proteins and adhesion receptors on inflammatory cells accounts for the primary cellular recognition system. Proteins such as albumin, fibrinogen, complement, fibronectin, vitronectin and γ globulin, regulate the adhesion of inflammatory cells and are critical determinants of subsequent degradation and isolation cascade. Therefore, it is beneficial to understand whether cysteine coatings exhibit an affinity towards any specific protein(s) inside the body. Enzyme-linked immunosorbent assay (ELISA) is one of the tools that can be used to identify and quantify the adsorbed plasma proteins.

2. Adsorbed proteins can slowly denature over time and the denatured proteins are known to promote immunological recognition of the underlying material that would otherwise remain “stealthy”. Therefore, the integrity of adsorbed protein is also of significant interest. The nature of adsorbed proteins and their denaturation are perhaps best investigated through molecular simulations as detecting the denaturation of adsorbed proteins from a complex biological solution is extremely

difficult. Oftentimes, the analytical test itself will be responsible for the denaturation of adsorbed protein.

3. Protein adsorption is proven to be a dynamic phenomenon, where highly mobile proteins will initially adsorb onto the surface, but are later replaced by other proteins through a complex series of protein exchange mechanisms. If the "later adsorbed" proteins are responsible for promoting undesirable host responses, it might be beneficial to "tune" the cysteine coatings to exhibit a higher affinity towards the initially adsorbed proteins in hopes to prevent further protein exchange. This tuning of the coating will be the first step towards controlling undesirable host responses as oppose to simply delaying it through reducing all fouling. Identifying adsorbed plasma proteins and understanding the protein exchange mechanisms will be crucial in accomplishing this work.

4. Determine the effect of cysteine coatings on underlying electrotherapeutic devices. The conductivity of the coated surface can be tested by a four-point probe and conductive atomic force microscopy (C-AFM). This study can provide valuable information on the correlation between coating thickness and degree of interference that cysteine coatings have on the electric signal.

5. Animal studies of cysteine SAMs are the logical next-step for confirming the feasibility of cysteine as an antifouling material and should proceed with a rat model. Histopathological examination of the subcutaneous tissue surrounding the implant should be carried out at different intervals to identify the various stages of the inflammatory phase. Some key observations include identifying neutrophils that are prominent in the initial acute inflammatory phase, a dense network of fibrous tissue with lymphocytes and macrophages characteristic of the chronic inflammatory phase, and a layer of fibrous connective tissue with collagen that indicates fibrous encapsulation.

Bibliography

(1) Frost, M.; Meyerhoff, M. E. In Vivo Chemical Sensors: Tackling Biocompatibility. *Anal. Chem.* **2006**, *78*, 7370-7377.

(2) Wisniewski, N.; Moussy, F.; Reichert, W. M. Characterization of Implantable Biosensor Membrane Biofouling. *Fresenius J. Anal. Chem.* **2000**, *366*, 611-621.

(3) Onuki, Y.; Bhardwaj, U.; Papadimitrakopoulos, F.; Burgess, D. J. A Review of the Biocompatibility of Implantable Devices: Current Challenges to Overcome Foreign Body Response. *J. Diabetes Sci. Technol.* **2008**, *2*, 1003-1015.

(4) Gifford, R.; Kehoe, J. J.; Barnes, S. L.; Kornilayev, B. A.; Alterman, M. A.; Wilson, G. S. Protein Interactions with Subcutaneously Implanted Biosensors. *Biomaterials* **2006**, *27*, 2587-2598.

(5) Wilson, G. S.; Gifford, R. Biosensors for Real-Time in Vivo Measurements. *Biosens. Bioelectron.* **2005**, *20*, 2388-2403.

(6) Hung-Wei Chiu; Mu-Lien Lin; Chii-Wann Lin; I-Hsiu Ho; Wei-Tso Lin; Po-Hsiang Fang; Yi-Chin Lee; Yeong-Ray Wen; Shey-Shi Lu Pain Control on Demand Based on Pulsed Radio-Frequency Stimulation of the Dorsal Root Ganglion using a Batteryless Implantable CMOS SoC. *IEEE Trans Biomed Circuits Syst.* **2010**, *4*, 350-359.

(7) Lin, P.; Lin, C.; Mansour, R.; Gu, F. Improving Biocompatibility by Surface Modification Techniques on Implantable Bioelectronics. *Biosens. Bioelectron.* **2013**, *47*, 451-460.

(8) Harbers, G. M.; Emoto, K.; Greef, C.; Metzger, S. W.; Woodward, H. N.; Mascali, J. J.; Grainger, D. W.; Lochhead, M. J. A Functionalized Poly(Ethylene Glycol)-Based Bioassay Surface Chemistry that Facilitates Bio-Immobilization and Inhibits Non-Specific Protein, Bacterial, and Mammalian Cell Adhesion. *Chem. Mater.* **2007**, *19*, 4405-4414.

(9) Yoshimoto, K.; Hirase, T.; Nemoto, S.; Hatta, T.; Nagasaki, Y. Facile Construction of Sulfanyl-Terminated Poly(Ethylene Glycol)-Brushed Layer on a Gold Surface for Protein Immobilization by the Combined use of Sulfanyl-Ended Telechelic and Semitelechelic Poly(Ethylene Glycol)S. *Langmuir* **2008**, *24*, 9623-9629.

(10) Hyun, J.; Jang, H.; Kim, K.; Na, K.; Tak, T. Restriction of Biofouling in Membrane Filtration using a Brush-Like Polymer Containing Oligoethylene Glycol Side Chains. *J. Membr. Sci.* **2006**, *282*, 52-59.

(11) Sharma, S.; Johnson, R. W.; Desai, T. A. Evaluation of the Stability of Nonfouling Ultrathin Poly(Ethylene Glycol) Films for Silicon-Based Microdevices. *Langmuir* **2004**, *20*, 348-356.

(12) Jeon, S. I.; Lee, J. H.; Andrade, J. D.; De Gennes, P. G. Protein-Surface Interactions in the Presence of Polyethylene Oxide: I. Simplified Theory. *J. Colloid Interface Sci.* **1991**, *142*, 149-158.

(13) Jeon, S. I.; Andrade, J. D. Protein-Surface Interactions in the Presence of Polyethylene Oxide: II. Effect of Protein Size. *J. Colloid Interface Sci.* **1991**, *142*, 159-166.

(14) Kryuk, T. V.; Mikhal'chuk, V. M.; Petrenko, L. V.; Nelepova, O. A.; Nikolaevskii, A. N. Promising Inhibitors of Poly(Ethylene Glycol) Oxidation in Aqueous Solutions. *Pharm. Chem. J.* **2002**, *36*, 32-35.

(15) Kawai, F. Microbial Degradation of Polyethers. *Appl. Microbiol. Biotechnol.* **2002**, *58*, 30-38.

(16) Armstrong, J. K.; Hempel, G.; Koling, S.; Chan, L. S.; Fisher, T.; Meiselman, H. J.; Garratty, G. Antibody Against Poly(Ethylene Glycol) Adversely Affects PEG-Asparaginase Therapy in Acute Lymphoblastic Leukemia Patients. *Cancer* **2007**, *110*, 103-111.

(17) Bretscher, M. S.; Raff, M. C. Mammalian Plasma Membranes. *Nature* **1975**, *258*, 43-49.

(18) ZWAAL, R. F. A.; COMFURIUS, P.; VAN DEENEN,L.L.M. Membrane Asymmetry and Blood Coagulation. *Nature* **1977**, *268*, 358-360.

(19) Kitano, H.; Mori, T.; Takeuchi, Y.; Tada, S.; Gemmei-Ide, M.; Yokoyama, Y.; Tanaka, M. Structure of Water Incorporated in Sulfobetaine Polymer Films as Studied by ATR-FTIR. *Macromol. Biosci.* **2005**, *5*, 314-321.

(20) Young, G.; Bowers, R.; Hall, B.; Port, M. Clinical Comparison of Omafilcon A with Four Control Materials. *CLAO J.* **1997**, *23*, 249-258.

(21) Van Dijk, K. R. A.; Luijpen, M. W.; Van Someren, E. J. W.; Sergeant, J. A.; Scheltens, P.; Scherder, E. J. A. Peripheral Electrical Nerve Stimulation and Rest-Activity Rhythm in Alzheimer's Disease. *J. Sleep Res.* **2006**, *15*, 415-423.

(22) Jui-Mei Hsu; Rieth, L.; Normann, R. A.; Tathireddy, P.; Solzbacher, F. Encapsulation of an Integrated Neural Interface Device with Parylene C. *IEEE Trans. Biomed. Eng.* **2009**, *56*, 23-29.

(23) Svennersten, K.; Larsson, K. C.; Berggren, M.; Richter-Dahlfors, A. Organic Bioelectronics in Nanomedicine. *Biochim. Biophys. Acta, Gen. Subj.* **2011**, *1810*, 276-285.

(24) Boss, J. H.; Shajrawi, I.; Aunullah, J.; Mendes, D. G. The Relativity of Biocompatibility. A Critique of the Concept of Biocompatibility. *Isr. J. Med. Sci.* **1995**, *31*, 203-209.

(25) AnonymousWorld Health Organization and Alzheimer's Disease International Say Dementia Must Be A Global Health Priority | Alzheimer's Disease International. *http://www.alz.co.uk/media/120411* (accessed 6/4/2014, 2014).

(26) Scherder, E. J. A.; Bouma, A.; Steen, L. Influence of Transcutaneous Electrical Nerve Stimulation on Memory in Patients with Dementia of the Alzheimer Type. *J. Clin. Exp. Neuropsychol.* **1992**, *14*, 951-960.

(27) Scherder, E. J. A.; Bouma, A.; Steen, A. M. Effects of Short-Term Transcutaneous Electrical Nerve Stimulation on Memory and Affective Behaviour in Patients with Probable Alzheimer's Disease. *Behav. Brain Res.* **1995**, *67*, 211-219.

(28) Gough, D. A.; Kumosa, L. S.; Routh, T. L.; Lin, J. T.; Lucisano, J. Y. Function of an Implanted Tissue Glucose Sensor for More than 1 Year in Animals. *Sci. Transl. Med.* **2010**, *2*, 42-53.

(29) Williams, G. T.; Williams, W. J. Granulomatous Inflammation--a Review. *J. Clin. Pathol.* **1983**, *36*, 723-733.

(30) Kovacs, E. J. Fibrogenic Cytokines: The Role of Immune Mediators in the Development of Scar Tissue. *Immunol. Today* **1991**, *12*, 17-23.

(31) Kyrolainen, M.; Rigsby, P.; Eddy, S.; Vadgama, P. Bio-/Haemocompatibility: Implications and Outcomes for Sensors? *Acta Anaesthesiol Scand Suppl.* **1995**, *39*, 55-60.

(32) Rigby, G. P.; Ahmed, S.; Horseman, G.; Vadgama, P. In Vivo Glucose Monitoring with Open Microflow – Influences of Fluid Composition and Preliminary Evaluation in Man. *Anal. Chim. Acta* **1999**, *385*, 23-32.

(33) Fournier, E.; Passirani, C.; Montero-Menei, C. N.; Benoit, J. P. Biocompatibility of Implantable Synthetic Polymeric Drug Carriers: Focus on Brain Biocompatibility. *Biomaterials* **2003**, *24*, 3311-3331.

(34) Ratner, B. D.; Hoffman, A. S.; Schoen, F. J.; Lemons, J. E. In *Biomaterials Science: An Introduction to Materials in Medicine;* Elsevier: Burlington, 2004; , pp 879.

(35) PERRETTI, M.; AHLUWALIA, A. The Microcirculation and Inflammation: Site of Action for Glucocorticoids. *Microcirculation* **2000**, *7*, 147-161.

(36) Morais, J. M.; Papadimitrakopoulos, F.; Burgess, D. J. Biomaterials/Tissue Interactions: Possible Solutions to Overcome Foreign Body Response. *AAPS J.* **2010**, *12*, 188-196.

(37) Patil, S. D.; Papadimitrakopoulos, F.; Burgess, D. J. Dexamethasone-Loaded Poly(Lactic-Co-Glycolic) Acid Microspheres/Poly(Vinyl Alcohol) Hydrogel Composite Coatings for Inflammation Control. *Diabetes Technol. Ther.* **2004**, *6*, 887-897.

(38) Patil, S. D.; Papadmitrakopoulos, F.; Burgess, D. J. Concurrent Delivery of Dexamethasone and VEGF for Localized Inflammation Control and Angiogenesis. *J. Control. Release* **2007**, *117*, 68-79.

(39) Kedem, A.; Perets, A.; Gamlieli-Bonshtein, I.; Dvir-Ginzberg, M.; Mizrahi, S.; Cohen, S. Vascular Endothelial Growth Factor-Releasing Scaffolds Enhance Vascularization and Engraftment of Hepatocytes Transplanted on Liver Lobes. *Tissue Eng.* **2005**, *11*, 715-722.

(40) Vaddiraju, S.; Tomazos, I.; Burgess, D. J.; Jain, F. C.; Papadimitrakopoulos, F. Emerging Synergy between Nanotechnology and Implantable Biosensors: A Review. *Biosens. Bioelectron.* **2010**, *25*, 1553-1565.

(41) Wisniewski, N.; Reichert, M. Methods for Reducing Biosensor Membrane Biofouling. *Colloids Surf. B Biointerfaces* **2000**, *18*, 197-219.

(42) Leckband, D.; Israelachvili, J. Intermolecular Forces in Biology. *Q. Rev. Biophys.* **2001**, *34*, 105-267.

(43) Richardson, S. On the no-Slip Boundary Condition. *J. Fluid Mech.* **1973**, *59*, 707-719.

(44) Lee, C.; Choi, C. H.; Kim, C. J. Structured Surfaces for a Giant Liquid Slip. *Phys. Rev. Lett.* **2008**, *101*, 064501.

(45) Athanasiou, K. A.; Niederauer, G. G.; Agrawal, C. M. Sterilization, Toxicity, Biocompatibility and Clinical Applications of Polylactic Acid/ Polyglycolic Acid Copolymers. *Biomaterials* **1996**, *17*, 93-102.

(46) Anderson, J. M.; Shive, M. S. Biodegradation and Biocompatibility of PLA and PLGA Microspheres. *Adv. Drug Deliv. Rev.* **1997**, *28*, 5-24.

(47) Espadas-Torre, C.; Meyerhoff, M. E. Thrombogenic Properties of Untreated and Poly(Ethylene Oxide)-Modified Polymeric Matrixes Useful for Preparing Intraarterial Ion-Selective Electrodes. *Anal. Chem.* **1995**, *67*, 3108-3114.

(48) Alconcel, S. N. S.; Baas, A. S.; Maynard, H. D. FDA-Approved Poly(Ethylene Glycol)–protein Conjugate Drugs. *Polym. Chem.* **2011**, *2*, 1442.

(49) Ostuni, E.; Chapman, R. G.; Holmlin, R. E.; Takayama, S.; Whitesides, G. M. A Survey of Structure-Property Relationships of Surfaces that Resist the Adsorption of Protein. *Langmuir* **2001**, *17*, 5605-5620.

(50) Chapman, R. G.; Ostuni, E.; Takayama, S.; Holmlin, R. E.; Yan, L.; Whitesides, G. M. Surveying for Surfaces that Resist the Adsorption of Proteins. *J. Am. Chem. Soc.* **2000**, *122*, 8303-8304.

(51) Zheng, J.; Li, L.; Tsao, H. K.; Sheng, Y. J.; Chen, S.; Jiang, S. Strong Repulsive Forces between Protein and Oligo (Ethylene Glycol) Self-Assembled Monolayers: A Molecular Simulation Study. *Biophys. J.* **2005**, *89*, 158-166.

(52) Zheng, J.; Li, L.; Chen, S.; Jiang, S. Molecular Simulation Study of Water Interactions with Oligo (Ethylene Glycol)-Terminated Alkanethiol Self-Assembled Monolayers. *Langmuir* **2004**, *20*, 8931-8938.

(53) Pertsin, A. J.; Grunze, M. Computer Simulation of Water Near the Surface of Oligo(Ethylene Glycol)-Terminated Alkanethiol Self-Assembled Monolayers†. *Langmuir* **2000**, *16*, 8829-8841.

(54) Archambault, J. G.; Brash, J. L. Protein Repellent Polyurethane-Urea Surfaces by Chemical Grafting of Hydroxyl-Terminated Poly(Ethylene Oxide): Effects of Protein Size and Charge. *Colloids Surf. B Biointerfaces* **2004**, *33*, 111-120.

(55) Herrwerth, S.; Eck, W.; Reinhardt, S.; Grunze, M. Factors that Determine the Protein Resistance of Oligoether Self-Assembled Monolayers - Internal Hydrophilicity, Terminal Hydrophilicity, and Lateral Packing Density. *J. Am. Chem. Soc.* **2003**, *125*, 9359-9366.

(56) Chen, S.; Liu, L.; Jiang, S. Strong Resistance of Oligo(Phosphorylcholine) Self-Assembled Monolayers to Protein Adsorption. *Langmuir* **2006**, *22*, 2418-2421.

(57) Rixman, M. A.; Dean, D.; Macias, C. E.; Ortiz, C. Nanoscale Intermolecular Interactions between Human Serum Albumin and Alkanethiol Self-Assembled Monolayers. *Langmuir* **2003**, *19*, 6202-6218.

(58) Chen, S.; Li, L.; Zhao, C.; Zheng, J. Surface Hydration: Principles and Applications Toward Low-Fouling/Nonfouling Biomaterials. *Polymer* **2010**, *51*, 5283-5293.

(59) Warkentin, P. H.; Lundström, I.; Tengvall, P. Proteins at Interfaces II; Protein—Protein Interactions Affecting Proteins at Surfaces. **1995**, *602*, 163-180.

(60) Tsai, I. Y.; Tomczyk, N.; Eckmann, J. I.; Composto, R. J.; Eckmann, D. M. Human Plasma Protein Adsorption Onto Dextranized Surfaces: A Two-Dimensional Electrophoresis and Mass Spectrometry Study. *Colloids Surf. B Biointerfaces* **2011**, *84*, 241-252.

(61) Lüsse, S.; Arnold, K. The Interaction of Poly(Ethylene Glycol) with Water Studied by1H and2H NMR Relaxation Time Measurements. *Macromolecules* **1996**, *29*, 4251-4257.

(62) Chang, Y.; Chu, W.; Chen, W.; Zheng, J.; Liu, L.; Ruaan, R.; Higuchi, A. A Systematic SPR Study of Human Plasma Protein Adsorption Behavior on the Controlled Surface Packing of Self-Assembled Poly(Ethylene Oxide) Triblock Copolymer Surfaces. *J. Biomed. Mater. Res. A* **2010**, *93A*, 400-408.

(63) Gao, C.; Li, G.; Xue, H.; Yang, W.; Zhang, F.; Jiang, S. Functionalizable and Ultra-Low Fouling Zwitterionic Surfaces Via Adhesive Mussel Mimetic Linkages. *Biomaterials* **2010**, *31*, 1486-1492.

(64) Dalsin, J. L.; Lin, L.; Tosatti, S.; Vörös, J.; Textor, M.; Messersmith, P. B. Protein Resistance of Titanium Oxide Surfaces Modified by Biologically Inspired mPEG-DOPA. *Langmuir* **2005**, *21*, 640-646.

(65) Tan, J.; Brash, J. L. Nonfouling Biomaterials Based on Polyethylene Oxide-Containing Amphiphilic Triblock Copolymers as Surface Modifying Additives: Solid State Structure of PEO-Copolymer/Polyurethane Blends. *Journal of Biomedical Materials Research Part A* **2008**, *85A*, 862-872.

(66) Zhang, Z.; Vaisocherova´, H.; Cheng, G.; Yang, W.; Xue, H.; Jiang, S. Nonfouling Behavior of Polycarboxybetaine-Grafted Surfaces: Structural and Environmental Effects. *Biomacromolecules* **2008**, *9*, 2686-2692.

(67) Otsuka, H.; Satomi, T.; Ueno, K.; Mitamura, Y.; Tateishi, T. Synthesis of Polypyridine-Graft-PEG Copolymer for Long-Term Stability of Nonfouling Character. *Trans. Mater. Res. Soc. Jpn.* **2006**, *31*, 627-631.

(68) Ladd, J.; Zhang, Z.; Chen, S.; Hower, J. C.; Jiang, S. Zwitterionic Polymers Exhibiting High Resistance to Nonspecific Protein Adsorption from Human Serum and Plasma. *Biomacromolecules* **2008**, *9*, 1357-1361.

(69) Bernards, M. T.; Cheng, G.; Zhang, Z.; Chen, S.; Jiang, S. Nonfouling Polymer Brushes Via Surface-Initiated, Two-Component Atom Transfer Radical Polymerization. *Macromolecules* **2008**, *41*, 4216-4219.

(70) Johnston, E. E.; Bryers, J. D.; Ratner, B. D. Plasma Deposition and Surface Characterization of Oligoglyme, Dioxane, and Crown Ether Nonfouling Films. *Langmuir* **2005**, *21*, 870-881.

(71) Roberts, M. J.; Bentley, M. D.; Harris, J. M. Chemistry for Peptide and Protein PEGylation. *Adv. Drug Deliv. Rev.* **2002**, *54*, 459-476.

(72) Shen, M.; Pan, Y. V.; Wagner, M. S.; Hauch, K. D.; Castner, D. G.; Ratner, B. D.; Horbett, T. A. Inhibition of Monocyte Adhesion and Fibrinogen Adsorption on Glow Discharge Plasma Deposited Tetraethylene Glycol Dimethyl Ether. *J. Biomater. Sci. Polym. Ed.* **2001**, *12*, 961-978.

(73) Li, L.; Chen, S.; Jiang, S. Protein Interactions with Oligo(Ethylene Glycol) (OEG) Self-Assembled Monolayers: OEG Stability, Surface Packing Density and Protein Adsorption. *J. Biomater. Sci. Polym. Ed.* **2007**, *18*, 1415-1427.

(74) Reitsma, S.; Slaaf, D. W.; Vink, H.; Zandvoort, M. A. M. J.; oude Egbrink, M. G. A. The Endothelial Glycocalyx: Composition, Functions, and Visualization. *Pflugers Arch.* **2007**, *454*, 345-359.

(75) Van Teeffelen, J. W.; Brands, J.; Stroes, E. S.; Vink, H. Endothelial Glycocalyx: Sweet Shield of Blood Vessels. *Trends Cardiovasc. Med.* **2007**, *17*, 101-105.

(76) Holland, N. B.; Qiu, Y.; Ruegsegger, M.; Marchant, R. E. Biomimetic Engineering of Non-Adhesive Glycocalyx-Like Surfaces using Oligosaccharide Surfactant Polymers. *Nature* **1998**, *392*, 799-801.

(77) D'Sa, R. A.; Meenan, B. J. Chemical Grafting of Poly(Ethylene Glycol) Methyl Ether Methacrylate Onto Polymer Surfaces by Atmospheric Pressure Plasma Processing. *Langmuir* **2010**, *26*, 1894-1903.

(78) Zoulalian, V.; Zu¨rcher, S.; Tosatti, S.; Textor, M.; Monge, S.; Robin, J. Self-Assembly of Poly(Ethylene Glycol)-Poly(Alkyl Phosphonate) Terpolymers on Titanium Oxide Surfaces: Synthesis, Interface Characterization, Investigation of Nonfouling Properties, and Long-Term Stability. *Langmuir* **2010**, *26*, 74-82.

(79) Schuler, M.; Hamilton, D. W.; Kunzler, T. P.; Sprecher, C. M.; de Wild, M.; Brunette, D. M.; Textor, M.; Tosatti, S. G. P. Comparison of the Response of Cultured Osteoblasts and Osteoblasts Outgrown from Rat Calvarial Bone Chips to Nonfouling KRSR and FHRRIKA-Peptide Modified Rough Titanium Surfaces. *J. Biomed. Mater. Res. Part B Appl. Biomater.* **2009**, *91B*, 517-527.

(80) Maddikeri, R. R.; Tosatti, S.; Schuler, M.; Chessari, S.; Textor, M.; Richards, R. G.; Harris, L. G. Reduced Medical Infection Related Bacterial Strains Adhesion on Bioactive RGD Modified Titanium Surfaces: A First Step Toward Cell Selective Surfaces. *J. Biomed. Mater. Res. A* **2008**, *84A*, 425-435.

(81) Tugulu, S.; Klok, H. Surface Modification of Polydimethylsiloxane Substrates with Nonfouling Poly(Poly(Ethylene Glycol)Methacrylate) Brushes. *Macromol. Symp.* **2009**, *279*, 103-109.

(82) Tugulu, S.; Klok, H. Stability and Nonfouling Properties of Poly(Poly(Ethylene Glycol) Methacrylate) Brushes Under Cell Culture Conditions. *Biomacromolecules* **2008**, *9*, 906-912.

(83) Wang, J.; Gibson, M. I.; Barbey, R.; Xiao, S.; Klok, H. Nonfouling Polypeptide Brushes Via Surface-Initiated Polymerization ofNe-Oligo(Ethylene Glycol)Succinate-L-lysineN-Carboxyanhydride. *Macromol. Rapid Commun.* **2009**, *30*, 845-850.

(84) Hucknall, A.; Simnick, A. J.; Hill, R. T.; Chilkoti, A.; Garcia, A.; Johannes, M. S.; Clark, R. L.; Zauscher, S.; Ratner, B. D. Versatile Synthesis and Micropatterning of Nonfouling Polymer Brushes on the Wafer Scale. *Biointerphases* **2009**, *4*, FA50-FA57.

(85) Hucknall, A.; Kim, D.; Rangarajan, S.; Hill, R. T.; Reichert, W. M.; Chilkoti, A. Simple Fabrication of Antibody Microarrays on Nonfouling Polymer Brushes with Femtomolar Sensitivity for Protein Analytes in Serum and Blood. *Adv Mater* **2009**, *21*, 1968-1971.

(86) Cheng, G.; Zhang, Z.; Chen, S.; Bryers, J. D.; Jiang, S. Inhibition of Bacterial Adhesion and Biofilm Formation on Zwitterionic Surfaces. *Biomaterials* **2007**, *28*, 4192-4199.

(87) Zhang, Z.; Zhang, M.; Chen, S.; Horbett, T. A.; Ratner, B. D.; Jiang, S. Blood Compatibility of Surfaces with Superlow Protein Adsorption. *Biomaterials* **2008**, *29*, 4285-4291.

(88) Tan, J.; L. Brash, J. Nonfouling Biomaterials Based on Polyethylene Oxide-Containing Amphiphilic Triblock Copolymers as Surface Modifying Additives: Synthesis and Characterization of Copolymers and Surface Properties of Copolymer–polyurethane Blends. *J Appl Polym Sci* **2008**, *108*, 1617-1628.

(89) Tan, J.; Brash, J. L. Nonfouling Biomaterials Based on Polyethylene Oxide-Containing Amphiphilic Triblock Copolymers as Surface Modifying Additives: Adsorption of Proteins from Human Plasma to Copolymer/Polyurethane Blends. *J. Biomed. Mater. Res. A* **2009**, *90A*, 196-204.

(90) Tan, J.; McClung, W. G.; Brash, J. L. Nonfouling Biomaterials Based on Polyethylene Oxide-Containing Amphiphilic Triblock Copolymers as Surface Modifying Additives: Protein Adsorption on PEO-Copolymer/Polyurethane Blends. *J. Biomed. Mater. Res. A* **2008**, *85A*, 873-880.

(91) Sheu, M. S.; Hoffman, A. S.; Feijen, J. A Glow Discharge Treatment to Immobilize Poly(Ethylene Oxide)/Poly(Propylene Oxide) Surfactants for Wettable and Non-Fouling Biomaterials. *J. Adhes. Sci. Technol.* **1992**, *6*, 995-1009.

(92) Leckband, D.; Sheth, S.; Halperin, A. Grafted Poly(Ethylene Oxide) Brushes as Nonfouling Surface Coatings. *J. Biomater. Sci. Polym. Ed.* **1999**, *10*, 1125-1147.

(93) Harbers, G. M.; Emoto, K.; Greef, C.; Metzger, S. W.; Woodward, H. N.; Mascali, J. J.; Grainger, D. W.; Lochhead, M. J. Functionalized Poly(Ethylene Glycol)-Based Bioassay Surface Chemistry that Facilitates Bio-Immobilization and Inhibits Nonspecific Protein, Bacterial, and Mammalian Cell Adhesion. *Chem. Mater.* **2007**, *19*, 4405-4414.

(94) Kingshott, P.; Wei, J.; Bagge-Ravn, D.; Gadegaard, N.; Gram, L. Covalent Attachment of Poly(Ethylene Glycol) to Surfaces, Critical for Reducing Bacterial Adhesion. *Langmuir* **2003**, *19*, 6912-6921.

(95) Dalsin, J. L.; Hu, B.; Lee, B. P.; Messersmith, P. B. Mussel Adhesive Protein Mimetic Polymers for the Preparation of Nonfouling Surfaces. *J. Am. Chem. Soc.* **2003**, *125*, 4253-4258.

(96) Li, L.; Chen, S.; Zheng, J.; Ratner, B. D.; Jiang, S. Protein Adsorption on Oligo(Ethylene Glycol)-Terminated Alkanethiolate Self-Assembled Monolayers: The Molecular Basis for Nonfouling Behavior. *J. Phys. Chem.* **2005**, *109*, 2934-2941.

(97) Chen, S.; Jiang, S. An New Avenue to Nonfouling Materials. *Adv Mater* **2008**, *20*, 335-338.

(98) Konradi, R.; Pidhatika, B.; Mühlebach, A.; Textor, M. Poly-2-Methyl-2-Oxazoline: A Peptide-Like Polymer for Protein-Repellent Surfaces. *Langmuir* **2008**, *24*, 613-616.

(99) Pidhatika, B.; Möller, J.; Vogel, V.; Konradi, R. Nonfouling Surface Coatings Based on Poly(2-Methyl-2-Oxazoline). *CHIMIA International Journal for Chemistry* **2008**, *62*, 264-269.

(100) Wyszogrodzka, M.; Haag, R. Synthesis and Characterization of Glycerol Dendrons, Self-Assembled Monolayers on Gold: A Detailed Study of their Protein Resistance. *Biomacromolecules* **2009**, *10*, 1043-1054.

(101) Kainthan, R. K.; Zou, Y.; Chiao, M.; Kizhakkedathu, J. N. Self-Assembled Monothiol-Terminated Hyperbranched Polyglycerols on a Gold Surface: A Comparative Study on the Structure, Morphology, and Protein Adsorption Characteristics with Linear Poly(Ethylene Glycol)S. *Langmuir* **2008**, *24*, 4907-4916.

(102) Zhang, M.; Horbett, T. A. Tetraglyme Coatings Reduce Fibrinogen and Von Willebrand Factor Adsorption and Platelet Adhesion Under both Static and Flow Conditions. *J. Biomed. Mater. Res. A* **2009**, *89A*, 791-803.

(103) Cao, L.; Chang, M.; Lee, C.; Castner, D. G.; Sukavaneshvar, S.; Ratner, B. D.; Horbett, T. A. Plasma-Deposited Tetraglyme Surfaces Greatly Reduce Total Blood Protein Adsorption, Contact Activation, Platelet Adhesion, Platelet Procoagulant Activity, Andin Vitro Thrombus Deposition. *J. Biomed. Mater. Res. A* **2007**, *81A*, 827-837.

(104) Shen, M.; Martinson, L.; Wagner, M. S.; Castner, D. G.; Ratner, B. D.; Horbett, T. A. PEO-Like Plasma Polymerized Tetraglyme Surface Interactions with Leukocytes and Proteins: In Vitro and in Vivo Studies. *J. Biomater. Sci. Polym. Ed.* **2002**, *13*, 367-390.

(105) Shen, M.; Wagner, M. S.; Castner, D. G.; Ratner, B. D.; Horbett, T. A. Multivariate Surface Analysis of Plasma-Deposited Tetraglyme for Reduction of Protein Adsorption and Monocyte Adhesion†. *Langmuir* **2003**, *19*, 1692-1699.

(106) McArthur, S. L.; McLean, K. M.; Kingshott, P.; St John, H. A. W.; Chatelier, R. C.; Griesser, H. J. Effect of Polysaccharide Structure on Protein Adsorption. *Colloids Surf. B Biointerfaces* **2000**, *17*, 37-48.

(107) Mrabet, B.; Nguyen, M. N.; Majbri, A.; Mahouche, S.; Turmine, M.; Bakhrouf, A.; Chehimi, M. M. Anti-Fouling Poly(2-Hydoxyethyl Methacrylate) Surface Coatings with Specific Bacteria Recognition Capabilities. *Surf. Sci.* **2009**, *603*, 2422-2429.

(108) Ishihara, K.; Ishikawa, E.; Iwasaki, Y.; Nakabayashi, N. Inhibition of Fibroblast Cell Adhesion on Substrate by Coating with 2-Methacryloyloxyethyl Phosphorylcholine Polymers. *J. Biomater. Sci. Polym. Ed.* **1999**, *10*, 1047-1061.

(109) Amanda, A.; Mallapragada, S. K. Comparison of Protein Fouling on Heat-Treated Poly(Vinyl Alcohol), Poly(Ether Sulfone) and Regenerated Cellulose Membranes using Diffuse Reflectance Infrared Fourier Transform Spectroscopy. *Biotechnol. Prog.* **2001**, *17*, 917-923.

(110) Chapman, R. G.; Ostuni, E.; Liang, M. N.; Meluleni, G.; Kim, E.; Yan, L.; Pier, G.; Warren, H. S.; Whitesides, G. M. Polymeric Thin Films that Resist the Adsorption of Proteins and the Adhesion of Bacteria. *Langmuir* **2001**, *17*, 1225-1233.

(111) Ostuni, E.; Chapman, R. G.; Liang, M. N.; Meluleni, G.; Pier, G.; Ingber, D. E.; Whitesides, G. M. Self-Assembled Monolayers that Resist the Adsorption of Proteins and the Adhesion of Bacterial and Mammalian Cells. *Langmuir* **2001**, *17*, 6336-6343.

(112) Chelmowski, R.; Ko¨ster, S. D.; Kerstan, A.; Prekelt, A.; Grunwald, C.; Winkler, T.; Metzler-Nolte, N.; Terfort, A.; Wo¨ll, C. Peptide-Based SAMs that Resist the Adsorption of Proteins. *J. Am. Chem. Soc.* **2008**, *130*, 14952-14953.

(113) Koc, Y.; de Mello, A. J.; McHale, G.; Newton, M. I.; Roach, P.; Shirtcliffe, N. J. Nano-Scale Superhydrophobicity: Suppression of Protein Adsorption and Promotion of Flow-Induced Detachment. *Lab. Chip* **2008**, *8*, 582-586.

(114) Bhushan, B.; Jung, Y. C. Natural and Biomimetic Artificial Surfaces for Superhydrophobicity, Self-Cleaning, Low Adhesion, and Drag Reduction. *Prog. Mater. Sci.* **2011**, *56*, 1-108.

(115) Brault, N. D.; Sundaram, H. S.; Li, Y.; Huang, C.; Yu, Q.; Jiang, S. Dry Film Refractive Index as an Important Parameter for Ultra-Low Fouling Surface Coatings. *Biomacromolecules* **2012**, *13*, 589-593.

(116) Yang, W.; Xue, H.; Carr, L. R.; Wang, J.; Jiang, S. Zwitterionic Poly(Carboxybetaine) Hydrogels for Glucose Biosensors in Complex Media. *Biosens. Bioelectron.* **2011**, *26*, 2454-2459.

(117) Rosen, J. E.; Gu, F. Surface Functionalization of Silica Nanoparticles with Cysteine: A Low-Fouling Zwitterionic Surface. *Langmuir* **2011**, *27*, 10507-10513.

(118) Chen, S.; Cao, Z.; Jiang, S. Ultra-Low Fouling Peptide Surfaces Derived from Natural Amino Acids. *Biomaterials* **2009**, *30*, 5892-5896.

(119) Ma, Z.; Han, H. One-Step Synthesis of Cystine-Coated Gold Nanoparticles in Aqueous Solution. *Colloids Surf. Physicochem. Eng. Aspects* **2008**, *317*, 229-233.

(120) Gonella, G.; Terreni, S.; Cvetko, D.; Cossaro, A.; Mattera, L.; Cavalleri, O.; Rolandi, R.; Morgante, A.; Floreano, L.; Canepa, M. Ultrahigh Vacuum Deposition of L-Cysteine on Au(110) Studied by High-Resolution X-Ray Photoemission: From Early Stages of Adsorption to Molecular Organization. *J. Phys. Chem. B* **2005**, *109*, 18003-18009.

(121) Zhang, Z.; Cheng, G.; Carr, L. R.; Vaisocherová, H.; Chen, S.; Jiang, S. The Hydrolysis of Cationic Polycarboxybetaine Esters to Zwitterionic Polycarboxybetaines with Controlled Properties. *Biomaterials* **2008**, *29*, 4719-4725.

(122) Vaisocherová, H.; Yang, W.; Zhang, Z.; Cao, Z.; Cheng, G.; Piliarik, M.; Homola, J.; Jiang, S. Ultralow Fouling and Functionalizable Surface Chemistry Based on a Zwitterionic Polymer Enabling Sensitive and Specific Protein Detection in Undiluted Blood Plasma. *Anal. Chem.* **2008**, *80*, 7894-7901.

(123) Vaisocherová, H.; Zhang, Z.; Yang, W.; Cao, Z.; Cheng, G.; Taylor, A. D.; Piliarik, M.; Homola, J.; Jiang, S. Functionalizable Surface Platform with Reduced Nonspecific Protein Adsorption from Full Blood plasma—Material Selection and Protein Immobilization Optimization. *Biosens. Bioelectron.* **2009**, *24*, 1924-1930.

(124) Li, G.; Cheng, G.; Xue, H.; Chen, S.; Zhang, F.; Jiang, S. Ultra Low Fouling Zwitterionic Polymers with a Biomimetic Adhesive Group. *Biomaterials* **2008**, *29*, 4592-4597.

(125) Li, G.; Xue, H.; Cheng, G.; Chen, S.; Zhang, F.; Jiang, S. Ultralow Fouling Zwitterionic Polymers Grafted from Surfaces Covered with an Initiator Via an Adhesive Mussel Mimetic Linkage. *J. Phys. Chem. B* **2008**, *112*, 15269-15274.

(126) Zhang, Z.; Chen, S.; Jiang, S. Dual-Functional Biomimetic Materials: Nonfouling Poly(Carboxybetaine) with Active Functional Groups for Protein Immobilization. *Biomacromolecules* **2006**, *7*, 3311-3315.

(127) Cheng, G.; Xue, H.; Zhang, Z.; Chen, S.; Jiang, S. A Switchable Biocompatible Polymer Surface with Self-Sterilizing and Nonfouling Capabilities. *Angew. Chem. Int. Ed.* **2008**, *47*, 8831-8834.

(128) Ishihara, K.; Hasegawa, T.; Watanabe, J.; Iwasaki, Y. Protein Adsorption-Resistant Hollow Fibers for Blood Purification. *Artif. Organs* **2002**, *26*, 1014-1019.

(129) Hasegawa, T.; Iwasaki, Y.; Ishihara, K. Preparation of Blood-Compatible Hollow Fibers from a Polymer Alloy Composed of Polysulfone and 2-Methacryloyloxyethyl Phosphorylcholine Polymer. *J. Biomed. Mater. Res.* **2002**, *63*, 333-341.

(130) Chen, S.; Yu, F.; Yu, Q.; He, Y.; Jiang, S. Strong Resistance of a Thin Crystalline Layer of Balanced Charged Groups to Protein Adsorption. *Langmuir* **2006**, *22*, 8186-8191.

(131) Li, G.; Xue, H.; Gao, C.; Zhang, F.; Jiang, S. Nonfouling Polyampholytes from an Ion-Pair Comonomer with Biomimetic Adhesive Groups. *Macromolecules* **2010**, *43*, 14-16.

(132) Yi, S. J.; Yuk, J. S.; Jung, S. H.; Zhavnerko, G. K.; Kim, Y. M.; Ha, K. S. Investigation of Selective Protein Immobilization on Charged Protein Array by Wavelength Interrogation-Based SPR Sensor. *Mol. Cells* **2003**, *15*, 333-340.

(133) Hsu, J. M. i.; Rieth, L.; Normann, R. A.; Tathireddy, P.; Solzbacher, F. Encapsulation of an Integrated Neural Interface Device with Parylene C. *IEEE Trans. Biomed. Eng.* **2009**, *56*, 23-29.

(134) Holmlin, R. E.; Chen, X.; Chapman, R. G.; Takayama, S.; Whitesides, G. M. Zwitterionic SAMs that Resist Nonspecific Adsorption of Protein from Aqueous Buffer. *Langmuir* **2001**, *17*, 2841-2850.

(135) Yang, W.; Xue, H.; Li, W.; Zhang, J.; Jiang, S. Pursuing "Zero" Protein Adsorption of Poly(Carboxybetaine) from Undiluted Blood Serum and Plasma. *Langmuir* **2009**, *25*, 11911-11916.

(136) Zhang, L.; Cao, Z.; Bai, T.; Carr, L.; Ella-Menye, J.; Irvin, C.; Ratner, B. D.; Jiang, S. Zwitterionic Hydrogels Implanted in Mice Resist the Foreign-Body Reaction. *Nat Biotech* **2013**, *31*, 553-556.

(137) Nowinski, A. K.; White, A. D.; Keefe, A. J.; Jiang, S. Biologically Inspired Stealth Peptide-Capped Gold Nanoparticles. *Langmuir* **2014**, *30*, 1864-1870.

(138) Zhu, Y.; Sundaram, H. S.; Liu, S.; Zhang, L.; Xu, X.; Yu, Q.; Xu, J.; Jiang, S. A Robust Graft-to Strategy to Form Multifunctional and Stealth Zwitterionic Polymer-Coated Mesoporous Silica Nanoparticles. *Biomacromolecules* **2014**, *15*, 1845-1851.

(139) Cao, Z.; Zhang, L.; Jiang, S. Superhydrophilic Zwitterionic Polymers Stabilize Liposomes. *Langmuir* **2012**, *28*, 11625-11632.

(140) Sinclair, A.; Bai, T.; Carr, L. R.; Ella-Menye, J.; Zhang, L.; Jiang, S. Engineering Buffering and Hydrolytic Or Photolabile Charge Shifting in a Polycarboxybetaine Ester Gene Delivery Platform. *Biomacromolecules* **2013**, *14*, 1587-1593.

(141) Murthy, A. K.; Stover, R. J.; Hardin, W. G.; Schramm, R.; Nie, G. D.; Gourisankar, S.; Truskett, T. M.; Sokolov, K. V.; Johnston, K. P. Charged Gold Nanoparticles with Essentially Zero Serum Protein Adsorption in Undiluted Fetal Bovine Serum. *J. Am. Chem. Soc.* **2013**, *135*, 7799-7802.

(142) Tlahuice-Flores, A. Zwitterion L-Cysteine Adsorbed on the Au(20) Cluster: Enhancement of Infrared Active Normal Modes. *J. Mol. Model.* **2013**, *19*, 1937-1942.

(143) Li, P.; Cai, X.; Wang, D.; Chen, S.; Yuan, J.; Li, L.; Shen, J. Hemocompatibility and Anti-Biofouling Property Improvement of Poly(Ethylene Terephthalate) Via Self-Polymerization of Dopamine and Covalent Graft of Zwitterionic Cysteine. *Colloids Surf. , B* **2013**, *110*, 327-332.

(144) Dodero, G.; De Michieli, L.; Cavalleri, O.; Rolandi, R.; Oliveri, L.; Daccà, A.; Parodi, R. L-Cysteine Chemisorption on Gold: An XPS and STM Study. *Colloids Surf. , A* **2000**, *175*, 121-128.

(145) Laibinis, P. E.; Bain, C. D.; Whitesides, G. M. Attenuation of Photoelectrons in Monolayers of N-Alkanethiols Adsorbed on Copper, Silver, and Gold. *J. Phys. Chem.* **1991**, *95*, 7017-7021.

(146) Uvdal, K.; Bodö, P.; Liedberg, B. L-Cysteine Adsorbed on Gold and Copper: An X-Ray Photoelectron Spectroscopy Study. *J. Colloid Interface Sci.* **1992**, *149*, 162-173.

(147) Cavalleri, O.; Gonella, G.; Terreni, S.; Vignolo, M.; Floreano, L.; Morgante, A.; Canepa, M.; Rolandi, R. High Resolution X-Ray Photoelectron Spectroscopy of L-Cysteine Self-Assembled Films. *Phys. Chem.* **2004**, *6*, 4042-4046.

(148) Beerbom, M. M.; Gargagliano, R.; Schlaf, R. Determination of the Electronic Structure of Self-Assembledl-Cysteine/Au Interfaces using Photoemission Spectroscopy. *Langmuir* **2005**, *21*, 3551-3558.

(149) Brizzolara, R. A. Cysteine by X-Ray Photoelectron Spectroscopy. *Surf. Sci. Spectra* **1996**, *4*, 102.

(150) Jacobs, L. C.; De Vogel, H. P.; Hemmes, K.; Wind, M. M.; De Wit, J. H. W. Potential Modulated Ellipsometric Measurements on an Fe-17Cr Alloy in Sulphuric Acid. *Corros. Sci.* **1995**, *37*, 1211-1233.

(151) Tengvall, P.; Lestelius, M.; Liedberg, B.; Lundstroem, I. Plasma Protein and Antisera Interactions with L-Cysteine and 3-Mercaptopropionic Acid Monolayers on Gold Surfaces. *Langmuir* **1992**, *8*, 1236-1238.

(152) Böhme, U.; Scheler, U. Effective Charge of Bovine Serum Albumin Determined by Electrophoresis NMR. *Chem. Phys. Lett.* **2007**, *435*, 342-345.

(153) Peters, T.,Jr Serum Albumin: Recent Progress in the Understanding of its Structure and Biosynthesis. *Clin. Chem.* **1977**, *23*, 5-12.

(154) Weijers, R. N. Amino Acid Sequence in Bovine Serum Albumin. *Clin. Chem.* **1977**, *23*, 1361-1362.

(155) La, Y.; McCloskey, B. D.; Sooriyakumaran, R.; Vora, A.; Freeman, B.; Nassar, M.; Hedrick, J.; Nelson, A.; Allen, R. Bifunctional Hydrogel Coatings for Water Purification Membranes: Improved Fouling Resistance and Antimicrobial Activity. *J. Membr. Sci.* **2011**, *372*, 285-291.

(156) Yang, R.; Gleason, K. K. Ultrathin Antifouling Coatings with Stable Surface Zwitterionic Functionality by Initiated Chemical Vapor Deposition (iCVD). *Langmuir* **2012**, *28*, 12266-12274.

(157) Zhao, J.; Shi, Q.; Luan, S.; Song, L.; Yang, H.; Shi, H.; Jin, J.; Li, X.; Yin, J.; Stagnaro, P. Improved Biocompatibility and Antifouling Property of Polypropylene Non-Woven Fabric Membrane by Surface Grafting Zwitterionic Polymer. *J. Membr. Sci.* **2011**, *369*, 5-12.

(158) Sağlam, D.; Venema, P.; de Vries, R.; Shi, J.; van der Linden, E. Concentrated Whey Protein Particle Dispersions: Heat Stability and Rheological Properties. *Food Hydrocoll.* **2013**, *30*, 100-109.

(159) D'Addio, S. M.; Chan, J. G.; Kwok, P. C.; Prud'homme, R. K.; Chan, H. K. Constant Size, Variable Density Aerosol Particles by Ultrasonic Spray Freeze Drying. *Int. J. Pharm.* **2012**, *427*, 185-191.

(160) Ravindran, A.; Singh, A.; Raichur, A. M.; Chandrasekaran, N.; Mukherjee, A. Studies on Interaction of Colloidal Ag Nanoparticles with Bovine Serum Albumin (BSA). *Colloids Surf. , B* **2010**, *76*, 32-37.

(161) Nayar, S.; Pramanick, A. K.; Sharma, B. K.; Mishra, R. K.; Bansal, S. K.; Prajapati, A.; Sahu, K. K.; Das, S. K.; Pathak, L.; Sinha, A. Hydroxyapatite Coating on Stainless Steel Pre-Coated with Bovine Serum Albumin at Ambient Conditions. *Colloids Surf. , B* **2006**, *48*, 183-187.

(162) Ma, M.; Hill, R. M. Superhydrophobic Surfaces. *Curr. Opin. Colloid Interface Sci.* **2006**, *11*, 193-202.

(163) Callies, M.; Quéré, D. On Water Repellency. *Soft matter* **2005**, *1*, 55-61.

(164) Koc, Y.; de Mello, A. J.; McHale, G.; Newton, M. I.; Roach, P.; Shirtcliffe, N. J. Nano-Scale Superhydrophobicity: Suppression of Protein Adsorption and Promotion of Flow-Induced Detachment. *Lab. Chip* **2008**, *8*, 582-586.

(165) Wen, X.; Xie, Y.; Mak, W. C.; Cheung, K. Y.; Li, X.; Renneberg, R.; Yang, S. Dendritic Nanostructures of Silver: Facile Synthesis, Structural Characterizations, and Sensing Applications. *Langmuir* **2006**, *22*, 4836-4842.

(166) Zawko, S. A.; Schmidt, C. E. Assembly of Sodium Soap Fibers and Fibrillar Particles Triggered by Dissolution of Sodium Chloride Crystals. *Soft Matter* **2010**, *6*, 3289-3297.

(167) Huang, D.; Qi, Y.; Bai, X.; Shi, L.; Jia, H.; Zhang, D.; Zheng, L. One-Pot Synthesis of Dendritic Gold Nanostructures in Aqueous Solutions of Quaternary Ammonium Cationic Surfactants: Effects of the Head Group and Hydrocarbon Chain Length. *ACS Appl. Mater. Interfaces* **2012**, *4*, 4665-4671.

(168) Qiu, R.; Cha, H. G.; Noh, H. B.; Shim, Y. B.; Zhang, X. L.; Qiao, R.; Zhang, D.; Kim, Y. I.; Pal, U.; Kang, Y. S. Preparation of Dendritic Copper Nanostructures and their Characterization for Electroreduction. *J. Phys. Chem. C* **2009**, *113*, 15891-15896.

(169) Witten, T.; Sander, L. Diffusion-Limited Aggregation, a Kinetic Critical Phenomenon. *Phys. Rev. Lett.* **1981**, *47*, 1400-1403.

(170) Wang, S.; Xin, H. Fractal and Dendritic Growth of Metallic Ag Aggregated from Different Kinds of ?-Irradiated Solutions. *J. Phys. Chem. B* **2000**, *104*, 5681-5685.

(171) Bixler, G. D.; Bhushan, B. Biofouling: Lessons from Nature. *Philos Transact A Math Phys Eng Sci* **2012**, *370*, 2381-2417.

(172) Shannon, M. A.; Bohn, P. W.; Elimelech, M.; Georgiadis, J. G.; Marinas, B. J.; Mayes, A. M. Science and Technology for Water Purification in the Coming Decades. *Nature* **2008**, *452*, 301-310.

(173) Matin, A.; Khan, Z.; Zaidi, S. M. J.; Boyce, M. C. Biofouling in Reverse Osmosis Membranes for Seawater Desalination: Phenomena and Prevention. *Desalination* **2011**, *281*, 1-16.

(174) Lin, P.; Ding, L.; Lin, C.; Gu, F. Nonfouling Property of Zwitterionic Cysteine Surface. *Langmuir* **2014**, *30*, 6497-6507.

(175) Warkentin, P. H.; Lundström, I.; Tengvall, P. In *Protein—Protein Interactions Affecting Proteins at Surfaces;* Proteins at Interfaces II; American Chemical Society: 1995; Vol. 602, pp 163-180.

(176) Andrade, J. D.; Hlady, V. In *Protein adsorption and materials biocompatibility: A tutorial review and suggested hypotheses;* Biopolymers/Non-Exclusion HPLC; Springer Berlin Heidelberg: Berlin, Heidelberg, 1986; pp 1-63.

(177) Zou, P.; Hartleb, W.; Lienkamp, K. It Takes Walls and Knights to Defend a Castle - Synthesis of Surface Coatings from Antimicrobial and Antibiofouling Polymers. *J. Mater. Chem.* **2012**, *22*, 19579-19589.

(178) Terayama, Y.; Kikuchi, M.; Kobayashi, M.; Takahara, A. Well-Defined Poly(Sulfobetaine) Brushes Prepared by Surface-Initiated ATRP using a Fluoroalcohol and Ionic Liquids as the Solvents. *Macromolecules* **2011**, *44*, 104-111.

(179) Chen, S.; Zheng, J.; Li, L.; Jiang, S. Strong Resistance of Phosphorylcholine Self-Assembled Monolayers to Protein Adsorption: Insights into Nonfouling Properties of Zwitterionic Materials. *J. Am. Chem. Soc.* **2005**, *127*, 14473-14478.

(180) Sundaram, H. S.; Han, X.; Nowinski, A. K.; Ella-Menye, J.; Wimbish, C.; Marek, P.; Senecal, K.; Jiang, S. One-Step Dip Coating of Zwitterionic Sulfobetaine Polymers on Hydrophobic and Hydrophilic Surfaces. *ACS Appl. Mater. Interfaces* **2014**, *6*, 6664-6671.

(181) Zhang, Z.; Chao, T.; Chen, S.; Jiang, S. Superlow Fouling Sulfobetaine and Carboxybetaine Polymers on Glass Slides. *Langmuir* **2006**, *22*, 10072-10077.

(182) Cheng, G.; Li, G.; Xue, H.; Chen, S.; Bryers, J. D.; Jiang, S. Zwitterionic Carboxybetaine Polymer Surfaces and their Resistance to Long-Term Biofilm Formation. *Biomaterials* **2009**, *30*, 5234-5240.

(183) Jiang, S.; Cao, Z. Ultralow-Fouling, Functionalizable, and Hydrolyzable Zwitterionic Materials and their Derivatives for Biological Applications. *Adv Mater* **2010**, *22*, 920-932.

(184) He, Y.; Chang, Y.; Hower, J. C.; Zheng, J.; Chen, S.; Jiang, S. Origin of Repulsive Force and Structure/Dynamics of Interfacial Water in OEG-Protein Interactions: A Molecular Simulation Study. *Phys. Chem. Chem. Phys.* **2008**, *10*, 5539-5544.

(185) He, Y.; Hower, J.; Chen, S.; Bernards, M. T.; Chang, Y.; Jiang, S. Molecular Simulation Studies of Protein Interactions with Zwitterionic Phosphorylcholine Self-Assembled Monolayers in the Presence of Water. *Langmuir* **2008**, *24*, 10358-10364.

(186) Shao, Q.; Jiang, S. Influence of Charged Groups on the Properties of Zwitterionic Moieties: A Molecular Simulation Study. *J Phys Chem B* **2014**.

(187) Shao, Q.; He, Y.; White, A. D.; Jiang, S. Difference in Hydration between Carboxybetaine and Sulfobetaine. *J Phys Chem B* **2010**, *114*, 16625-16631.

(188) Hower, J. C.; He, Y.; Jiang, S. A Molecular Simulation Study of Methylated and Hydroxyl Sugar-Based Self-Assembled Monolayers: Surface Hydration and Resistance to Protein Adsorption. *J. Chem. Phys.* **2008**, *129*, 12B601.

(189) Southall, N. T.; Dill, K. A.; Haymet, A. D. J. A View of the Hydrophobic Effect. *J Phys Chem B* **2002**, *106*, 521-533.

(190) Kitano, H.; Imai, M.; Sudo, K.; Ide, M. Hydrogen-Bonded Network Structure of Water in Aqueous Solution of Sulfobetaine Polymers. *J Phys Chem B* **2002**, *106*, 11391-11396.

(191) Kitano, H.; Sudo, K.; Ichikawa, K.; Ide, M.; Ishihara, K. Raman Spectroscopic Study on the Structure of Water in Aqueous Polyelectrolyte Solutions. *J Phys Chem B* **2000**, *104*, 11425-11429.

(192) Shao, Q.; Jiang, S. Effect of Carbon Spacer Length on Zwitterionic Carboxybetaines. *J Phys Chem B* **2013**, *117*, 1357-1366.

(193) Currie, E.; Norde, W.; Stuart, M. C. Tethered Polymer Chains: Surface Chemistry and their Impact on Colloidal and Surface Properties. *Adv. Colloid Interface Sci.* **2003**, *100*, 205-265.

(194) Kulikova, G. A.; Ryabinina, I. V.; Guseynov, S. S.; Parfenyuk, E. V. Calorimetric Study of Adsorption of Human Serum Albumin Onto Silica Powders. *Thermochimica Acta* **2010**, *503*, 65-69.

(195) Estephan, Z. G.; Schlenoff, P. S.; Schlenoff, J. B. Zwitteration as an Alternative to PEGylation. *Langmuir* **2011**, *27*, 6794-6800.

(196) Schlenoff, J. B.; Rmaile, A. H.; Bucur, C. B. Hydration Contributions to Association in Polyelectrolyte Multilayers and Complexes: Visualizing Hydrophobicity. *J. Am. Chem. Soc.* **2008**, *130*, 13589-13597.

(197) MathMol Library-University of New York *https://www.nyu.edu/pages/mathmol/library/life/life1.html* (accessed 09/27, 2016).

(198) Berendsen, H.; Grigera, J.; Straatsma, T. The Missing Term in Effective Pair Potentials. *J. Phys. Chem.* **1987**, *91*, 6269-6271.

(199) Jorgensen, W. L.; Maxwell, D. S.; Tirado-Rives, J. Development and Testing of the OPLS all-Atom Force Field on Conformational Energetics and Properties of Organic Liquids. *J. Am. Chem. Soc.* **1996**, *118*, 11225-11236.

(200) Kaminski, G. A.; Friesner, R. A.; Tirado-Rives, J.; Jorgensen, W. L. Evaluation and Reparametrization of the OPLS-AA Force Field for Proteins Via Comparison with Accurate Quantum Chemical Calculations on Peptides. *J Phys Chem B* **2001**, *105*, 6474-6487.

(201) Berendsen, H. J.; Postma, J. v.; van Gunsteren, W. F.; DiNola, A.; Haak, J. Molecular Dynamics with Coupling to an External Bath. *J. Chem. Phys.* **1984**, *81*, 3684-3690.

(202) Bussi, G.; Donadio, D.; Parrinello, M. Canonical Sampling through Velocity Rescaling. *J. Chem. Phys.* **2007**, *126*, 014101.

(203) Parrinello, M.; Rahman, A. Polymorphic Transitions in Single Crystals: A New Molecular Dynamics Method. *J. Appl. Phys.* **1981**, *52*, 7182-7190.

(204) Haynes, C. A.; Norde, W. Globular Proteins at Solid/Liquid Interfaces. *Colloids and Surfaces B: Biointerfaces* **1994**, *2*, 517-566.

(205) Israelachvili, J.; Wennerström, H. Role of Hydration and Water Structure in Biological and Colloidal Interactions. *Nature* **1996**, *379*, 219-225.

(206) Kidoaki, S.; Matsuda, T. Mechanistic Aspects of Protein/Material Interactions Probed by Atomic Force Microscopy. *Colloids and Surfaces B: Biointerfaces* **2002**, *23*, 153-163.

(207) Xu, L.; Logan, B. E. Interaction Forces between Colloids and Protein-Coated Surfaces Measured using an Atomic Force Microscope. *Environ. Sci. Technol.* **2005**, *39*, 3592-3600.

(208) Zhang, X.; Du, X.; Huang, X.; Lv, Z. Creating Protein-Imprinted Self-Assembled Monolayers with Multiple Binding Sites and Biocompatible Imprinted Cavities. *J. Am. Chem. Soc.* **2013**, *135*, 9248-9251.

(209) Prime, K. L.; Whitesides, G. M. Adsorption of Proteins Onto Surfaces Containing End-Attached Oligo (Ethylene Oxide): A Model System using Self-Assembled Monolayers. *J. Am. Chem. Soc.* **1993**, *115*, 10714-10721.

(210) Wischerhoff, E.; Uhlig, K.; Lankenau, A.; Börner, H. G.; Laschewsky, A.; Duschl, C.; Lutz, J. Controlled Cell Adhesion on PEG-based Switchable Surfaces. *Angew. Chem. Int. Ed.* **2008**, *47*, 5666-5668.

(211) Zhang, M.; Desai, T.; Ferrari, M. Proteins and Cells on PEG Immobilized Silicon Surfaces. *Biomaterials* **1998**, *19*, 953-960.

(212) Luk, Y.; Kato, M.; Mrksich, M. Self-Assembled Monolayers of Alkanethiolates Presenting Mannitol Groups are Inert to Protein Adsorption and Cell Attachment. *Langmuir* **2000**, *16*, 9604-9608.

(213) Zhang, Z.; Chen, S.; Chang, Y.; Jiang, S. Surface Grafted Sulfobetaine Polymers Via Atom Transfer Radical Polymerization as Superlow Fouling Coatings. *J Phys Chem B* **2006**, *110*, 10799-10804.

(214) Chu, S.; Liu, C.; Chang, Y.; Huang, C. In *In Sulfur-Containing Natural Zwitterionic Amino Acids and Derivative on Gold: Study on Physicochemical and Anti-fouling Properties;* 1st Global Conference on Biomedical Engineering & 9th Asian-Pacific Conference on Medical and Biological Engineering; Springer: 2015; , pp 21-23.

(215) Chandra, S.; Saleem, H.; Sebastian, S.; Sundaraganesan, N. The Spectroscopic (FT-IR, FT-Raman), NCA, First Order Hyperpolarizability, NBO Analysis, HOMO and LUMO Analysis of L-Cysteine by Ab Inito HF and Density Functional Method. *Spectrochim. Acta A Mol. Biomol. Spectrosc.* **2011**, *78*, 1515-1524.

(216) Moggach, S. A.; Allan, D. R.; Parsons, S.; Sawyer, L.; Warren, J. E. The Effect of Pressure on the Crystal Structure of hexagonalL-Cystine. *J. Synchrotron Radiat.* **2005**, *12*, 598-607.

(217) Roux, M. V.; Foces-Foces, C.; Notario, R.; Ribeiro da Silva, M. A. V.; Ribeiro da Silva,Maria das Dores M.C.; Santos, A. F. L. O. M.; Juaristi, E. Experimental and Computational Thermochemical Study of Sulfur-Containing Amino Acids:L-Cysteine,L-Cystine, Andl-Cysteine-Derived Radicals. S-S, S-H, and C-S Bond Dissociation Enthalpies. *J. Phys. Chem. B* **2010**, *114*, 10530-10540.

(218) Lio, A.; Charych, D.; Salmeron, M. Comparative Atomic Force Microscopy Study of the Chain Length Dependence of Frictional Properties of Alkanethiols on Gold and Alkylsilanes on Mica. *J. Phys. Chem. B* **1997**, *101*, 3800-3805.

(219) Tawil, N.; Hatef, A.; Sacher, E.; Maisonneuve, M.; Gervais, T.; Mandeville, R.; Meunier, M. Surface Plasmon Resonance Determination of the Binding Mechanisms of L-Cysteine and Mercaptoundecanoic Acid on Gold. *J. Phys. Chem. C* **2013**, *117*, 6712-6718.

(220) Cavalleri, O.; Gonella, G.; Terreni, S.; Vignolo, M.; Pelori, P.; Floreano, L.; Morgante, A.; Canepa, M.; Rolandi, R. High Resolution XPS of the S 2p Core Level Region of the L-Cysteine/Gold Interface. *J. Phys. Condens. Matter* **2004**, *16*, S2477-S2482.

(221) Park, S.; Yang, S.; Shin, N.; Lee, E.; Lee, H. Adsorption Configuration for Cysteine on Ge (100): Coverage-Dependent Surface Reorientation. *J. Phys. Chem. C* **2010**, *114*, 14528-14531.

(222) Zharnikov, M.; Frey, S.; Heister, K.; Grunze, M. Modification of Alkanethiolate Monolayers by Low Energy Electron Irradiation: Dependence on the Substrate Material and on the Length and Isotopic Composition of the Alkyl Chains. *Langmuir* **2000**, *16*, 2697-2705.

(223) Zharnikov, M.; Grunze, M. Spectroscopic Characterization of Thiol-Derived Self-Assembling Monolayers. *J. Phys. Condens. Matter* **2001**, *13*, 11333.

(224) Ishida, T.; Choi, N.; Mizutani, W.; Tokumoto, H.; Kojima, I.; Azehara, H.; Hokari, H.; Akiba, U.; Fujihira, M. High-Resolution X-Ray Photoelectron Spectra of Organosulfur Monolayers on Au (111): S (2p) Spectral Dependence on Molecular Species. *Langmuir* **1999**, *15*, 6799-6806.

(225) Ishida, T.; Fukushima, H.; Mizutani, W.; Miyashita, S.; Ogiso, H.; Ozaki, K.; Tokumoto, H. Annealing Effect of Self-Assembled Monolayers Generated from Terphenyl Derivatized Thiols on Au (111). *Langmuir* **2002**, *18*, 83-92.

(226) Yang, Y.; Fan, L. High-Resolution XPS Study of Decanethiol on Au (111): Single Sulfur-Gold Bonding Interaction. *Langmuir* **2002**, *18*, 1157-1164.

(227) Weisshaar, D. E.; Walczak, M. M.; Porter, M. D. Electrochemically Induced Transformations of Monolayers Formed by Self-Assembly of Mercaptoethanol at Gold. *Langmuir* **1993**, *9*, 323-329.

(228) Vericat, C.; Vela, M.; Andreasen, G.; Salvarezza, R.; Vazquez, L.; Martin-Gago, J. Sulfur-Substrate Interactions in Spontaneously Formed Sulfur Adlayers on Au (111). *Langmuir* **2001**, *17*, 4919-4924.

(229) Rodriguez, J. A.; Dvorak, J.; Jirsak, T.; Liu, G.; Hrbek, J.; Aray, Y.; González, C. Coverage Effects and the Nature of the Metal-Sulfur Bond in S/Au (111): High-Resolution Photoemission and Density-Functional Studies. *J. Am. Chem. Soc.* **2003**, *125*, 276-285.

(230) Leggett, G. J.; Davies, M. C.; Jackson, D. E.; Tendler, S. J. Surface Studies by Static Secondary Ion Mass Spectrometry: Adsorption of 3-Mercaptopropionic Acid and Cysteine Onto Gold Surfaces. *J. Phys. Chem.* **1993**, *97*, 5348-5355.

(231) Cavalleri, O.; Oliveri, L.; Dacca, A.; Parodi, R.; Rolandi, R. XPS Measurements on L-Cysteine and 1-Octadecanethiol Self-Assembled Films: A Comparative Study. *Appl. Surf. Sci.* **2001**, *175*, 357-362.

(232) Bagus, P. S.; Illas, F.; Pacchioni, G.; Parmigiani, F. Mechanisms Responsible for Chemical Shifts of Core-Level Binding Energies and their Relationship to Chemical Bonding. *Journal of electron spectroscopy and related phenomena* **1999**, *100*, 215-236.

(233) Höffling, B.; Ortmann, F.; Hannewald, K.; Bechstedt, F. In *Cysteine on Gold: An ab-initio Investigation;* High Performance Computing in Science and Engineering'11; Springer: 2012; pp 105-117.

(234) Martin, S. J.; Granstaff, V. E.; Frye, G. C. Characterization of a Quartz Crystal Microbalance with Simultaneous Mass and Liquid Loading. *Anal. Chem.* **1991**, *63*, 2272-2281.

(235) Mecea, V. M. From Quartz Crystal Microbalance to Fundamental Principles of Mass Measurements. *Anal. Lett.* **2005**, *38*, 753-767.

(236) Huang, Y. H.; Chang, J. S.; Chao, S. D.; Wu, K. C.; Huang, L. S. Improving the Binding Efficiency of Quartz Crystal Microbalance Biosensors by Applying the Electrothermal Effect. *Biomicrofluidics* **2014**, *8*, 054116.

(237) Pensa, E.; Carro, P.; Rubert, A.; Benítez, G.; Vericat, C.; Salvarezza, R. Thiol with an Unusual Adsorption− Desorption Behavior: 6-Mercaptopurine on Au (111). *Langmuir* **2010**, *26*, 17068-17074.

(238) Vericat, C.; Vela, M.; Benitez, G.; Carro, P.; Salvarezza, R. Self-Assembled Monolayers of Thiols and Dithiols on Gold: New Challenges for a Well-Known System. *Chem. Soc. Rev.* **2010**, *39*, 1805-1834.

(239) Gerritsen, M.; Jansen, J. A.; Lutterman, J. A. Performance of Subcutaneously Implanted Glucose Sensors for Continuous Monitoring. *Neth. J. Med.* **1999**, *54*, 167-179.

(240) Gifford, R.; Kehoe, J. J.; Barnes, S. L.; Kornilayev, B. A.; Alterman, M. A.; Wilson, G. S. Protein Interactions with Subcutaneously Implanted Biosensors. *Biomaterials* **2006**, *27*, 2587-2598.

(241) Martwiset, S.; Koh, A. E.; Chen, W. Nonfouling Characteristics of Dextran-Containing Surfaces. *Langmuir* **2006**, *22*, 8192-8196.

(242) Morra, M.; Cassineli, C. Non-Fouling Properties of Polysaccharide-Coated Surfaces. *Journal of Biomaterials Science, Polymer Edition* **1999**, *10*, 1107-1124.

(243) Banerjee, I.; Pangule, R. C.; Kane, R. S. Antifouling Coatings: Recent Developments in the Design of Surfaces that Prevent Fouling by Proteins, Bacteria, and Marine Organisms. *Adv Mater* **2010**, *23*, 690-718.

(244) Bhardwaj, U.; Papadimitrakopoulos, F.; Burgess, D. J. A Review of the Development of a Vehicle for Localized and Controlled Drug Delivery for Implantable Biosensors. *J. Diabetes Sci. Technol.* **2008**, *2*, 1016-1029.

(245) Chuang, T. L.; Chang, C. C.; Chu-Su, Y.; Wei, S. C.; Zhao, X. H.; Hsueh, P. R.; Lin, C. W. Disposable Surface Plasmon Resonance Aptasensor with Membrane-Based Sample Handling Design for Quantitative Interferon-Gamma Detection. *Lab. Chip* **2014**, *14*, 2968-2977.

(246) Dubois, L. H.; Nuzzo, R. G. Synthesis, Structure, and Properties of Model Organic Surfaces. *Annu. Rev. Phys. Chem.* **1992**, *43*, 437-463.

(247) Love, J. C.; Estroff, L. A.; Kriebel, J. K.; Nuzzo, R. G.; Whitesides, G. M. Self-Assembled Monolayers of Thiolates on Metals as a Form of Nanotechnology. *Chem. Rev.* **2005**, *105*, 1103-1169.

(248) Tang, L.; Eaton, J. W. Fibrin(Ogen) Mediates Acute Inflammatory Responses to Biomaterials. *J. Exp. Med.* **1993**, *178*, 2147-2156.

(249) Tang, L.; Ugarova, T. P.; Plow, E. F.; Eaton, J. W. Molecular Determinants of Acute Inflammatory Responses to Biomaterials. *J. Clin. Invest.* **1996**, *97*, 1329-1334.

(250) Clarke, M. L.; Wang, J.; Chen, Z. Conformational Changes of Fibrinogen After Adsorption. *J Phys Chem B* **2005**, *109*, 22027-22035.

(251) Roach, P.; Farrar, D.; Perry, C. C. Interpretation of Protein Adsorption: Surface-Induced Conformational Changes. *J. Am. Chem. Soc.* **2005**, *127*, 8168-8173.

(252) Fabrizius-Homan, D. J.; Cooper, S. L. A Comparison of the Adsorption of Three Adhesive Proteins to Biomaterial Surfaces. *J. Biomater. Sci. Polym. Ed.* **1991**, *3*, 27-47.

(253) Fabrizius-Homan, D. J.; Cooper, S. L. Competitive Adsorption of Vitronectin with Albumin, Fibrinogen, and Fibronectin on Polymeric Biomaterials. *J. Biomed. Mater. Res.* **1991**, *25*, 953-971.

(254) Nimeri, G.; Lassen, B.; Golander, C. G.; Nilsson, U.; Elwing, H. Adsorption of Fibrinogen and some Other Proteins from Blood Plasma at a Variety of Solid Surfaces. *J. Biomater. Sci. Polym. Ed.* **1994**, *6*, 573-583.

(255) Nonckreman, C. J.; Fleith, S.; Rouxhet, P. G.; Dupont-Gillain, C. C. Competitive Adsorption of Fibrinogen and Albumin and Blood Platelet Adhesion on Surfaces Modified with Nanoparticles and/Or PEO. *Colloids Surf. B Biointerfaces* **2010**, *77*, 139-149.

(256) Wilson, C. J.; Clegg, R. E.; Leavesley, D. I.; Pearcy, M. J. Mediation of Biomaterial-Cell Interactions by Adsorbed Proteins: A Review. *Tissue Eng.* **2005**, *11*, 1-18.

(257) Huang, C. J.; Chu, S. H.; Wang, L. C.; Li, C. H.; Lee, T. R. Bioinspired Zwitterionic Surface Coatings with Robust Photostability and Fouling Resistance. *ACS Appl. Mater. Interfaces* **2015**, *7*, 23776-23786.

(258) Yang, R.; Goktekin, E.; Gleason, K. K. Zwitterionic Antifouling Coatings for the Purification of High-Salinity Shale Gas Produced Water. *Langmuir* **2015**, *31*, 11895-11903.

(259) Mohan, T.; Kargl, R.; Tradt, K. E.; Kulterer, M. R.; Bracic, M.; Hribernik, S.; Stana-Kleinschek, K.; Ribitsch, V. Antifouling Coating of Cellulose Acetate Thin Films with Polysaccharide Multilayers. *Carbohydr. Polym.* **2015**, *116*, 149-158.

(260) Sengupta, A.; Linehan, A. R.; Iovine, P. M. Impact of Starch Content on Protein Adsorption Characteristics in Amphiphilic Hybrid Graft Copolymers. *Int. J. Biol. Macromol.* **2016**, *82*, 256-263.

Appendix A

Supplementary Figures

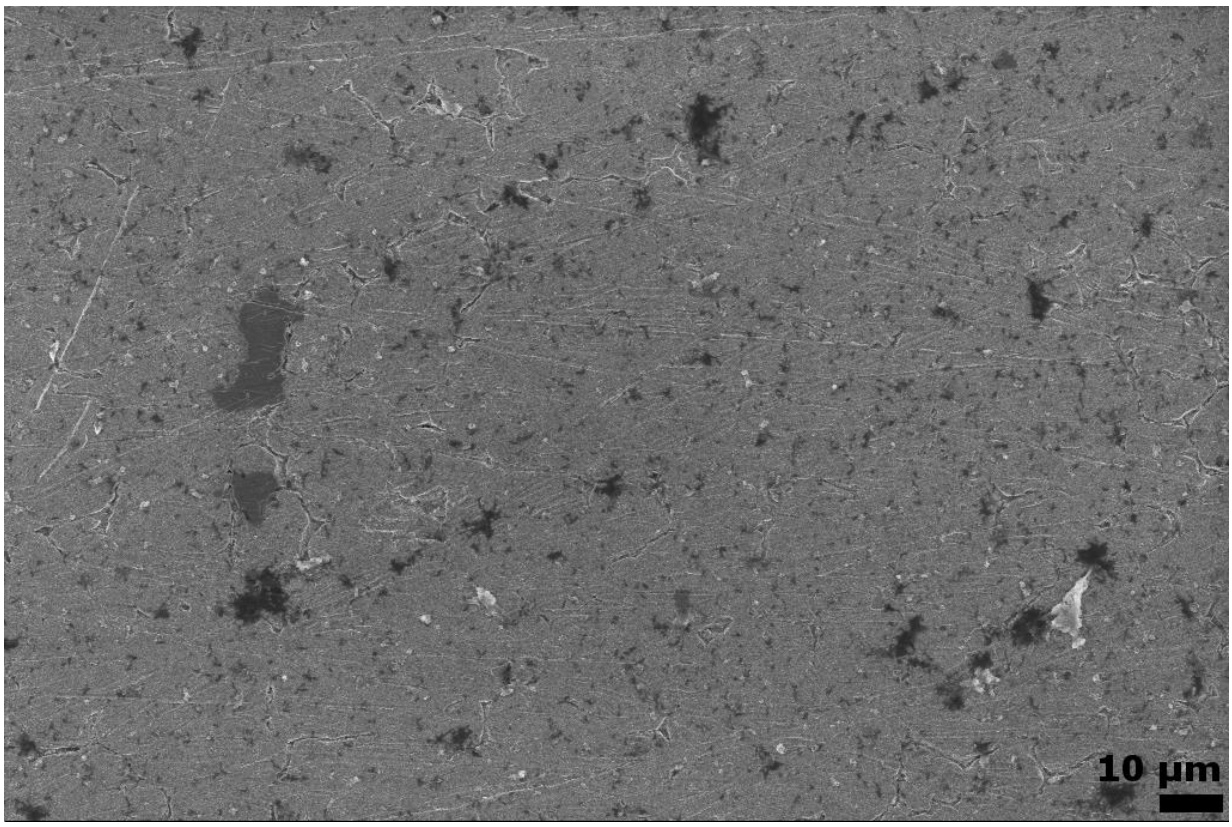

Supplementary Figure S1: SEM Image of a cysteine surface subsequent to BSA exposure.
The image was taken at 572X magnification. The imaged area of the exposed cysteine surface is almost double of the gold and stainless steel presented at Figure 12: BSA Fouling D & E, but still demonstrated less fouling.

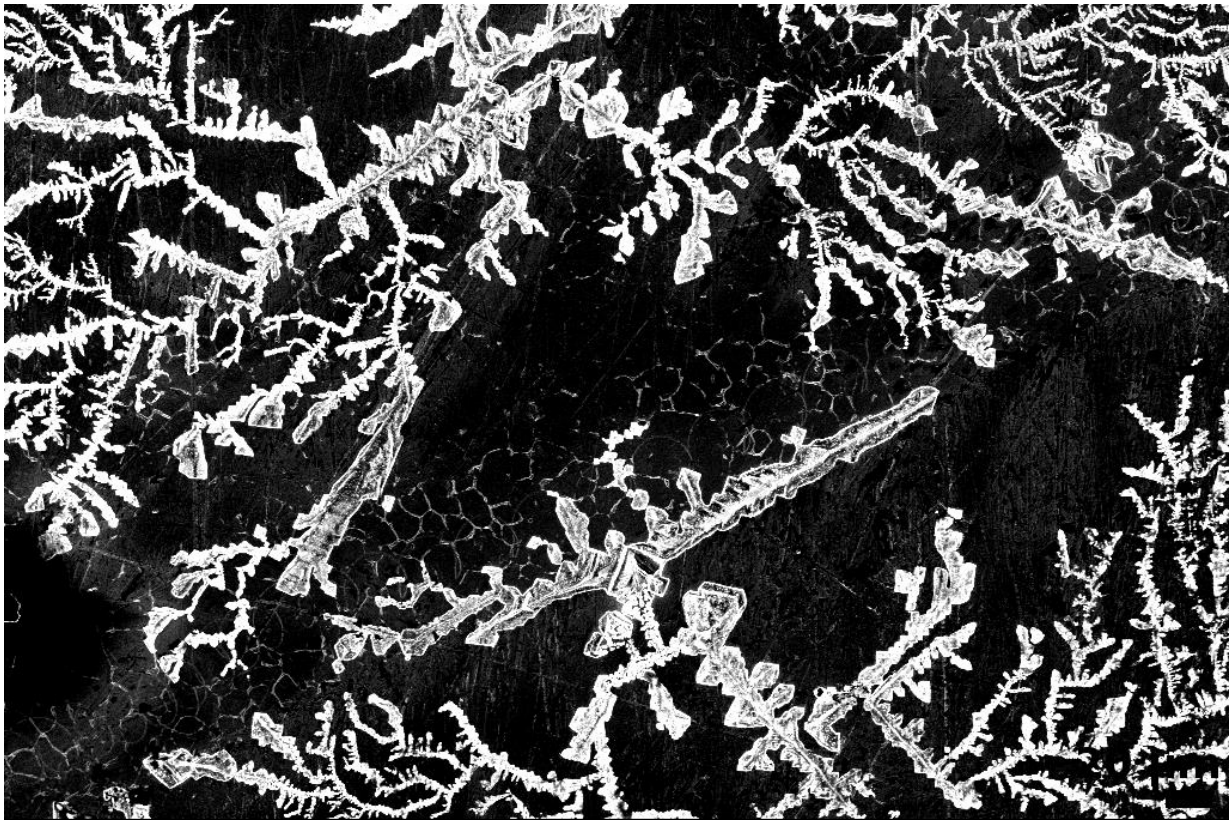

Supplementary Figure S2: SEM Image of a cysteine surface subsequent to serum exposure.
This image was taken at 202X magnification and illustrate a different electrolyte formation compared to Figure 5A. Compared with the images in Figure 5, there are many more nucleation points or "seed" in this area and may be the reason for the difference in salt pattern.

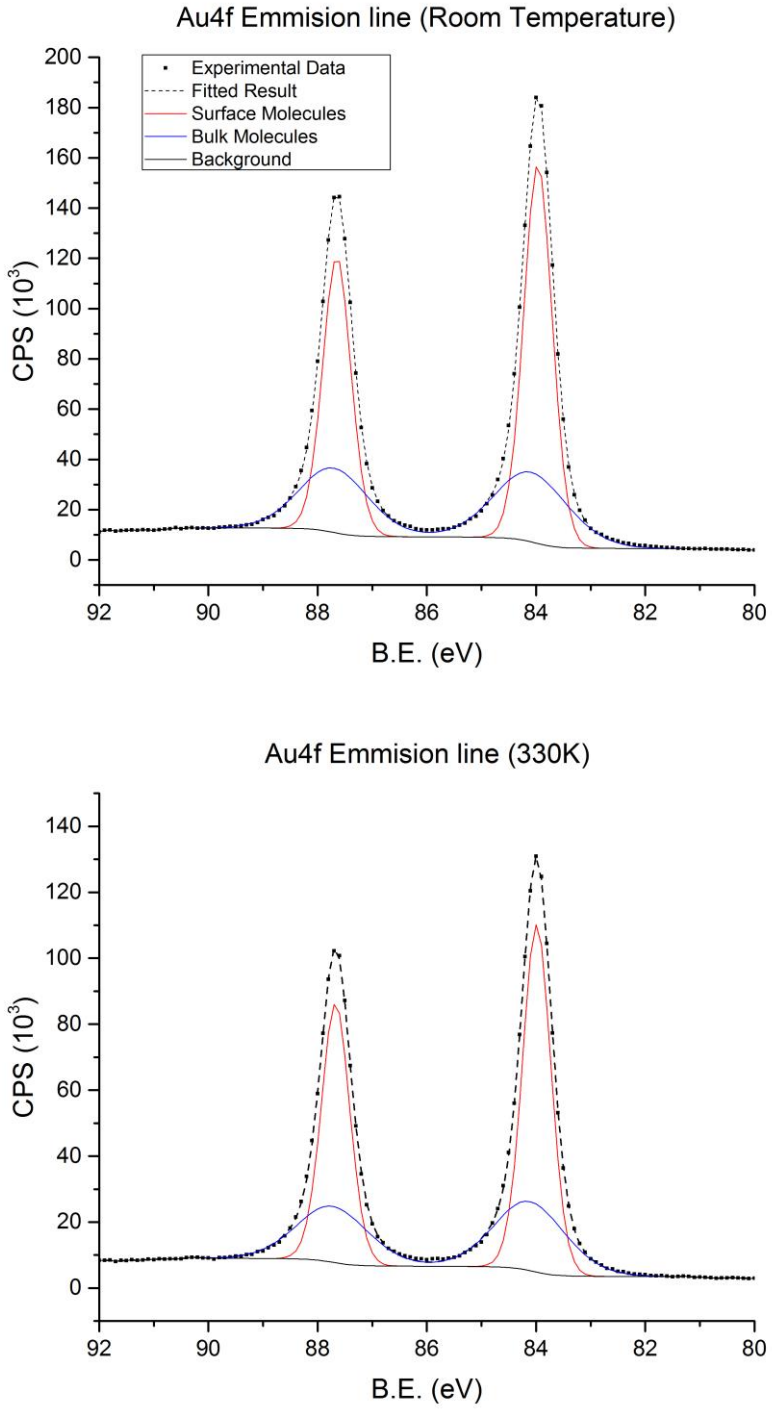

Supplementary Figure S3: Au4f Emission Line
For samples created at room temperature (top) and at 330K (bottom). The peak positions for these samples are almost identical at 83.98 ± 0.02 eV and 87.66 ± 0.01 eV.

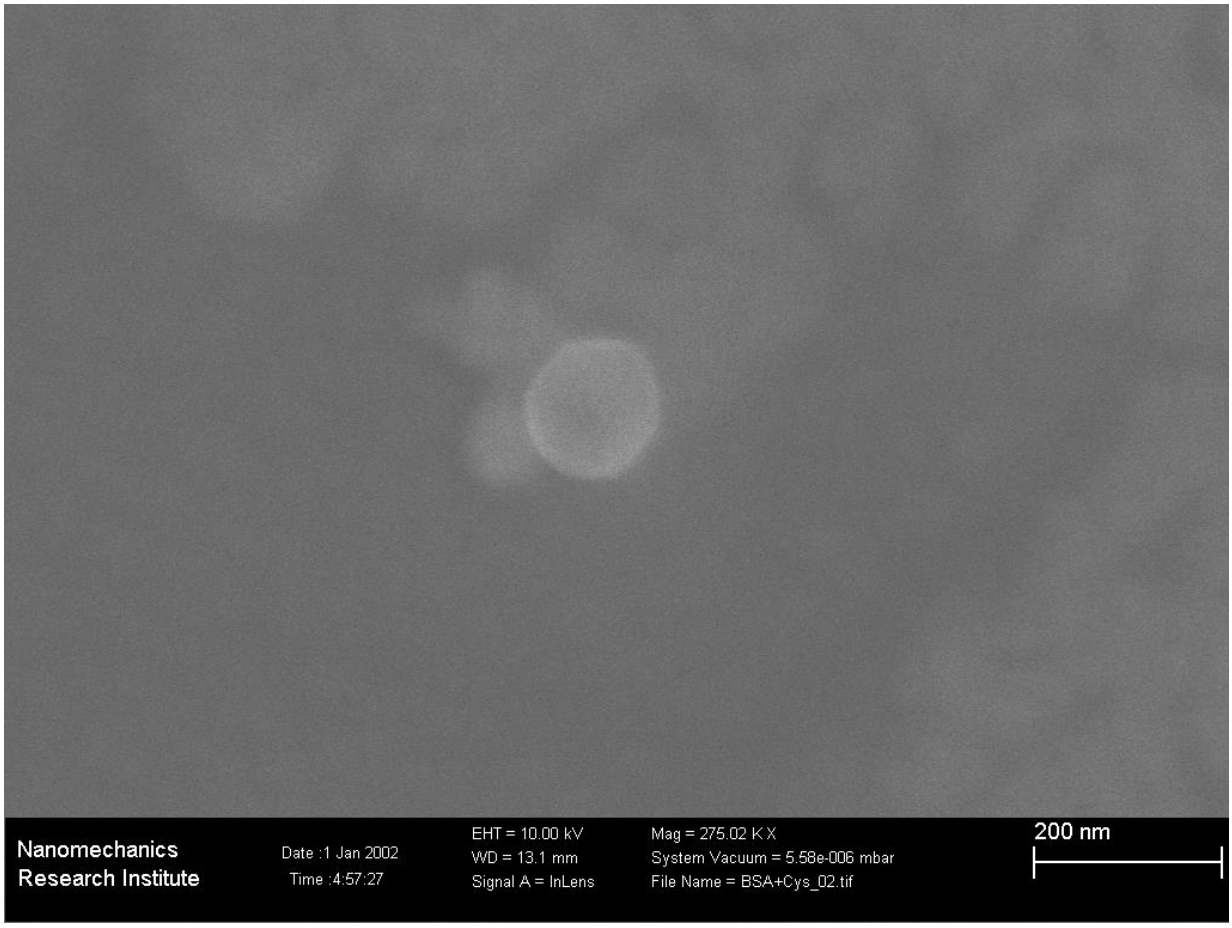

Supplementary Figure S4: SEM image of a BSA cluster adsorbed on a cysteine surface.

Appendix B

Supplementary Tables

Table S1. Peak Position and Full Width Halved Maximum (FWHM)
For each element presented in Figure 10. The Values are obtained by X-ray photoelectron spectroscopy using CasaXPS software

	Chemical State	Position	FWHM	Percent Area (%)
Gold	Primary Doublet	87.64; 83.96	0.747; 0.758	70.11%
	Secondary Doublet	87.69; 84.12	1.472; 1.854	29.89%
Carbon	C1: S-"C"-C	284.85	1.298	62.42%
	C2: C-"C"-C	286.12	1.856	24.17%
	C3: COO^-	288.39	1.650	11.78%
	C4: COOH	289.44	1.069	1.63%
Nitrogen	N1: NH2	398.40	1.379	9.62%
	N2: $NH3^+$	400.25	1.500	90.38%
Oxygen	O1: COO-	531.75	2.512	67.73%
	O2: O=C-"O"H	532.34	1.299	24.00%
	O3: "O"=COH	533.78	1.062	8.27%
Sulfur	Primary Doublet	161.99; 163.6	1.396; 1.495	80.93%
	Secondary Layer	165.03	1.104	19.07